Morphology And Dynamics of Phase Separation: From Simple to Active fluids

Relazione attività svolta durante il II anno
Dottorato in fisica teorica XXXII ciclo
Dip. di Fisica "M.Merlin" Bari
Supervisor: Prof. Giuseppe Gonnella, Dot. Antonio Lamura

Giuseppe Negro

October 10, 2018

1 Introduzione

Scopo del progetto è lo studio della dinamica di transizione di fase in alcune importanti classi di sistemi fluidi. Partendo dal caso di fluido ad una singola componente vogliamo studiare la separazione di fase tra liquido e vapore e la legge di crescita dei domini delle due fasi, in un sistema raffreddato al di sotto del punto critico. Tale studio trova motivazione nel fatto che, come si preciserà meglio in seguito, questo sistema non è stato mai studiato in dimensione $d = 3$. Vogliamo poi considerare miscele di fluidi con una componente attiva, che rappresentano sistemi biologici o materiali biosintetici, e studiare nuovi meccanismi di autopropulsione. Il Tratto caratterizzante dei sistemi attivi è rappresentato dal fatto che i costituenti sono in grado di assorbire energia, da serbatoi interni o dall'esterno, e dissiparla in attività come crescita, duplicazione, autopropulsione[1]. Essi costituiscono un campo di ricerca di enorme interesse, all'interfaccia tra fisica della materia soffice, meccanica statistica e biofisica.

Questo studio sarà condotto utilizzando metodi numerici Lattice Boltzmann (LB)[2], già utilizzati in passato per lo studio della dinamica di fluidi complessi.

Per tutti i sistemi in oggetto è conveniente descrivere l' enorme numero di gradi di libertà interagenti in termini di pochi campi coarse grained. La descrizione dinamica nel continuo richiede la definizione di un modello termodinamico per il sistema in esame. Utilizzeremo un approccio *à la* Ginzburg-Landau in cui l' energia libera è espressa come una funzione polinomiale degli invarianti del parametro d'ordine rispetto al gruppo di simmetria del sistema. A partire da questo ricaviamo le forze termodinamiche (tensore di pressione e potenziale chimico) che sono inserite nelle equazioni di evoluzione dinamica. Le corrispondenti equazioni sono quella di Navier-Stokes, quella di continuità e quella per l' energia (se necessaria). Nel caso delle miscele fluide e dei cristalli liquidi bisogna considerare anche un ulteriore insieme di equazioni che descrivono l'evoluzione del parametro d' ordine, che può essere una quantità scalare, vettoriale o tensoriale, a seconda del sistema considerato e delle sue simmetrie. Un approccio analitico, che risolva le equazioni di evoluzione, è possibile solo per sistemi e geometrie molto semplici. Diviene dunque essenziale sviluppare e adottare un approccio numerico. I metodi LB, in particolare, rappresentano tecniche computazionali moderne usate in fluidodinamica per la simulazione del campo di velocità e per lo studio degli effetti da esso

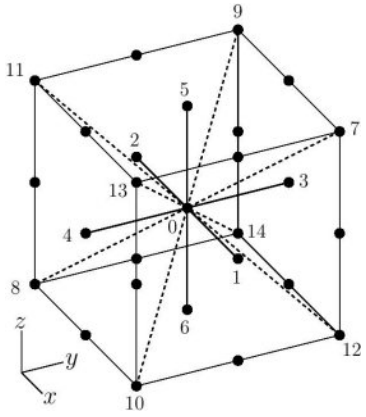

Figure 1: Rappresentazione delle velocità reticolari nella geometria utilizzata $D3Q15$.

generati. Essi sono costruiti a partire da particelle che si muovono tra i siti di un reticolo regolare secondo l' equazione del trasporto di Boltzmann discretizzata (LBE). Tale approccio trascura gli effetti microscopici, ma tiene conto dell' esistenza di difetti topologici a scale intermedie, come per esempio le interfacce nelle miscele di fluidi, e l' accoppiamento di questi oggetti con il campo di velocità.

Nell'ambito del progetto il secondo anno è stato dedicato ai seguenti punti:

- Studio della separazione di fase tra liquido e vapore, in un sistema raffreddato al di sotto del punto critico, e determinazione delle leggi di crescita dei domini delle due fasi in dimensione $d = 3$. A tal fine è stato utilizzato uno specifico schema LB sviluppato e implementato nell'ambito delle attività del primo anno.
- Utilizzando una modellizzazione Liquido-Vapore, con l'aggiunta di un ulteriore campo atto a rappresentare la concentrazione di materiale attivo, si è sviluppato e studiato numericamente un modello per il meccanismo all'origine della motilità cellulare in assenza di substrato.
- Studio numerico della morfologia della dinamica e della reologia di miscele di fluidi in cui una delle due componenti è attiva.

2 Dinamica della separazione di fase Liquido Vapore in 3D

Quando un fluido, inizialmente in uno stato disordinato, viene istantaneamente raffreddato ad una temperatura al di sotto della linea spinodale[1], in una regione di coesistenza tra due fasi, si formano domini delle due differenti fasi che crescono nel tempo. In tal caso la separazione di fase prende il nome di decomposizione spinodale.

Tipicamente la crescita di tali domini è un fenomeno di scala, ovvero esiste una singola lunghezza caratteristica l tale che la struttura dei domini appare la stessa durante l'evoluzione temporale, quando tutte le lunghezze sono riscalate rispetto a l. Quanto detto prende il nome di *ipotesi di scaling*

[1] curva nel diagramma temperatura-densità (o composizione per sistemi a più componenti) luogo dei punti caratterizzati da derivata seconda dell'energia libera di Gibbs nulla.

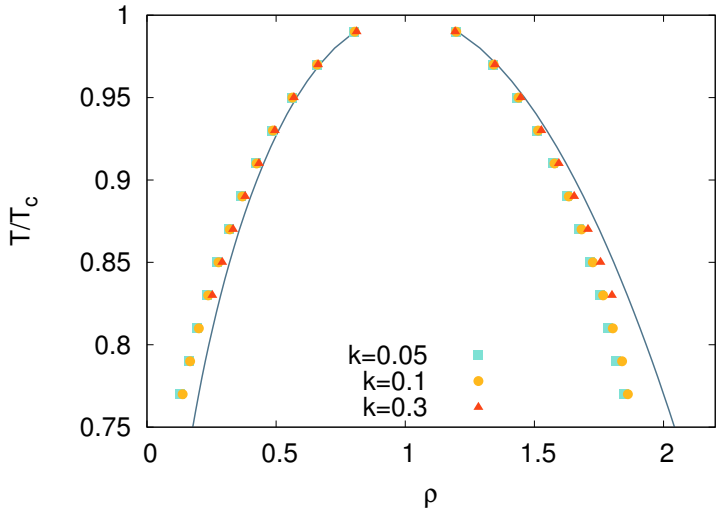

Figure 2: Diagramma di fase ottenuto numericamente per diversi valori del coefficiente k, che controlla la larghezza delle interfacce, e confronto con quello teorico ottenuto con la costruzione di Maxwell (curve continue).

dinamico[3], ed è supportata dai risultati di simulazioni numeriche e esperimenti per il fattore di struttura e le funzioni di correlazione. Tipicamente la taglia media dei domini $l(t)$ cresce nel tempo secondo legge a potenza, con un esponente α che dipende dalla morfologia, struttura dei domini, dimensione del sistema, presenza di effetti idrodinamici e numero di componenti del parametro d'ordine e se esso è conservato o meno.

Per le miscele binarie si possono distinguere tre differenti regimi [3], ognuno caratterizzato da uno specifico meccanismo fisico di crescita, la cui esistenza può essere dedotta analizzando le equazioni della dinamica, le equazioni di Navier-Stokes e l'equazione di evoluzione del parametro d'ordine, e assumendo che esista una sola lunghezza caratteristica rilevante:

- *Diffusivo*
  Nelle fasi immediatamente successive ad un *quench*, i.e. una brusca diminuzione di temperatura, il meccanismo di crescita dei domini è la diffusione di molecole da domini più piccoli, a curvatura più grande, a domini più grandi con curvatura inferiore. Si può mostrare che l'esponente con cui i domini crescono nel tempo è in questo caso $\alpha = 1/3$.

- *Idrodinamico Viscoso*
  Quando, durante il processo di separazione di fase, l'idrodinamica comincia ad essere rilevante ma le velocità sono piccole e variano poco nel tempo, si può assumere che il termine inerziale nelle equazioni di Navier-Stokes sia trascurabile. Imponendo quindi che le forze viscose siano bilanciate da forze di interfaccia si trova, in questo regime $\alpha = 1$ (come messo in evidenza per la prima volta da Siggia).

- *Idrodinamico Inerziale*
  Per velocità più elevate, il fenomeno fisico rilevante diviene il bilancio tra le forze di interfaccia e le forze inerziali. Sotto queste assunzioni si trova $\alpha = 2/3$.

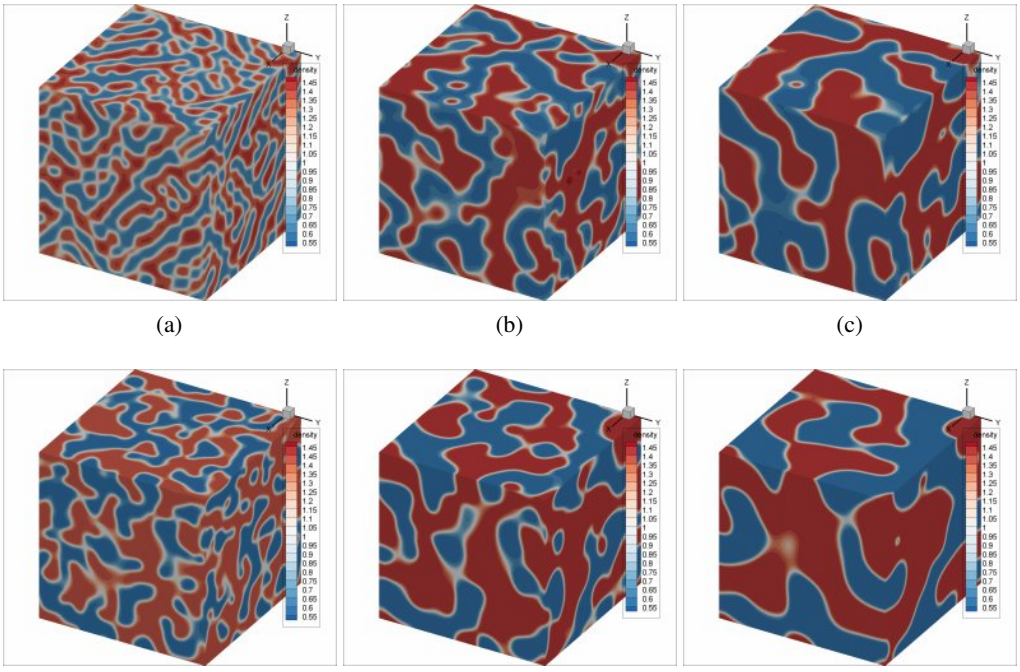

(a) (b) (c)

(d) $t = 570$ (e) $t = 10832$ (f) $t = 1938$

Figure 3: Snapshots della densità ρ, per un sistema di taglia $L = 256$ e viscosità $\eta = 3$ (**a-c**) e $\eta = 1$ (**d-f**). Notiamo come la separazione di fase sia ritardata nel caso di viscosità più alta, e come i domini appaiano meno regolari.

Il regime inerziale, per piccoli valori della viscosità, e il regime viscoso, per valori più alti della viscosità, sono stati osservati numericamente in un importante lavoro di Keadon et al. [4], per miscele binarie in 3D.

Per sistemi a singola componente con separazione di fase Liquido-Vapore, in cui il parametro d'ordine è la densità ρ, che non è localmente conservata, non è noto quali debbano essere gli esponenti di crescita. I pochi risultati in letteratura riguardando solo sistemi 2D[5], e riportano l'esistenza di un regime inerziale, e di un regime caratterizzato da un esponente di crescita $\alpha = 1/2$ per viscosità sufficientemente elevate.

Parte dell'attività di ricerca, durante il primo anno, è stata dedicata allo sviluppo e all'implementazione di uno schema LB per lo studio della separazione di fase liquido vapore in 3D, mentre durante il secondo anno si è provveduto alla parallelizzazione dello stesso, al fine di considerare sistemi di grandezza sino ad ora impossibili da simulare.

L'approccio LB prevede una discretizzazione dello spazio fisico e delle velocità consentite a livello di ciascun sito reticolare, in base ad opportune proprietà geometriche. Nel caso specifico si è scelto un modello $D3Q15$ (3 dimensioni spaziali e 15 velocità reticolari (Fig. 1)). L'evoluzione del fluido è definita a partire da un insieme discreto di N funzioni di distribuzione $\{f_i\}$ $(i = 0, ..., N-1)$, che obbediscono alla equazione del trasporto di Boltzmann nell'approssimazione BGK:

$$f_i(\mathbf{r} + \mathbf{e}_i \Delta t, t + \Delta t) - f_i(\mathbf{r}, t) = -\frac{\Delta t}{\tau}[f_i(\mathbf{r}, t) - f_i^{eq}(\mathbf{r}, t)] \,, \tag{1}$$

dove $\mathbf{r}$ e t rappresentano coordinate spaziali e tempo, rispettivamente, $\{\mathbf{e_i}\}$ $(i = 0, ..., N-1)$ è

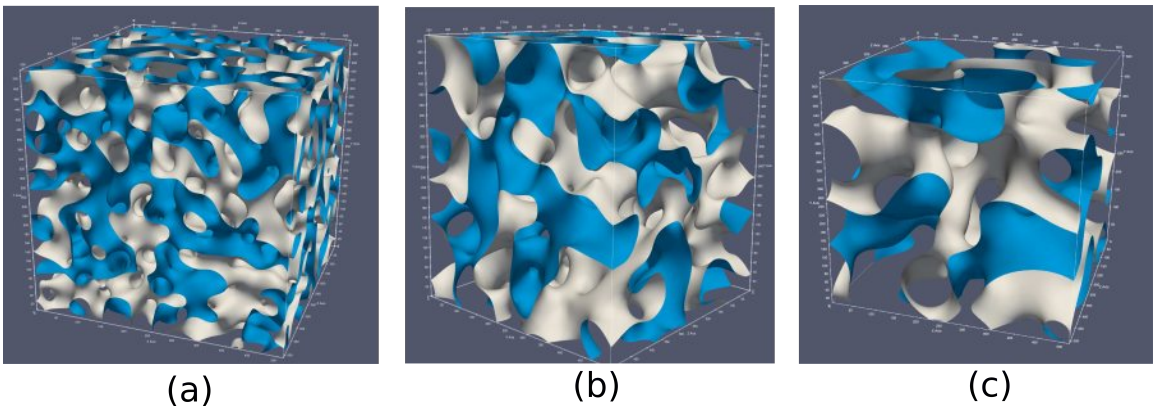

Figure 4: Snapshots a differenti istanti di tempo dell'interfaccia liquido-vapore per un sistema di taglia $L = 512$ per un quench poco profondo a $T = 0.99$ e viscosità $\eta = 1$, per cui si osserva, a questa temperatura, l'esponente $\alpha = 1/2$, presente invece da $\eta = 2$ in poi a $T = 0.95$.

l'insieme delle velocità discrete, Δt è il *time step*, e τ è il tempo di rilassamento che caratterizza il rilassamento verso e distribuzioni di equilibrio f_i^{eq}. La ricetta LB prevede che per le distribuzioni di equilibrio, e eventualmente anche per i termini di forza dell'equazione del trasporto se presenti, si effettui una espansione i cui coefficienti dovranno essere determinati in modo da ottenere le corrette equazioni della dinamica nel limite continuo. A tal fine si è scelto di sviluppare uno schema LB basato su una derivazione rigorosa della LBE per mezzo di una proiezione di Gauss-Hermite della corrispondente equazione nel continuo[6]. La dimensionalità del problema in esame ha anche reso necessario prendere in considerazione metodi di discretizzazione degli operatori differenziali diversi da quelli standard. La scelta ottimale è risultata essere quella della di operatori con errori di discretizzazione isotropi [7]. Alla fase di implementazione è seguita la fase di test del codice. Il diagramma di fase della separazione liquido-vapore è stato ricostruito numericamente e risulta essere consistente con quello teorico ottenuto attraverso la costruzione di Maxwell (Fig.2).

In figura 3 sono riportati alcuni snapshots della densità ρ, per un sistema di taglia $L = 256$, per viscosità $\eta = 3$ (Serie superiore) e $\eta = 1$ (Serie inferiore). I casi riportati fanno riferimento a due valori tipici, in *lattice units* (LU), di bassa e alta viscosità per il sistema in esame. Essi dipendono dal modello *LB* considerato e il massimo e il minimo η sono limitati dalla stabilità numerica del codice.

Notiamo come la separazione di fase sia ritardata nel caso di viscosità più alta, e che i domini appaino meno regolari. Queste differenze si riflettono sull'andamento della taglia media dei domini $l(t)$ nel tempo (Fig. 5). Questa è stata misurata come il primo momento del fattore di struttura della densità e sembra suggerire, per il momento, l'esistenza di due regimi: uno caratterizzato da un esponete $\alpha = 2/3$ per bassi valori della viscosità (Fig.5a), e un regime di crescita con $\alpha = 1/2$ (Fig.5b) per grandi valori della viscosità. L'esistenza di un regime iniziale, per alti valori di viscosità, di crescita accelerata prima del regime $1/2$, ha suggerito di considerare sistemi di taglia più grande. Per poter considerare sistemi di taglia $L = 512$ è stato necessario parallelizzare il nostro schema LB, tramite lo standard open MPI. Si è inoltre convenuto di considerare qunech meno profondi, dato che in vicinanza del punto critico la tensione superficiale del sistema liquido-vapore ha un andamento con la temperatura simile a quello delle miscele binarie. I risultati sono mostrati in figura 6(a), dove risulta evidente un regime lineare seguito da una crescita con esponente $\alpha = 1/2$ per valori di viscosità più elevata. Il differente comportamento tra i diversi valori di viscosità è marcato da un

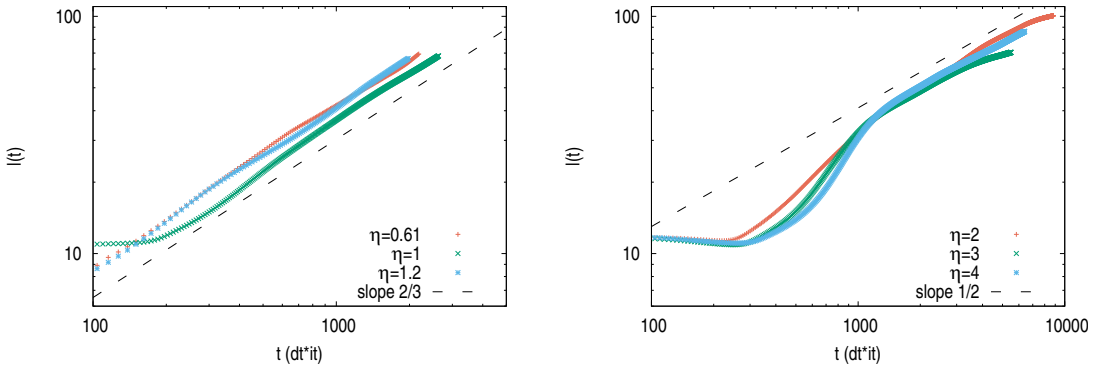

(a) (b)

Figure 5: Taglia media dei domini in funzione del tempo, per un reticolo di taglia $L = 256$, per bassa viscosità **(a)** e viscosità più alta **(b)**. Nel caso di bassa viscosità gli andamenti appaiono consistenti con un esponente di crescita $\alpha \simeq 2/3$ (retta tratteggiata in **(a)**), mentre nel caso di viscosità più alta gli andamenti suggeriscono un esponente $\alpha \simeq 1/2$ (retta tratteggiata in **(b)**).

differente comportamento nel tempo della separation depth (figura 6(b)), osservabile che misura la distanza dei domini di una fase dal loro stato di equilibrio.

Qualitativamente si può intuire, dalla dinamica della interfaccia tra liquido e vapore (figura 4(c)), come su sistemi più grandi, una volta raggiunto l'equilibrio, la crescita dei domini sia dominata dalla diffusione dell'interfaccia, piuttosto che dal meccanismo di pinch-off (figura 4(a-b)), che determina ad alta viscosità, una crescita rapida con esponente $\alpha = 1$.

Questa linea di ricerca proseguirà in collaborazione con il *Prof. Sofonea*, dell'università di Timisoara, esperto nell'ambito dello sviluppo ed implementazione di algoritmi LB su GPU, per confrontare i risultati sin qui ottenuti con schemi LB più precisi, sebbene meno efficienti.

3 Goccia di liquido attiva

Capire le regole che governano il moto di una cellula (o *cell motility*) è un problema affascinante in biofisica poiché il meccanismo che governa la motilità è puramente auto-organizzato[8]. Il meccanismo della cell-motility è anche di enorme interesse in campo biomedico, sia per il suo ruolo centrale nell'auto-assemblamento di tessuti nella crescita embrionale, necessaria per la rigenerazione di tessuti, sia per comprendere il meccanismo con cui le cellule formano metastasi nel cancro. Il cosiddetto *Crawling*, moto di una cellula su substrato[8], è stato ampiamente studiato sia dal punto di vista teorico sia numericamente. Al contrario, il moto di una cellula in bulk, ad esempio una cellula che si muove in un ambiente 3D o nella matrice extracellulare, necessita ancora di una completa comprensione e modelizzazione dal punto di vista teorico. Un ruolo fondamentale nella motilità cellulare è ricoperto dalla miosina. Essa è una proteina motrice, rintracciabile nelle cellule eucariotiche, responsabile del movimento basato sui filamenti di actina. Sia la contrazione della miosina che la polimerizzazione della actina contribuiscono al moto della cellula. In particolare la contrazione è la sola responsabile per la polarizzazione della cellula[9]. I risultati numerici riportati in letteratura fanno riferimento tutti a sistemi composti da una goccia di gel attivo polare il cui moto è dominato dall'instaurarsi di difetti nel campo di polarizzazione [10]. Tuttavia, recenti

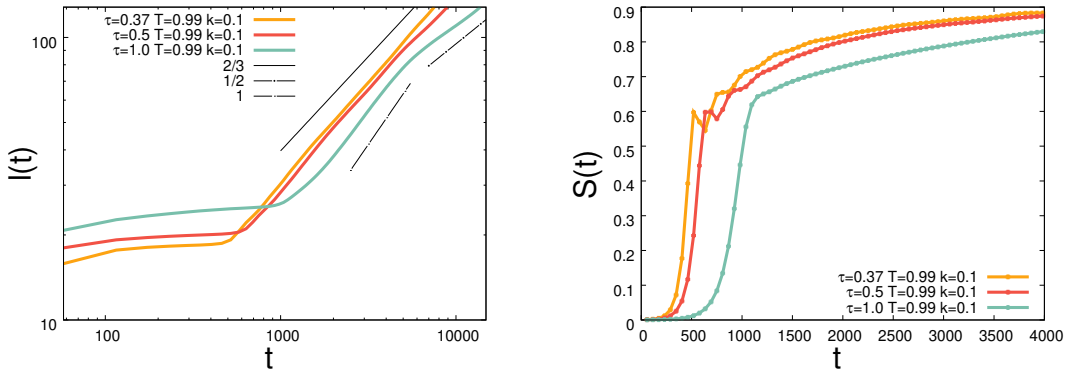

(a) (b)

Figure 6: **(a)**Taglia media dei domini in funzione del tempo, per un reticolo di taglia $L = 512$. **(b)** Separation depth in funzione del tempo, per un reticolo di taglia $L = 512$.

risultati sperimentali [11] suggeriscono che per alcuni tipi di cellule il moto può essere guidato esclusivamente dalla contrazione e dalla concentrazione di miosina presente.

Il nostro obiettivo è quello di sviluppare un modello per il moto cellulare che sia governato dalla sola contrazione della miosina, e che dunque sia isotropo e non prenda in considerazione la dinamica del campo di polarizzazione.

Partiamo quindi modellizzando la cellula come una goccia di liquido in equilibrio termodinamico con il vapore. Si è preso in considerazione questo sistema, e non ad esempio una miscela binaria, poiché ci aspettiamo che sia necessario che il fluido sia comprimibile perché ci sia motilità guidata dalla contrazione. All'interno della goccia aggiungiamo una certa concentrazione di miosina (Fig. 7). Supponiamo che essa sia posizionata a sinistra nella cellula. La miosina è contrattile quindi 'spinge il flusso', ovvero crea un flusso maggiore a sinistra piuttosto che a destra e questo dovrebbe essere sufficiente a far muovere la cellula. Introduciamo quindi un campo scalare che rappresenta la miosina, che sia nullo all'esterno della cellula e valga 1 all'interno. La miosina crea contrazione, e l'interplay tra contrazione e asimmetria dovrebbe generare il moto della cellula. La concentrazione di miosina deve essere considerata nell'equazione della pressione che quindi risulterà essere uguale a

$$p = \rho T - \phi\zeta - G\rho \quad , \tag{2}$$

ζ è la contrattilità($\zeta < 0$), mentre G è un parametro legato alla comprimibilità del sistema..

Le equazioni che governano la dinamica del sistema sono le equazioni di Navier Stokes per la velocità e l'equazione di convezione-diffusione per l'evoluzione della concentrazione di miosina ϕ:

$$\begin{cases} \rho \frac{D\mathbf{v}}{Dt} = -\nabla p + \eta\nabla^2\mathbf{v} - \frac{2}{3}\eta\nabla(\nabla.\mathbf{v}) \\ \\ \frac{\partial\phi}{\partial t} + \nabla.(\phi\mathbf{v}) = \Gamma\nabla^2(\frac{\delta\mathscr{F}}{\delta\phi}) \quad . \end{cases} \tag{3}$$

Nell'equazione di Navier Stokes compare il gradiente della pressione e quindi la variazione di velocità è legata al gradiente di concentrazione di miosina.

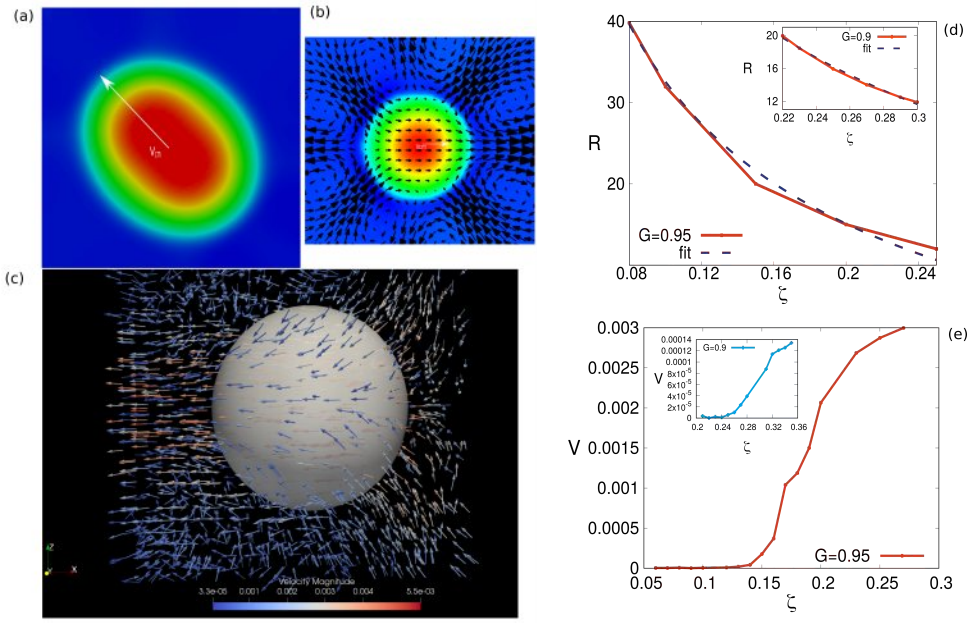

Figure 7: **(a)** Contour plot della densità *rho* e **(b)**-**(c)** campo di velocità per due differenti valori di attività per una goccia in d=2 e d=3.**(d)**-**(e)** Raggio della goccia e velocità del centro di massa al variare dell'attività ζ per due differenti valori del parametro G.

Nell'equazione di convezione-diffusione, l'energia libera è data da

$$\mathscr{F} = \int d\mathbf{r} \quad \{\frac{a}{2}\phi^2 + \ k(\nabla\phi)^2 - b(\rho-\rho_{av})\phi^2 + c\phi(\nabla\rho)^2\} \ . \tag{4}$$

Il terzo e il quarto termine vengono introdotti per permettere che la miosina rimanga all'interno della cellula (i.e., goccia di liquido).

I risultati ottenuti confermano che il meccanismo proposto, che impiega la contrazione della miosina all'interno della goccia di liquido per generare la motilità della stessa, sia sufficiente per il moto in assenza di substrato. La contrazione è infatti sufficiente a creare una goccia di actina, e sussiste un range per i parametri G e ζ per il quale si osserva motilità della goccia(Fig. 7(a)-(b)). Tale risultato è confermato anche dalle simulazioni in d=3 7(c). Si è inoltre provveduto a caratterizzare il moto della goccia Fig. 7(e) e l'andamento del raggio critico della goccia per cui si ha moto al variare del'attività Fig.7(d). Il diagramma di fase nel piano $G-\zeta$ completa lo studio (non mostrato qui) che è stato sottomesso come research article alla rivista EPL.

4 Studio della reologia di una miscela attiva simmetrica

In questa sezione verranno presentati i risultati riguardanti la caratterizzazione reologica di una emulsione polare attiva. L'attività di ricerca nel campo della materia attiva è stata principalmente focalizzata su sistemi a singola componente e in minor misura sul comportamento di miscele costituite da componenti attive e passive. Recenti studi su miscele binarie con una componente attiva hanno mostrato che l'attività può causare instabilità all'interfaccia tra le due componenti[12, 13]. Il modello

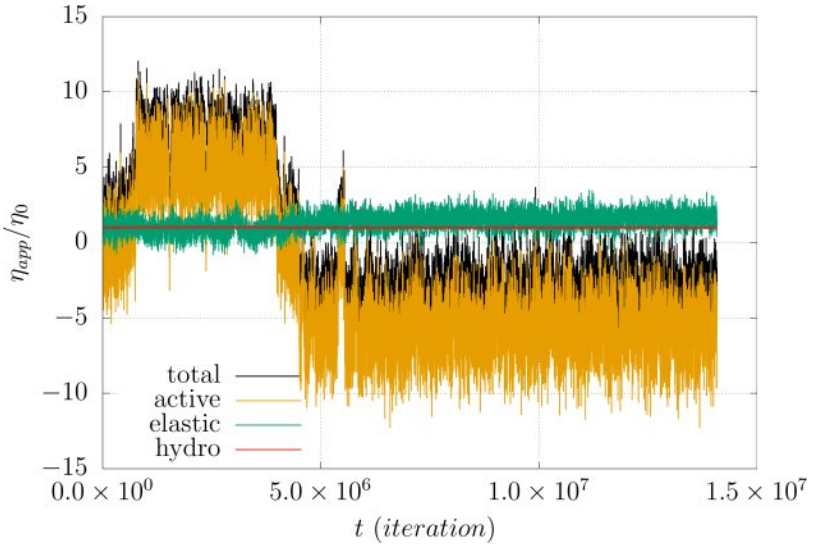

Figure 8: Rapporto (viscosità apparente)/(viscosità del fluido isostropo) vs tempo, per una miscela attiva polare con $\zeta = 0.005$, confinata tra due pareti aventi velocità in unità LB $v_w = 0.01$.

che presentiamo costituisce una generalizzazione dei modelli citati nel fatto che l'emulsificazione della componente attiva è favorita dalla presenza di un surfattante aggiunto alla miscela. In questo modo si ottiene un sistema in cui è possibile controllare la quantità di materiale attivo disperso. Questo consente di controllare non solo l'intensità ma anche la distribuzione spaziale dell'input energetico, dovuto alla presenza dell'attività, nel sistema. Questo sostituisce un enorme progresso sia dal punto di vista teorico che per l'influsso di tali studi in ambito tecnologico, dando la possibilità di progettare nuovi materiali biosintetici, le cui caratteristiche e proprietà possono essere controllate da un singolo parametro.

I fluidi attivi presentano una serie di fenomeni estremamente interessanti tra i quali il manifestarsi di un regime di super-fluido, e stati di viscosità negativa osservati recentemente in una sospensione di *Escherichia Coli*[14]. Nell'ambito del nostro modello vogliamo caratterizzare questi stati di superfluidità e indagare il meccanismo alla base di queste peculiari caratteristiche reologiche dei sistemi attivi.

Le variabili idrodinamiche del problema sono la densità del fluido ρ, la sua velocità $\mathbf{v}$, la concentrazione di materiale attivo ϕ, e la polarizzazione $\mathbf{P}$, che determina l'orientazione media della componente attiva.

Le equazioni che governano l'evoluzione del sistema sono

$$\rho\left(\frac{\partial}{\partial t}+\mathbf{v}\cdot\nabla\right)\mathbf{v} = -\nabla p+\nabla\cdot\underline{\underline{\sigma}}^{total}, \tag{5}$$

$$\frac{\partial\phi}{\partial t}+\nabla\cdot(\phi\mathbf{v}) = \nabla\cdot\left(M\nabla\frac{\delta F}{\delta\phi}\right), \tag{6}$$

$$\frac{\partial\mathbf{P}}{\partial t}+(\mathbf{v}\cdot\nabla)\mathbf{P} = -\underline{\underline{\Omega}}\cdot\mathbf{P}+\xi\underline{\underline{D}}\cdot\mathbf{P}-\frac{1}{\Gamma}\frac{\delta F}{\delta\mathbf{P}}, \tag{7}$$

nel limite di fluido incomprimibile. La prima è l'equazione di Navier Stokes dove p la pressione isotropica e $\underline{\underline{\sigma}}^{total}$ è il tensore degli stress totale [15].

Le equazioni (6)-(7) governano l'evoluzione temporale del campo di concentrazione e della polarizzazione della componete attiva del fluido. Dato che la concentrazione di materiale attivo è una quantità localmente conservata la sua evoluzione temporale sarà dettata da una equazione di convezione-diffusione, Eq. (6), dove M è la mobilità, F un funzionale di energia libera che verrà definito a breve, e $\delta F/\delta\phi$ il potenziale chimico.

La dinamica del campo di polarizzazione segue invece una equazione di advezione-rilassamento, Eq. (7), derivante dalla teoria dei cristalli liquidi. Qui Γ rappresenta la viscosità rotazionale, ξ è una costante che controlla la forma delle particelle attive, (positiva per particelle rod-like e negativa per particelle disk-like), $h = \delta F/\delta \mathbf{P}$ è il campo molecolare. $\underline{\underline{D}} = (\underline{\underline{W}} + \underline{\underline{W}}^T)/2$ e $\underline{\underline{\Omega}} = (\underline{\underline{W}} - \underline{\underline{W}}^T)/2$ rappresenta la parte simmetrica e anti-simmetrica del tensore gradiente del campo di velocità $W_{\alpha\beta} = \partial_\beta v_\alpha$, dove gli indici greci denotano le componenti cartesiane. Il tensore degli stress $\underline{\underline{\sigma}}^{total}$ considerato nelle equazioni di Navier-Stokes del modello, Eq. (5), può essere suddiviso in un pezzo passivo di equilibrio ed in uno attivo di non equilibrio:

$$\underline{\underline{\sigma}}^{total} = \underline{\underline{\sigma}}^{passive} + \underline{\underline{\sigma}}^{active}. \tag{8}$$

La parte passiva rappresenta la risposta elastica dal soluto ed è a sua volta somma di tre termini:

$$\underline{\underline{\sigma}}^{passive} = \underline{\underline{\sigma}}^{viscous} + \underline{\underline{\sigma}}^{elastic} + \underline{\underline{\sigma}}^{interface}. \tag{9}$$

Il primo è un termine di stress viscoso che può essere scritto come $\sigma^{viscous}_{\alpha\beta} = \eta(\partial_\alpha v_\beta + \partial_\beta v_\alpha)$ dove η è la viscosità di shear. Il secondo termine rappresenta lo stress elastico [15]:

$$\begin{aligned}\sigma^{elastic}_{\alpha\beta} = \quad & \frac{1}{2}(P_\alpha h_\beta - P_\beta h_\alpha) - \frac{\xi}{2}(P_\alpha h_\beta + P_\beta h_\alpha) \\ & -\kappa \partial_\alpha P_\gamma \partial_\beta P_\gamma,\end{aligned} \tag{10}$$

Dove κ è la costante elastica del cristallo liquido e il parametro ξ dipende dalla geometria come già accennato. In più ξ stabilisce se il fluido tende ad allinearsi con il flusso ($|\xi| > 1$) o fare tumbling ($|\xi| < 1$) sotto shear. Il terzo termine deriva dalla teoria delle miscele binarie. Esso include il contributo dovuto all'interfaccia tra la fase attiva e passiva:

$$\sigma^{interface}_{\alpha\beta} = \left(f - \phi\frac{\delta F}{\delta\phi}\right)\delta_{\alpha\beta} - \frac{\partial f}{\partial\left(\partial_\beta\phi\right)}\partial_\alpha\phi\ . \tag{11}$$

Nell'ultima espressione f è la densità di energia libera. Il contributo attivo al tensore degli stress, è dato da [16, 17]

$$\sigma^{active}_{\alpha\beta} = -\zeta\phi\left(P_\alpha P_\beta - \frac{1}{3}|\mathbf{P}|^2\delta_{\alpha\beta}\right), \tag{12}$$

dove ζ è il parametro di attività che è positivo per sistemi extensile (pushers) e negativo per quelli contractile (pullers). Lo stress attivo guida il sistema fuori dall'equilibrio fornendo energia. In assenza di attività, le proprietà termodinamiche della miscela sono codificate nel seguente funzionale di energia libera che accoppia l'energia libera del modello di Landau-Brazowskii [18] all'energia libera di un cristallo liquido polare :

$$\begin{aligned}F \quad [\phi,\mathbf{P}] = & \int d\mathbf{r}\,\{\frac{a}{4\phi^4_{cr}}\phi^2(\phi-\phi_0)^2 + \frac{k}{2}|\nabla\phi|^2 + \frac{c}{2}(\nabla^2\phi)^2 \\ - \quad & \frac{\alpha}{2}\frac{(\phi-\phi_{cr})}{\phi_{cr}}|\mathbf{P}|^2 + \frac{\alpha}{4}|\mathbf{P}|^4 + \frac{\kappa}{2}(\nabla\mathbf{P})^2 + \beta\mathbf{P}\cdot\nabla\phi\}\ .\end{aligned} \tag{13}$$

Il funzionale introdotto costituisce una generalizzazione dell'energia introdotta in [16], per una miscela binaria attiva.

Il primo termine, moltiplicato per la costante fenomenologica $a > 0$, descrive le proprietà di bulk della miscela, il secondo e il terzo determinano la tensione superficiale. Il termine di bulk è scelto in modo da avere una energia libera con due minimi, uno a $\phi = 0$ corrispondente alla componente passiva, e l'altro in $\phi \simeq \phi_0$, corrispondente alla fase attiva.

Il nostro studio, teso alla caratterizzazione reologica della emulsione in presenza di attività, ha messo in evidenza l'esistenza di un determinato range di shear rate $\dot{\gamma}$ e attività estensile $\zeta > 0$ per il quale il sistema mostra, durante la sua evoluzione temporale, stati di viscosità negativa e finestre di superfluidità (Fig. 8). Le differenti morfologie e i profili di velocità mediati sono mostrati in Fig. 9 per differenti valori di attività a fissato shear rate. Il profilo di velocità in Fig. 9(d) corrisponde ad una situazione di unidirected motion, mentre i profili in Fig. 9(f) sono tipici profili di viscosità negativa. Il meccanismo alla base dei differenti regimi, lineare, unidirected e inverso è caratterizzabile nell'ambito del nostro modello. Le caratteristiche reologiche sono infatti determinate dalla direzione del campo di polarizzazione in vicinanza delle pareti. Se la polarizzazione è allineata al flusso ad entrambe le pareti la viscosità risulta essere positiva, mentre se risulta essere in verso opposto al flusso per entrambe le pareti la viscosità è negativa e i profili di velocità risultano invertiti. Se invece la polarizzazione è allineata nello stesso verso del flusso ad una parete e in verso opposto all'altra si hanno stati di unidirected motion, in cui il bulk si muove in una sola direzione. Questi peculiari fenomeni, osservati in alcuni recenti esperimenti su sistemi biologici, risultano per la prima volta tutti osservabili e caratterizzabile nell'ambito del nostro modello. Il fenomeno della presenza di regimi di viscosità negativa rappresenta un primo passo verso la progettazione di motori biologici.

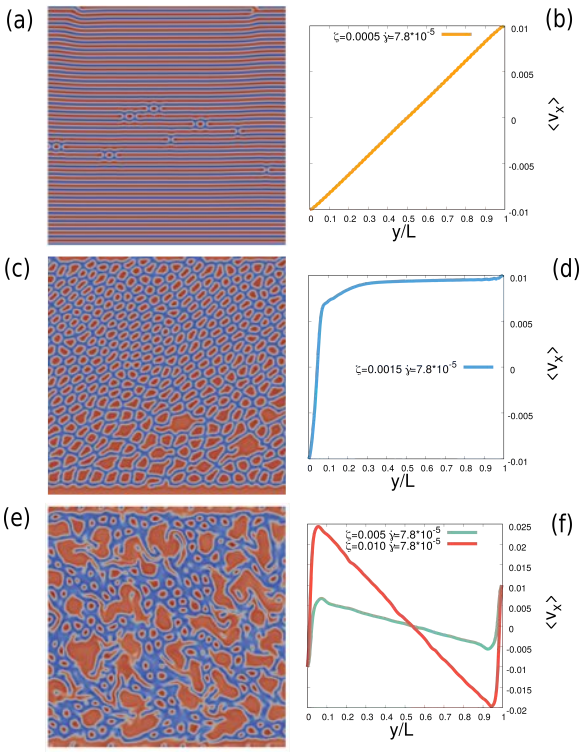

Figure 9: **(a)-(c)-(e)** ϕ contour plots per shear rate $\dot{\gamma} = 7.8 * 10^{-5}$ e rispettivamente $\zeta = 0.0005, 0.0015, 0.005$.**(b)-(d)-(f)** Profili di velocità mediati per lo stesso valore di $\dot{\gamma}$ e $Er_{\text{active}} = 5.7 * 10^{-2}$ curva **(arancione)**, $Er_{\text{active}} = 1.7 * 10^{-1}$**(blue)**, $Er_{\text{active}} = 5.7 * 10^{-1}$ **(light-green)** e $Er_{\text{active}} = 1.14$ **(rossa)** . Er_{active} è un numero adimensionale direttamente proporzionale all'attività ζ.

5 Attività didattica e partecipazione a scuole e conferenze

Durante il secondo anno di dottorato è stata svolta attività di supporto alla didattica nell'abito del corso di *Meccanica statistica avanzata*, nello specifico per la parte riguardante la *Teoria del gruppo*

di rinormalizzazione in Meccanica Statistica.

Si è inoltre trascorso, dal mese di Ottobre 2017 al mese di Dicembre 2017 un periodo all'estero presso il dipartimento di fisica J.Maxwell dell'università di Edimburgo, sotto la supervisione del Prof. Marenduzzo.

Come partecipazione a conferenze e scuole si riporta quanto segue:

- **Winter scholl in active matter Tel Aviv university**
- **Tim 18 Conference Timisoara** Dove si è presentato il lavoro dal titolo *Morphology and flow patters in higly asymmetric active emulsions*
- **DSFD 18 Conference** Wochester Ma. USA, dove si è presentato il lavoro dal titolo *Unidirected motion and negative viscosity in active polar emulsions*
- **Italian soft matter days** Padova, Italy, dove si è presentato un poster dal titolo *Morphology and flow patterns in polar active emulsions.*

6 Pubblicazioni

Morphology and flow patterns in highly asymmetric active emulsions, *G. Negro, L.N. Carenza, P. Digregorio, G. Gonnella,A. Lamura*, Physica A 2018.
Allegato alla presente relazione.

7 Lavori in sottomissione

In silico recostruction of myosin contraction based cell motility,*G. Negro, G. Gonnella,A. Lamura, D. Marenduzzo* EPL.
LB methods for active fluids, *G. Negro, L.N. Carenza, G. Gonnella,A. Lamura, A. Tiribocchi*.

8 Lavori in preparazione

Sheared active polar emulsion, *G. Negro, L.N. Carenza, G. Gonnella,A. Lamura, A. Tiribocchi*.

References

[1] M. C. Marchetti, J. F. Joanny, S. Ramaswamy, T. B. Liverpool, J. Prost, M. Rao, and R. A. Simha. Hydrodynamics of soft active matter. *Rev. Mod. Phys.*, 85:1143–1189, 2013.

[2] S. Succi. *The Lattice Boltzmann Equation: For Fluid Dynamics and Beyond*. Numerical Mathematics and Scientific Computation. Clarendon Press, 2001.

[3] A.J. Bray. Theory of phase-ordering kinetics. *Advances in Physics*, 43(3):357–459, 1994.

[4] V M. Kendon, Jean-Christophe Desplat, P Bladon, and M E. Cates. 3d spinodal decomposition in the inertial regime. 83, 02 1999.

[5] V. Sofonea, A. Lamura, G. Gonnella, and A. Cristea. Finite-difference lattice boltzmann model with flux limiters for liquid-vapor systems. *Phys. Rev. E*, 70:046702, Oct 2004.

[6] XIAOWEN SHAN, XUE-FENG YUAN, and HUDONG CHEN. Kinetic theory representation of hydrodynamics: a way beyond the navier–stokes equation. *Journal of Fluid Mechanics*, 550:413–441, 2006.

[7] Sumesh P. Thampi, Santosh Ansumali, R. Adhikari, and Sauro Succi. Isotropic discrete laplacian operators from lattice hydrodynamics. *Journal of Computational Physics*, 234(Supplement C):1 – 7, 2013.

[8] D. Bray. *Cell Movements: From Molecules to Motility*. Garland Pub., 2001.

[9] Renaud Poincloux, Olivier Collin, Floria Lizárraga, Maryse Romao, Marcel Debray, Matthieu Piel, and Philippe Chavrier. Contractility of the cell rear drives invasion of breast tumor cells in 3d matrigel. *Proceedings of the National Academy of Sciences*, 108(5):1943–1948, 2011.

[10] E. Tjhung, A. Tiribocchi, D. Marenduzzo, and M. E. Cates. A minimal physical model captures the shapes of crawling cells. *Nat.Commun.*, 6:5420, 2015.

[11] Hansuli Keller, Alireza Dehghani Zadeh, and Peter Eggli. Localised depletion of polymerised actin at the front of walker carcinosarcoma cells increases the speed of locomotion. *Cell Motility and the Cytoskeleton*, 53(3):189–202, 2002.

[12] E. Tjhung, D. Marenduzzo, and M. E. Cates. Spontaneous symmetry breaking in active droplets provides a generic route to motility. *Proc. Natl. Acad. Sci. U.S.A.*, 109(31):12381–12386, 2012.

[13] M. L. Blow, S. P. Thampi, and J. M. Yeomans. Biphasic, lyotropic, active nematics. *Phys. Rev. Lett.*, 113:248303, 2014.

[14] Héctor Matías López, Jérémie Gachelin, Carine Douarche, Harold Auradou, and Eric Clément. Turning bacteria suspensions into superfluids. *Phys. Rev. Lett.*, 115:028301, Jul 2015.

[15] A. N. Beris and B. J. Edwards. *Thermodynamics of Flowing Systems*. Oxford Engineering Science Series. Oxford University Press, 1994.

[16] E. Tjhung, M. E. Cates, and D. Marenduzzo. Nonequilibrium steady states in polar active fluids. *Soft Matter*, 7:7453–7464, 2011.

[17] R. Aditi Simha and S. Ramaswamy. Hydrodynamic fluctuations and instabilities in ordered suspensions of self-propelled particles. *Phys. Rev. Lett.*, 89:058101, 2002.

[18] S. A. Brazovskiĭ. Phase transition of an isotropic system to a nonuniform state. *J. Exp. Theor. Phys.*, 41:85, 1975.

Physica A 503 (2018) 464–475

Contents lists available at ScienceDirect

Physica A

journal homepage: www.elsevier.com/locate/physa

Morphology and flow patterns in highly asymmetric active emulsions

G. Negro [a,*], L.N. Carenza [a], P. Digregorio [a], G. Gonnella [a], A. Lamura [b]

[a] Dipartimento di Fisica, Università degli studi di Bari and INFN, Sezione di Bari, Via Amendola 173, 70126 Bari, Italy
[b] Istituto Applicazioni Calcolo, CNR, Via Amendola 122/D, 70126 Bari, Italy

HIGHLIGHTS

- The morphology and the dynamics of an emulsion made of a polar active gel and an isotropic passive fluid is studied.
- We focus on the case of a highly off-symmetric ratio between the active and passive components.
- In absence of activity the stationary state is characterized by an hexaticaly ordered array of droplets.
- Small amount of activity favors the elimination of defects in the array of droplets.
- Rising activity new and interesting morphologies arises depending on whether the system is contractile or extensile.

ARTICLE INFO

Article history:
Received 4 November 2017
Received in revised form 16 February 2018
Available online 9 March 2018

ABSTRACT

We investigate numerically, by a hybrid lattice Boltzmann method, the morphology and the dynamics of an emulsion made of a polar active gel, contractile or extensile, and an isotropic passive fluid. We focus on the case of a highly off-symmetric ratio between the active and passive components. In absence of any activity we observe an hexatic-ordered droplets phase, with some defects in the layout. We study how the morphology of the system is affected by activity both in the contractile and extensile case. In the extensile case a small amount of activity favors the elimination of defects in the array of droplets, while at higher activities, first aster-like rotating droplets appear, and then a disordered pattern occurs. In the contractile case, at sufficiently high values of activity, elongated structures are formed. Energy and enstrophy behavior mark the transitions between the different regimes.

1. Introduction

The capability of different systems of using energy taken from their environment to go out of thermal equilibrium, gives rise to a wealth of behaviors [1]. They range from swarming, self-assembly, spontaneous flows to other collective properties [2–5]. This boosted a deep interest in addressing their study in order to look for possible new physics, explore common features between different systems, and develop new strategies in designing synthetic devices and materials with smart properties.

Self-propelled objects represent a remarkable example of active matter. Starting from the seminal model of Vicsek [6] for swarms, it was later realized that common features can be traced in several systems at different scales promoting the introduction of statistical models able to describe such behaviors [7–10]. Another example of active matter, sharing

* Corresponding author.
E-mail addresses: giuseppe.negro@ba.infn.it (G. Negro), l.carenza@studenti.uniba.it (L.N. Carenza), pasquale.digregorio@ba.infn.it (P. Digregorio), g.gonnella@ba.infn.it (G. Gonnella), a.lamura@ba.iac.cnr.it (A. Lamura).

https://doi.org/10.1016/j.physa.2018.03.011
0378-4371/

many properties with suspensions of swimmers, is made by active gels that have been introduced to model mixtures of polar biological filaments with (active) motor proteins [11–13]. Their continuum modeling is based on the liquid-Crystal description of long filaments in the nematic phase supplemented with additional contributions to introduce the motor activity [14,1,2].

Research in this field has been mainly focused on single-component active systems and to a lesser extent on the behavior of solutions of active and passive components. Mixtures of self propelled and passive particles have been studied by Brownian-like simulations [15,16], focusing on the role of activity in separating the two components of the mixtures. Binary fluids with an active component have been considered in [17,18] showing that the active part may cause instabilities on active passive interface. Recently [19] a model has been introduced where emulsification of the active component is favored by the presence of surfactant added to the mixture. This model generalizes the aforementioned active gel theory to describe the behavior of a mixture of isotropic passive and polar active fluids. The goal was to have a system with a tunable amount of active material that can be dispersed homogeneously in the fluid. This would also represent a further important step in the study of active turbulent fluids [20,21] (with the possibility of tuning the intensity but also the spatial distribution of energy input in the system).

In [19] a symmetric mixture of active and passive components was considered. Their equilibrium configurations are dominated by the formation of local ordered lamellae [22–26]. It was shown that activity may modify such a configuration leading to a variety of morphologies whose formation strongly depends on the intensity and the kind of active doping. Indeed, polar active fluids are said to be either extensile (*e.g.* bacterial colonies and microtubules bundles) or contractile (*e.g.* actine and myosin filaments) according to the nature of the stress exerted by the active component on its neighborhood. Furthermore, intensity of active doping can be tuned by keeping under control the amount of fuel available to active particles. This corresponds experimentally to keeping under control the amount of ATP in active gels of bundled microtubles [27] or the amount of oxygen available, the concentration of ingredients, or the temperature in bacterial suspensions. In the present model this is done by introducing a parameter representing the strength of the active stress acting in the system (see Section 2). The main result was that, even if under symmetric conditions, activity modifies lamellar configurations into an emulsion of passive droplets in an active matrix at sufficiently high contractile activity. On the other hand, lamellae change their morphology into rotating active droplets in the extensile case.

In this work we complement the previous analysis by considering a highly off-symmetric mixture with a 10 : 90 ratio of the active and passive components both for extensile and contractile systems. Here the equilibrium state of the fluid is characterized by an ordered array of droplets of the minority phase positioned at the vertices of a triangular lattice. We will show that, despite the strong unbalance between the two components, activity greatly affects the morphology of the system, leading to the development of a wide range of patterns both for the concentration and the velocity field. In the extensile case a small amount of activity favors the elimination of defects in the system, as shown by measuring the number of defects in Voronoi tessellation. By increasing activity, isolated droplets tend to merge forming larger 'islands' of active material and then, at still larger activity, big rotating droplets are observed. In the contractile case activity promotes the rupture of the hexagonal phase and the appearance of a matrix of the active component in the passive flowing background, differently from what happened in the symmetric case. The morphological study is supported by the analysis of the kinetic energy and enstrophy behavior.

The dynamic equations for the concentration of the active material and the polarization, which fixes the average orientation of the active component, are derived from a proper free-energy functional and supplemented with the Navier–Stokes equations for the whole fluid in the incompressible limit. These equations are numerically solved by using a hybrid lattice Boltzmann method [17,28–32].

The paper is organized in the following way. The next Section is devoted to present the thermo-hydrodynamic description of the system, the numerical method, and the set of parameters relevant for the present study. In Sections 3 and 4 the results for the morphology and the corresponding flow patterns will be shown and related to the observed behaviors of energy and enstrophy. Finally, a discussion with some remarks and possible future lines of investigation will conclude the paper.

2. Model

We outline here the hydrodynamic model and the numerical method used to conduct our study. We consider a fluid comprising a mixture of active material and solvent with total mass density ρ. The physics of the resulting composite material can be described by using an extended version of the well-established active gel theory [1,2,17,32–34]. The hydrodynamic variables are the density of the fluid ρ, its velocity $\mathbf{v}$, the concentration of the active material ϕ, and the polarization $\mathbf{P}$, which determines the average orientation of the active material. The dynamic equations ruling the evolution of the system are

$$\rho\left(\frac{\partial}{\partial t}+\mathbf{v}\cdot\nabla\right)\mathbf{v} = -\nabla p+\nabla\cdot\underline{\underline{\sigma}}^{total}, \tag{1}$$

$$\frac{\partial\phi}{\partial t}+\nabla\cdot(\phi\mathbf{v}) = \nabla\cdot\left(M\nabla\frac{\delta F}{\delta\phi}\right), \tag{2}$$

$$\frac{\partial\mathbf{P}}{\partial t}+(\mathbf{v}\cdot\nabla)\,\mathbf{P} = -\underline{\underline{\Omega}}\cdot\mathbf{P}+\xi\underline{\underline{D}}\cdot\mathbf{P}-\frac{1}{\Gamma}\frac{\delta F}{\delta\mathbf{P}}, \tag{3}$$

in the limit of incompressible fluid. The first one is the Navier–Stokes equation, where p is the isotropic pressure and $\underline{\underline{\sigma}}^{total}$ is the total stress tensor [35]. Eqs. (2)–(3) govern the time evolution of the concentration of the active material and of the polarization field, respectively. Since the amount of active material is locally conserved, the time evolution of the concentration field can be written as a convection–diffusion equation, Eq. (2), where M is the mobility, F a free energy functional as defined later, and $\delta F/\delta\phi$ is the chemical potential. The dynamics of the polarization field follows an advection–relaxation equation, Eq. (3), borrowed from polar liquid crystal theory. Here Γ is the rotational viscosity, ξ is a constant controlling the aspect ratio of active particles (positive for rod-like particles and negative for disk-like ones), $h = \delta F/\delta\mathbf{P}$ is the molecular field. $\underline{\underline{D}} = (\underline{\underline{W}}+\underline{\underline{W}}^T)/2$ and $\underline{\underline{\Omega}} = (\underline{\underline{W}}-\underline{\underline{W}}^T)/2$ represent the symmetric and the antisymmetric parts of the velocity gradient tensor $\underline{\underline{W}}_{\alpha\beta} = \partial_\beta v_\alpha$, where Greek indexes denote Cartesian components. These contributions are in addition to the material derivative as the liquid crystal can be rotated or aligned by the fluid [35]. The stress tensor $\underline{\underline{\sigma}}^{total}$ considered in the Navier–Stokes equation of the model, Eq. (1), is split into the equilibrium/passive and non-equilibrium/active part:

$$\underline{\underline{\sigma}}^{total} = \underline{\underline{\sigma}}^{passive} + \underline{\underline{\sigma}}^{active}. \tag{4}$$

The passive part represents elastic response from solutes and is, in turn, the sum of three terms:

$$\underline{\underline{\sigma}}^{passive} = \underline{\underline{\sigma}}^{viscous} + \underline{\underline{\sigma}}^{elastic} + \underline{\underline{\sigma}}^{interface}. \tag{5}$$

The first term is the viscous stress written as $\sigma^{viscous}_{\alpha\beta} = \eta(\partial_\alpha v_\beta + \partial_\beta v_\alpha)$ where η is the shear viscosity. The second term is the elastic stress analogous to the one used in nematic liquid crystal hydrodynamics [35]:

$$\begin{aligned}\sigma^{elastic}_{\alpha\beta} = &\frac{1}{2}(P_\alpha h_\beta - P_\beta h_\alpha) - \frac{\xi}{2}(P_\alpha h_\beta + P_\beta h_\alpha)\\ &- \kappa\,\partial_\alpha P_\gamma \partial_\beta P_\gamma,\end{aligned} \tag{6}$$

where κ is the elastic constant of the liquid crystal and the parameter ξ depends on the geometry, as already mentioned. In addition ξ establishes whether the fluid is flow aligning ($|\xi| > 1$) or flow tumbling ($|\xi| < 1$) under shear. The third term is borrowed from binary mixtures theory. It includes interfacial contribution between the passive and the active phase:

$$\sigma^{interface}_{\alpha\beta} = \left(f - \phi\frac{\delta F}{\delta\phi}\right)\delta_{\alpha\beta} - \frac{\partial f}{\partial\left(\partial_\beta\phi\right)}\partial_\alpha\phi\,. \tag{7}$$

Here f is the free energy density. The active contribution to the stress tensor, not stemming from the free energy, is given by [33,36]

$$\sigma^{active}_{\alpha\beta} = -\zeta\phi\left(P_\alpha P_\beta - \frac{1}{3}|\mathbf{P}|^2\delta_{\alpha\beta}\right), \tag{8}$$

where ζ is the activity strength that is positive for extensile systems (pushers) and negative for contractile ones (pullers). The active stress drives the system out of equilibrium by injecting energy into it and satisfies the symmetry $\mathbf{P} \to -\mathbf{P}$.

The thermodynamics properties of the binary mixture, in absence of activity, are encoded in the following free-energy functional that couples the Landau–Brazovskii model [37] to the distortion free-energy of a polar system:

$$\begin{aligned}F\ [\phi,\mathbf{P}] = \int d\mathbf{r}\,\{&\frac{a}{4\phi_{cr}^4}\phi^2(\phi-\phi_0)^2 + \frac{k}{2}|\nabla\phi|^2 + \frac{c}{2}(\nabla^2\phi)^2\\ &- \frac{\alpha}{2}\frac{(\phi-\phi_{cr})}{\phi_{cr}}|\mathbf{P}|^2 + \frac{\alpha}{4}|\mathbf{P}|^4 + \frac{\kappa}{2}(\nabla\mathbf{P})^2 + \beta\mathbf{P}\cdot\nabla\phi\}\ .\end{aligned} \tag{9}$$

This is a generalization of the free energy functional for active binary mixtures defined in [33]. The first term, multiplied by the phenomenological constant $a > 0$, describes the bulk properties of the fluid, the second and third ones determine the interfacial tension. Notice that here a negative value of k favors the formation of interfaces while a positive value of c has to guarantee the stability of the free-energy [37]. The Landau–Brazovskii model, with only the ϕ terms in the first line of Eq. (9), when the composition is symmetric, has a transition line for $k_{cr} = -\sqrt{8c\tilde{a}/15}$, in the mean field approximation [38], where $\tilde{a} = a\phi_0^2/8\phi_{cr}^4$ is half the coefficient of the ϕ quadratic term in (9). Lowering k from positive to negative values leads the system to move from pure ferromagnetic phase to configurations where interfaces between components are favored; for values lower than k_{cr} the system exhibits a periodic behavior such that the equilibrium state of the system is characterized by lamellae. For asymmetric compositions droplets of the minority phase are stable [22,39,40]. The bulk term is chosen in order to create two free energy minima, one ($\phi = 0$) corresponding to the passive material and the other one ($\phi \simeq \phi_0$) corresponding to the active phase; $\phi_{cr} = \phi_0/2$, where ϕ_{cr} is the critical concentration for the transition from isotropic ($|\mathbf{P}| = 0$) to polar ($|\mathbf{P}| > 0$) states. The bulk properties of the polar liquid crystal are instead controlled by the $|\mathbf{P}|^2$ and $|\mathbf{P}|^4$ terms, multiplied by the positive constant α. The choice of ϕ_{cr} has been made in order to break the symmetry between the two phases and confine the polarization field in the active phase $\phi > \phi_{cr}$. The second last term proportional to $(\nabla\mathbf{P})^2$ describes the energy cost due to elastic deformation in the liquid crystalline phase, gauged by the elastic constant κ (in the single elastic constant approximation). Finally, the last term takes into account the orientation of the polarization at the

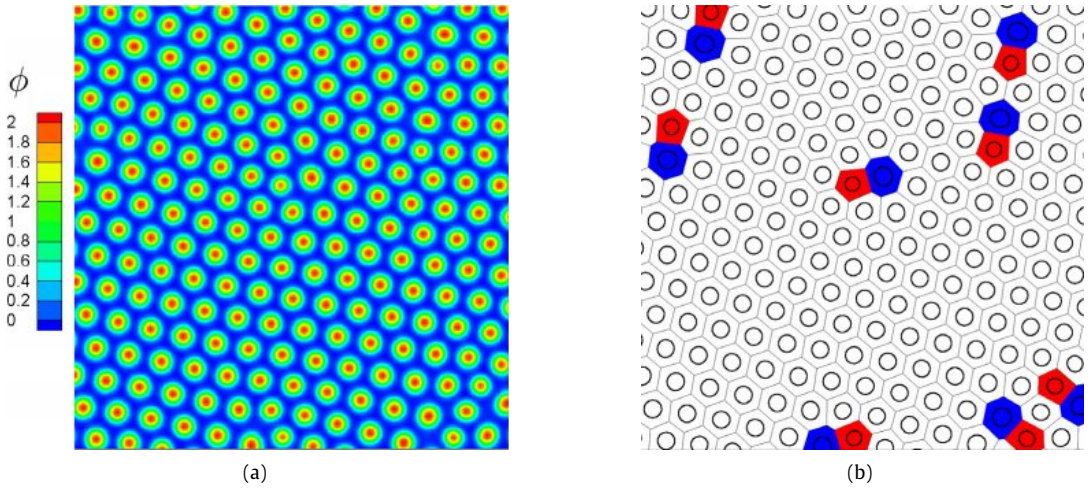

Fig. 1. (a) Snapshot of ϕ contour plot for a configuration in the stationary regime at $\zeta = 0$, for a portion of size $L = 128$, of a system of original size $L = 256$. The color code displayed here is the same of all the contour plots in the rest of the work. (b) Voronoi tessellation for the same configuration in (a). (For interpretation of the references to color in this figure legend, the reader is referred to the web version of this article.)

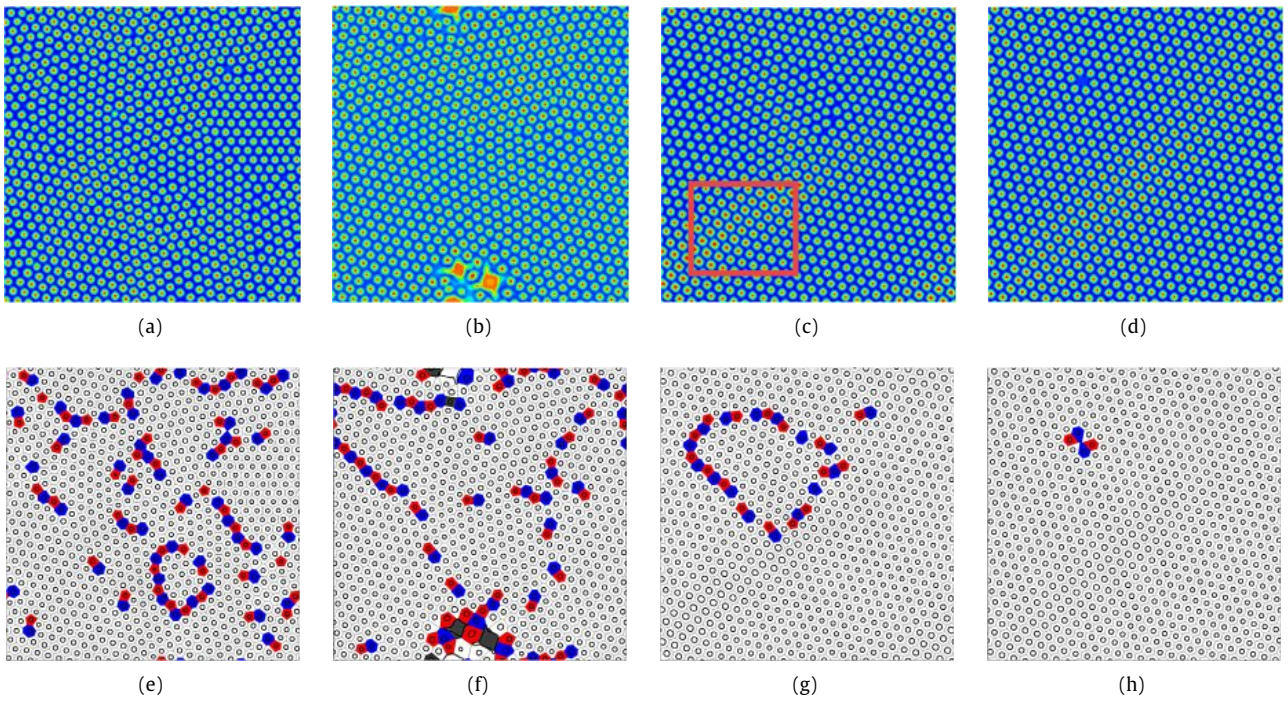

Fig. 2. Snapshots of ϕ contour plots (upper panels), and corresponding Voronoi tessellation (lower panels) at times 2×10^5 (a), 12×10^5 (b), 40×10^5 (c), 62×10^5 (d) for $\zeta = 0.006$ on a lattice of size $L = 256$. The box in Fig. 2c indicates a region in which the droplet size is bigger compared to the rest of the system. The final configuration (Fig. 2h) is almost-completely hexatically ordered as witnessed by the presence of very few defects. These latter ones are in correspondence of the hole visible in Fig. 2d in the same position.

interface of the fluid. If $\beta \neq 0$, $\mathbf{P}$ preferentially points perpendicularly to the interface (normal anchoring): towards the passive (active) phase if $\beta > 0$ ($\beta < 0$).

The equations of motion of the exotic polar active emulsion, Eqs. (1)–(3), are solved by means of a hybrid lattice Boltzmann (LB) scheme, which combines a LB treatment for the Navier–Stokes equation (see Appendix for more details) with a finite-difference predictor–corrector algorithm to solve the order parameter dynamics. Simulations have been performed on a periodic square lattice of size $L = 256$. The concentration ϕ ranges from $\phi \simeq 0$ (passive phase) to $\phi \simeq 2$ (active phase). Unless otherwise stated, parameter values are $a = 4 \times 10^{-3}$, $k = -6 \times 10^{-3}$, $c = 10^{-2}$, $\alpha = 10^{-3}$, $\kappa = 10^{-2}$, $\beta = 0.01$, $\Gamma = 1$, $\xi = 1.1$, $\phi_0 = 2.0$, and $\eta = 1.67$. All quantities in the text are reported in lattice units.

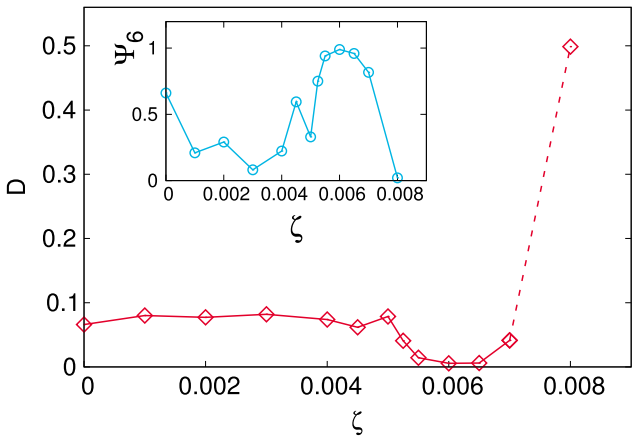

Fig. 3. (Main figure) Defects ratio (droplets without 6 neighbors over the total number of droplets in the configuration) vs. activity, in the stationary time regime, for systems of size $L = 256$. The figurative dashed line stands for the fact that increasing activity it is no more possible a coherent defects analysis, due to the formation of asters first and completely non definite structures for strong activity (see next figures). **(Inset)** Global hexatic order parameter (10) as a function of activity.

We have considered a 10 : 90 mixture of the active and passive component following two initialization procedures. In one case we started from a random configuration of polarization and concentration. The latter has been initialized considering a random variation of ten percent around its average value. Starting from this configuration, the system has been equilibrated without activity. Then, activity has been switched on and the evolution of the system studied. In the other procedure the random initial configuration has been evolved in the presence of activity. We checked that the two procedures lead to the same behavior at late times. The results presented in the following generally are obtained with the second initialization procedure.

3. Extensile case

3.1. Small activity, hexatic order, and defects

Having in mind to fully characterize the behavior of the system as the value of activity changes, we begin by considering the case when the activity is off. In this case, at equilibrium, the system is characterized by an ordered array of droplets as can be seen looking at the contour plot of the concentration ϕ in Fig. 1a. The droplets (and their centers of mass) can be easily pinpointed by putting a proper cutoff on the concentration field to distinguish active regions from passive ones. Each closed region of lattice sites that falls beyond the cutoff, is identified as a droplet. A good choice for the cutoff with our choice of the parameters is seen to be $\phi \sim 1.5$. Droplets are hexatically ordered, that is they occupy vertices of a triangular lattice, besides the presence of some defects. A *Voronoi tessellation* is used in order to unambiguously identify the nearest-neighbors network for the centers of mass of each droplet. Voronoi tessellation establishes a partitioning of the space with one closed region for each center of mass, according to the following rule: the region associated to the ith droplet contains all the points of the space that are closer to its center of mass than to any other droplets. In Fig. 1b it is shown the use of this analysis. Droplets with 5 nearest neighbors are highlighted in red, while those with 7 neighbors in blue. Observe that most of the defects appear in pairs indicating the presence of dislocations in the system [41].

For non-zero, but still small (positive) values of ζ, the *hexatic-droplet* phase survives. At sufficiently high values of ζ, but still in the small activity regime, activity is able to reduce the number of defects, driving the system in an almost completely ordered phase, as shown in the time evolution of Fig. 2, at $\zeta = 0.006$. The system first forms transient differently-oriented domains bounded by grain-boundary defects (an example of a closed grain boundary is shown in Fig. 2g), then they shrink during the time evolution and disappear at the end, leaving a single hole in the layout. We checked that if instead of switching on activity from the beginning, we start from configurations equilibrated without activity, and then we switch it on, the defects dynamics is not significantly affected. In the course of this evolution we also observe other features, here only transient, that play a major role at larger activity. In Fig. 2b few larger aster-like droplets are observed. We refer as *aster-like droplets*, big rotating droplets or simply *asters* to non-circular droplets which have the shape of an aster associated to the formation of vortices in the velocity field, as will be seen later. The presence of these aster-like droplets will be a predominant feature in the large activity regime as will be seen further in the text. We observe also a slight increase of droplets size during time evolution of the system as highlighted in Fig. 2c. At the end, for $\zeta = 0.006$ and slightly larger values of ζ, activity is such to let the droplets rearrange in an almost defect-free final configuration. To better understand the effect of activity on the hexatic arrangement we plot in Fig. 3 the defects ratio D (with respect to the number of droplets) as the activity varies. We see that for very small values of activity, the hexatic order survives but there is no appreciable change in the number of defects with respect to the passive limit. However, for values of ζ around 0.006, or slightly larger, for the longest

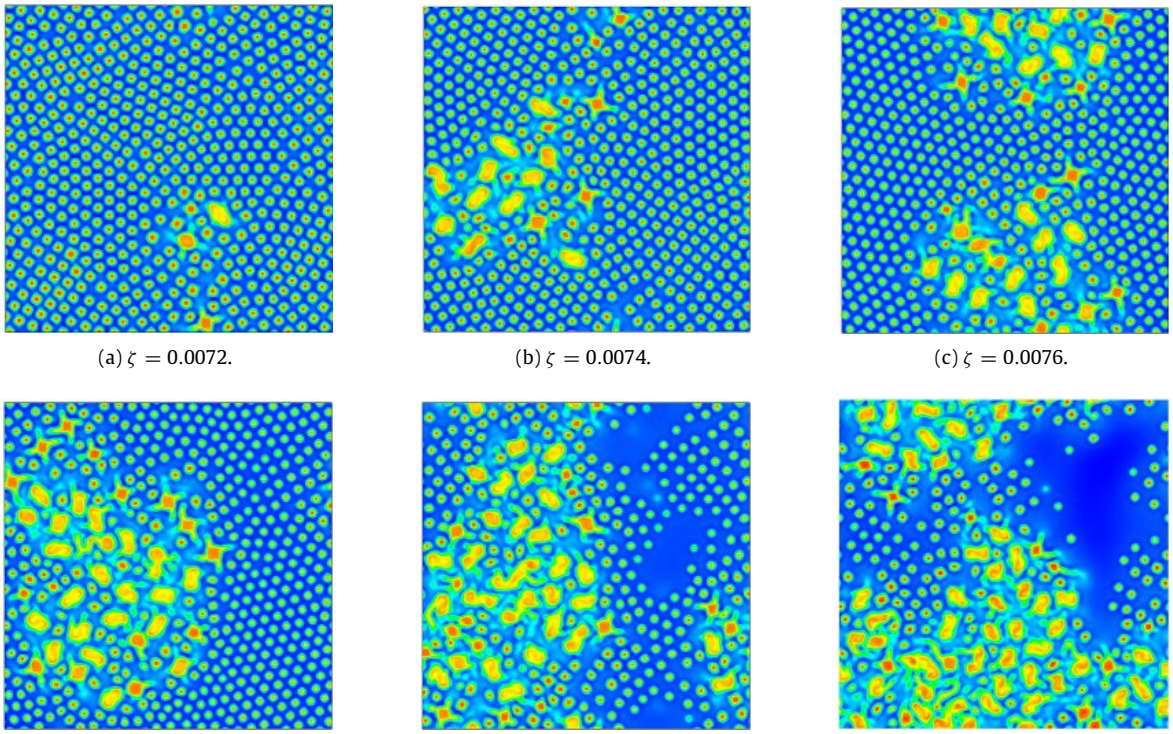

(a) $\zeta = 0.0072$. (b) $\zeta = 0.0074$. (c) $\zeta = 0.0076$.

(d) $\zeta = 0.0078$. (e) $\zeta = 0.0080$. (f) $\zeta = 0.0090$.

Fig. 4. Snapshots of ϕ contour plots at late times for different choices of $\zeta > 0$, for a lattice of size $L = 256$.

simulated times, the hexatic order is enhanced as activity is such to remove the defects. At larger values of ζ a change in the overall morphological behavior of the mixture will be observed and the defects analysis looses significance. In order to further characterize order in the droplet phase we use a *hexatic order parameter*, as the one used for studying hexatic order and phase transitions in two-dimensional systems [42]. Local hexatic order parameter and its global average are defined, as in [43], by

$$\psi_{6i} = \frac{1}{N_i}\sum_{j=1}^{N_i} \exp 6\mathrm{i}\theta_{ij}, \qquad \Psi_6 = \frac{1}{N}\left|\sum_{i=1}^{N}\psi_{6i}\right|, \tag{10}$$

where N_i is the number of neighbors of the ith droplet, θ_{ij} is the angle that droplets i and j form with a reference axis, and N is the total number of droplets. As shown in the inset of Fig. 3, the measure of Ψ_6 is consistent with the picture found by looking at the number of defects. As activity is increased from 0, the global hexatic parameter fluctuates around a positive value, which means that the system is partially hexatically ordered except for some defects. Within the activity range where we see no defects, Ψ_6 reaches its saturation value 1, being the system in a perfectly ordered phase.

3.2. Larger activity and aster-like droplets

Starting from $\zeta = 0.0072$ aster-like droplets are no more transient and the system morphology, at late times, becomes dominated by the presence of these structures.[1] The transition to this regime can be analyzed, qualitatively, looking at the panels in Fig. 4. Here a series of snapshots of ϕ contour plots for different values of activity are reported, starting from $\zeta = 0.0072$ up to $\zeta = 0.0090$. A small number of isolated aster-like droplets linger at late times for $\zeta = 0.0072$ (Fig. 4a), while for bigger values of activity these structures start grouping (Fig. 4b) filling progressively a large portion of the system (Figs. 4d–4f) at the expense of small droplets. The mechanism of formation of the aster-like droplets can be intuited looking at Figs. 4a and 4b. First, bigger droplets thicken in a portion of the system, leading two of them to merge, then the new big droplet starts rotating while incorporating neighboring droplets until an aster-like structure is fully stable. The time evolution of the kinetic energy per unit volume $E_k = \sum_{\mathbf{r}} \rho \mathbf{v}(\mathbf{r})^2/2$, for $\zeta = 0.0072$, is shown in Fig. 5 (blue curve) and reproduces the aster formation: The system sits in the droplet configuration with a constant value of kinetic energy density until the merging of the two droplets leads to a strong discontinuity in the energy density. When the aster-like droplets are

[1] We checked the behavior until $t = 3.5 \times 10^6$ as can be seen from the time evolution of the kinetic energy in Fig. 5.

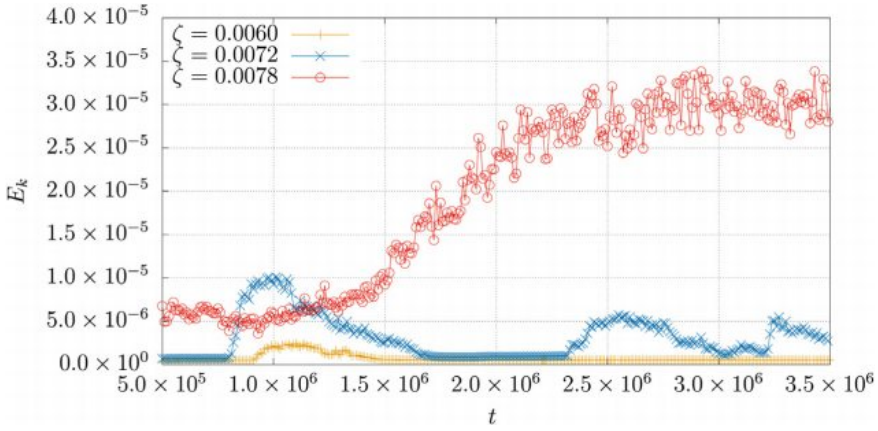

Fig. 5. Time evolution of kinetic energy for different values of ζ. The **middle blue** curve is the time evolution for the same system of Fig. 4a. For $\zeta = 0.006$ (**bottom yellow** curve) the peak corresponds to the formation of asters as explained in the text but at late times the stationary state is characterized by an hexatic order and the kinetic energy goes to zero. The **top red** curve corresponds to the case $\zeta = 0.0078$ and is displayed in order to show that the system reach a stationary state.

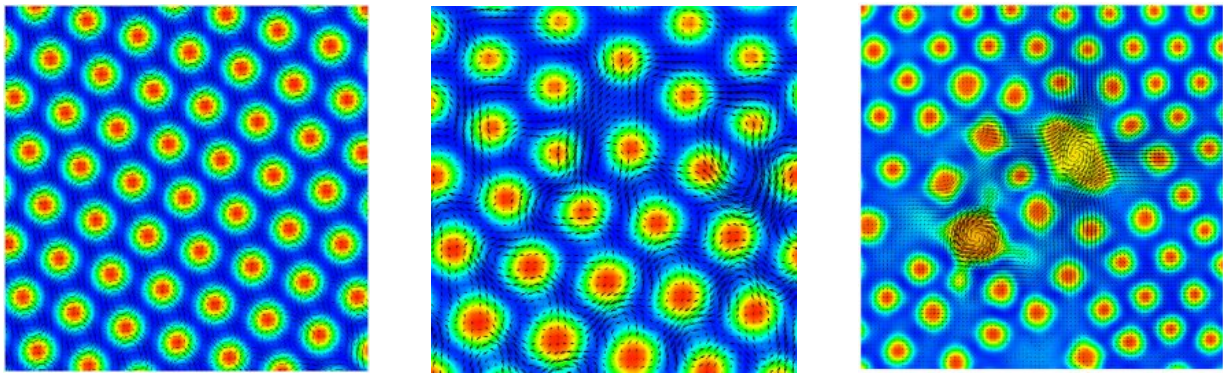

(a) $\zeta = 0.0030$. (b) $\zeta = 0.006$. (c) $\zeta = 0.0072$.

Fig. 6. Snapshots of ϕ contour plots with superimposed the velocity field at late times with different choices of $\zeta > 0$, for a portion of size $L = 120$ for cases (a) and (c), and of size $L = 100$ for case (b), of a system of original size $L = 256$. Averaged modules, over lattice sites, of velocities for the three cases are 3.473×10^{-4}, 7.232×10^{-4} and 1.974×10^{-3} respectively.

fully stable, there is a strong contribution to the kinetic energy coming from their angular velocity. These structures then begin to slow down until they disappear, and the energy density returns to a lower constant value. Then, again, new asters are formed and do not disappear even at late times. In contrast, at lower activity (yellow curve in Fig. 5, for $\zeta = 0.006$) asters disappear and the kinetic energy goes to zero remaining constant for the time checked. The red curve in Fig. 5 corresponds to the case $\zeta = 0.0078$. The kinetic energy is appreciably greater then the previous cases and increases until a stationary state is reached. For this value of activity asters are continuously formed and never disappear in the system.

The velocity field at different activities is displayed in Fig. 6. We see that the resulting aster-like droplets (Fig. 6c) have a velocity field much stronger that the one around droplets (see caption of Fig. 6c). They behave as a vortical source for the velocity field and for this reason we refer to them also as big rotating droplets. The velocity field as activity varies reproduces the behaviors so far discussed. At $\zeta = 0.006$ (Fig. 6b) we distinguish vortical structures that are not localized anymore in correspondence of the droplets, as for smaller values of the activity (Fig. 6a), but start mixing with neighboring vortices.

3.3. Very large activity and overview

At even larger values of activity ($\zeta \gtrsim 0.01$) the aster-like structures are destroyed by the flow and no clear morphological pattern can be observed. The system appears completely mixed as it will be shown.

A better characterization of the behavior of the system in this regime comes from the study of hydrodynamic quantities such as the kinetic energy per unit volume E_k and the enstrophy per unit volume defined as $\varepsilon = \sum_{\mathbf{r}} \omega(\mathbf{r})^2/2$, where $\omega_i = \epsilon_{ijk}\partial_j v_k$ is the vorticity vector and ϵ_{ijk} is the completely anti-symmetric Levi-Civita tensor. Kinetic energy represents a measure of the strength of fluid flows in the system, while enstrophy can be used to figure out whether the velocity field has developed vortical structures. The graphs in Fig. 7 show the behavior of energy and enstrophy averaged in time over

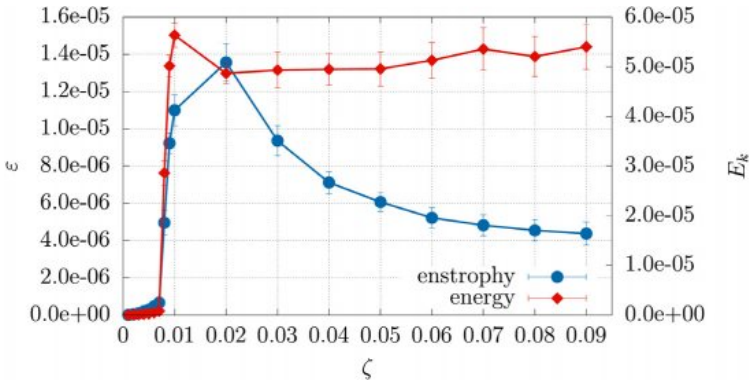

Fig. 7. Plot of kinetic energy and enstrophy per unit volume averaged in time as functions of $\zeta > 0$.

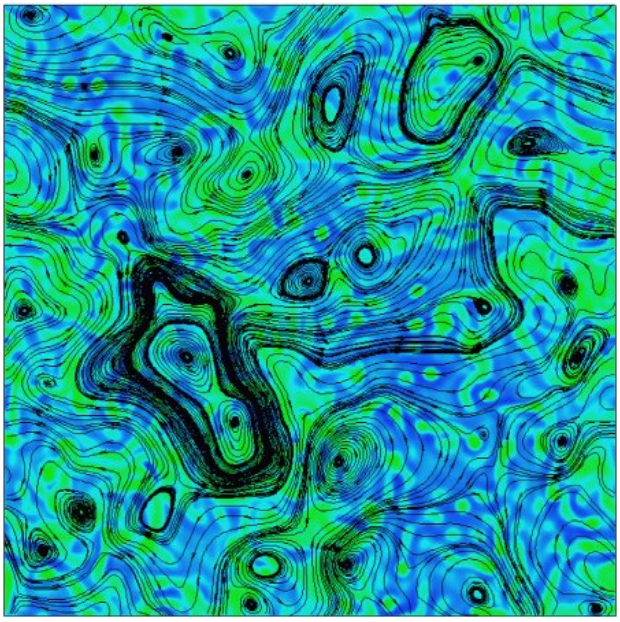

Fig. 8. Snapshots of ϕ contour plot with superimposed streamtraces, at late times, for $\zeta = 0.09$, for a lattice of size $L = 256$. The color code is the same of that displayed in Fig. 1a. The prevalence of green regions means that the system is almost completely mixed. (For interpretation of the references to color in this figure legend, the reader is referred to the web version of this article.)

uncorrelated configurations as functions of the activity. They are both null for $\zeta = 0$ and raise to reach a peak in the range $0.01 - 0.02$. Values are significantly different from 0 at $\zeta = 0.0072$ and this corresponds to the formation of vortical asters. If activity is raised over $\zeta \simeq 0.007$, the number of vortical structures increases until $\zeta \simeq 0.02$. For larger values of ζ asters become unstable and flexible, elongated rotating structures are formed until one arrives at configurations like that of Fig. 8, at $\zeta = 0.09$, with the velocity field exhibiting a pattern like the one shown. When these structures start melting, rotational contribution to the kinetic energy starts decreasing while the kinetic energy stays approximately constant. In this regime weak vortical flows span the system. Such flows dissipate energy while moving, according to the dissipative nature of the fluid, and weaken in intensity until they expire in small and slow vortices or simply merge in more intense flows as suggested by the streamtraces displayed in Fig. 8.

4. Contractile case

We now consider the case of contractile ($\zeta < 0$) emulsions. For slightly negative values of ζ, configurations at late times are similar to the extensile case.

Increasing $|\zeta|$, the hexatic order is progressively lost: First a change in the droplet dimension and shape is observed, as it can be seen in Fig. 9a. This leads the fluid flow to assume different configurations throughout the system. At very low contractile activity, not shown, the velocity field is small in magnitude and enforced in regions close to droplets creating vortical structures that rotate around the center of the droplets themselves. For values of activity, such as $\zeta = -0.008$,

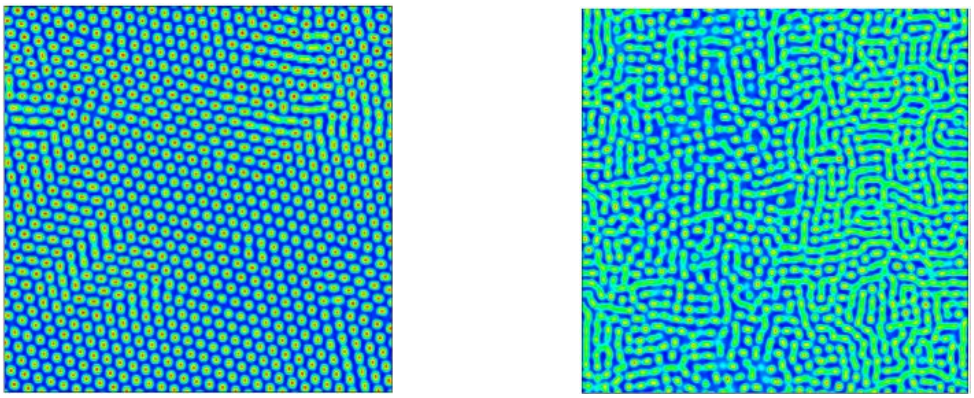

(a) $\zeta = -0.008$. (b) $\zeta = -0.02$.

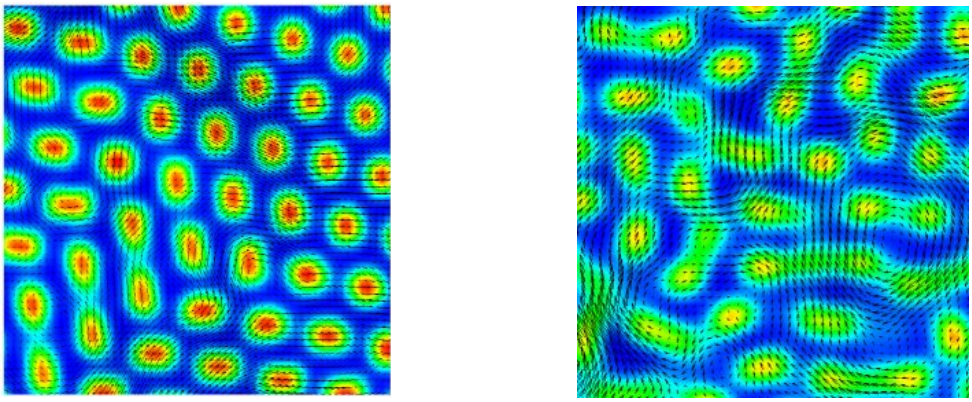

(c) $\zeta = -0.008$. (d) $\zeta = -0.02$.

Fig. 9. (a)–(b) Snapshots of ϕ contour plots at late time for different choices of $\zeta < 0$, for a system of size $L = 256$. (c)–(d) Snapshots of ϕ contour plots with superimposed the velocity field at late times, for the same choices of $\zeta < 0$ as in (a) and (b) respectively, for a portion of size $L = 70$ of a system of original size $L = 256$. Averaged modules, over lattice sites, of velocities for the two cases are 9.201×10^{-4} and 1.143×10^{-3} respectively.

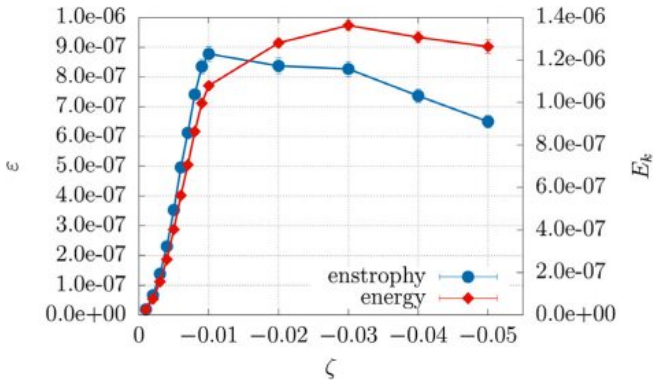

Fig. 10. Plot of energy and enstrophy per unit volume as functions of ζ. Both energy and enstrophy are two order of magnitude less compared to the extensile case (Fig. 5). This is mainly due to the absence of asters in this case.

droplets start oscillating, following the flow (Fig. 9c) and, eventually, merging (see Figs. 9a and 9c) thus creating elongated structures. For large enough activity the hexagonal pattern is lost (Fig. 9b). Flow fields are sustained by the active stress that continuously drives energy into the system and generates flows that are not confined around the droplets anymore, but move throughout the system as it is shown in Fig. 9d. This happens for values of ζ ranging from -0.01 to -0.02 but for even stronger values, the merging of structures throughout the system affects the equilibrium configuration so strongly that when $\zeta \lesssim -0.02$, it is not possible to distinguish any kind of definite pattern anymore.

Here again, together with the morphology it is useful to look at the behavior of the kinetic energy and enstrophy per unit volume. The graphs in Fig. 10 show their behaviors averaged in time over uncorrelated configurations of the system for

different values of the activity ζ. Both energy and enstrophy are null when $\zeta = 0$, according to the fact that in absence of an energy source no fluid flow can be sustained in a dissipative fluid; then they increase until $\zeta \simeq -0.01$ when enstrophy reaches a peak. This trend fits the morphology behavior presented before: As far as droplets are preserved, the velocity field creates vortical structures around them that raise in strength for stronger values of activity, but when the merging of droplets starts affecting the morphology, the local vortical structures are progressively replaced by flows without ordered structure. This brings energy to stay approximatively constant for values $\zeta \lesssim -0.02$ while enstrophy collapses rapidly.

5. Conclusions and perspectives

This work shows how activity modifies the equilibrium hexatic-ordered droplets configuration of an highly asymmetric active emulsion.

In the extensile case we found three different regimes. For ζ up to 0.005 hexatic order is preserved, while is enhanced for values of ζ around 0.006, which is the critical value for a transition to a regime dominated by big-rotating droplets. In fact, starting from $\zeta = 0.0072$ the system morphology becomes characterized by the presence of aster-like droplets. At even larger values of activity ($\zeta \gtrsim 0.01$) the aster-like structures are destroyed by the flow and the system appears completely mixed. We have scored the transitions studying energy and enstrophy behaviors. In the case of contractile emulsions, for slightly negative values of ζ stationary configurations are similar to the extensile case while, strong contractile activity gives rise to elongated structures.

In the future we plan to extend these studies to three dimensional systems, where even richer morphologies ad flow patterns ca be expected.

Acknowledgments

Simulations have been performed at Bari ReCaS e-Infrastructure funded by MIUR, Italy through the program PON Research and Competitiveness 2007–2013 Call 254 Action I. We thank D. Marenduzzo, A. Tiribocchi and F. Bonelli for the very useful discussions.

Appendix. Numerical method

In the LB scheme the evolution of the fluid is defined in terms of a set of N discrete distribution functions $\{f_i\}$ ($i = 0, \ldots, N-1$) which obey the dimensionless Boltzmann equation in the BGK approximation:

$$\begin{aligned} &f_i(\mathbf{r} + \mathbf{e}_i \Delta t, t + \Delta t) - f_i(\mathbf{r}, t) \\ &= -\frac{\Delta t}{\tau}[f_i(\mathbf{r}, t) - f_i^{eq}(\mathbf{r}, t)] \,, \end{aligned} \tag{A.1}$$

where $\mathbf{r}$ and t are the spatial coordinates and the time, respectively, $\{\mathbf{e_i}\}$ ($i = 0, \ldots, N-1$) is the set of discrete velocities, Δt is the time step, and τ is a relaxation time which characterizes the relaxation towards the equilibrium distributions f_i^{eq}. The shear viscosity η is related to τ by the relationship $\eta = c^2 \Delta t \frac{2\tau - 1}{6}$. The value of N depends on the space dimensions and the lattice geometry. The moments of the distribution functions allow to write the conservation laws for the density and total momentum in the form:

$$\begin{aligned} &\sum_i f_i^{eq} = \rho \\ &\sum_i f_i^{eq} e_{i\alpha} = \rho \mathbf{v}_\alpha \,. \end{aligned} \tag{A.2}$$

The second moment, which describes the balance between energetic densities at stake, is fixed in order to find the hydrodynamic equations in the continuum limit. It is given by

$$\sum_i f_i^{eq} e_{i\alpha} e_{i\beta} = \Pi_{\alpha\beta} + \rho \mathbf{v}_\alpha \mathbf{v}_\beta \,, \tag{A.3}$$

where $\Pi_{\alpha\beta}$ represents the pressure tensor. Introducing the nematic tensor $Q_{\alpha\beta} = \mathbf{P}_\alpha \mathbf{P}_\beta - \frac{1}{3}|\mathbf{P}^2|\delta_{\alpha\beta}$, the pressure tensor can be written as

$$\begin{aligned} \Pi_{\alpha\beta} = &-p\delta_{\alpha\beta} + 2\xi(Q_{\alpha\beta} + \frac{1}{3}\delta_{\alpha\beta})Q_{\gamma\epsilon}H_{\gamma\epsilon} \\ &- \xi H_{\alpha\gamma}(Q_{\gamma\beta} + \frac{1}{3}\delta_{\gamma\beta}) - \xi(Q_{\alpha\gamma} + \frac{1}{3}\delta_{\alpha\gamma})H_{\gamma\beta} \\ &- \partial_\alpha Q_{\gamma\nu}\frac{\delta f}{\delta(\partial_\beta Q_{\gamma\nu})} + Q_{\alpha\gamma}H_{\gamma\beta} - H_{\alpha\gamma}Q_{\gamma\beta} \,, \end{aligned} \tag{A.4}$$

Table A.1
Equilibrium distribution coefficients.

$A_0 = \rho - 20A_2$	$A_1 = 4A_2$	$A_2 = \frac{[\Pi_{\alpha\beta} + \mathbf{v}\zeta(Q_{\alpha\beta} + \frac{1}{3}\delta_{\alpha\beta})]\delta_{\alpha\beta}}{24\mathbf{v}^2}$
$B_0 = 0$	$B_1 = 4B_2$	$B_2 = \rho/12\mathbf{v}^2$
$C_0 = -2\rho/3\mathbf{v}^2$	$C_1 = 4C_2$	$C_2 = -\rho/24\mathbf{v}^2$
$D_0 = 0$	$D_1 = 8D_2$	$D_2 = \rho/8\mathbf{v}^2$
$G_{0\alpha\beta} = 0$	$G_{1\alpha\beta} = 4G_{2\alpha\beta}$	$G_{2\alpha\beta} = \frac{[\Pi_{\alpha\beta} - \frac{1}{2}\Pi_{\delta\delta}\delta_{\alpha\beta} + \mathbf{v}\zeta(Q_{\alpha\beta} + \frac{1}{3}\delta_{\alpha\beta})]}{8\mathbf{v}^4}$

where H is the field conjugated to the nematic tensor and p the ideal gas pressure.

The equilibrium distributions are expanded up to the second order in the velocities

$$f_k^{eq} = A_k + B_k \mathbf{v}_\alpha e_{k\alpha} + C_k \mathbf{v}^2 + D_k \mathbf{v}_\alpha \mathbf{v}_\beta e_{k\alpha} e_{k\beta} + G_{k\alpha\beta} e_{k\alpha} e_{k\beta} \,, \tag{A.5}$$

where the index k labels the different directions on the discretized lattice. The A_k, B_k, C_k, D_k and $G_{k\alpha\beta}$ are characteristic parameters to be determined to get the right hydrodynamic equations in the continuum limit by imposing the conditions given by Eqs. (A.2)–(A.3). For a two-dimensional square lattice with $N = 9$ velocities (D2Q9), which is the model here considered, these parameters are reported in Table A.1, and the lattice velocities are $\mathbf{e}_0 = (0, 0)$, $\mathbf{e}_{1,2} = (\pm u, 0)$, $\mathbf{e}_{3,4} = (0, \pm u)$, $\mathbf{e}_{5,6} = (\pm u, \pm u)$, $\mathbf{e}_{7,8} = (\mp u, \pm u)$ with $u = \Delta x/\Delta t$, Δx being the lattice mesh size. In Table A.1 $k = 0$ corresponds to the rest lattice velocity, while $k = 1$ and $k = 2$ correspond to the velocities directed towards the first and second neighbors, respectively.

The LB scheme is coupled with a finite-difference predictor–corrector algorithm, in order to solve simultaneously Eqs. (1)–(3). This method was previously used to study the hydrodynamics of binary fluids [28,44], liquid crystals and active matter [30,45].

References

[1] S. Ramaswamy, The mechanics and statistics of active matter, Annu. Rev. Condens. Matter Phys. 1 (1) (2010) 323–345.
[2] M.C. Marchetti, J.F. Joanny, S. Ramaswamy, T.B. Liverpool, J. Prost, M. Rao, R.A. Simha, Hydrodynamics of soft active matter, Rev. Modern Phys. 85 (2013) 1143–1189.
[3] J. Elgeti, R.G. Winkler, G. Gompper, Physics of microswimmers—single particle motion and collective behavior: a review, Rep. Progr. Phys. 78 (5) (2015) 056601.
[4] C. Bechinger, R. Di Leonardo, H. Löwen, C. Reichhardt, G. Volpe, G. Volpe, Active particles in complex and crowded environments, Rev. Modern Phys. 88 (2016) 045006.
[5] G. Gonnella, D. Marenduzzo, A. Suma, A. Tiribocchi, Motility-induced phase separation and coarsening in active matter, C. R. Phys. 16 (3) (2015) 316–331.
[6] T. Vicsek, A. Czirók, E. Ben-Jacob, I. Cohen, O. Shochet, Novel type of phase transition in a system of self-driven particles, Phys. Rev. Lett. 75 (1995) 1226–1229.
[7] M.E. Cates, J. Tailleur, Motility-induced phase separation, Annu. Rev. Condens. Matter Phys. 6 (1) (2015) 219–244.
[8] A. Suma, G. Gonnella, G. Laghezza, A. Lamura, A. Mossa, L.F. Cugliandolo, Dynamics of a homogeneous active dumbbell system, Phys. Rev. E 90 (2014) 052130.
[9] F.D.C. Farrell, M.C. Marchetti, D. Marenduzzo, J. Tailleur, Pattern formation in self-propelled particles with density-dependent motility, Phys. Rev. Lett. 108 (2012) 248101.
[10] G.S. Redner, M.F. Hagan, A. Baskaran, Structure and dynamics of a phase-separating active colloidal fluid, Phys. Rev. Lett. 110 (2013) 055701.
[11] J. Prost, F. Jülicher, J.-F. Joanny, Active gel physics, Nat. Phys. 11 (2) (2015) 111.
[12] J.-F. Joanny, J. Prost, Active gels as a description of the actin-myosin cytoskeleton, HFSP J. 3 (2) (2009) 94–104.
[13] D. Marenduzzo, E. Orlandini, Hydrodynamics of non-homogeneous active gels, Soft Matter 6 (4) (2010) 774–778.
[14] J. Toner, Y. Tu, S. Ramaswamy, Hydrodynamics and phases of flocks, Ann. Phys. 318 (1) (2005) 170–244. Special Issue.
[15] S.R. McCandlish, A. Baskaran, M.F. Hagan, Spontaneous segregation of self-propelled particles with different motilities, Soft Matter 8 (8) (2012) 2527–2534.
[16] A.Y. Grosberg, J.-F. Joanny, Nonequilibrium statistical mechanics of mixtures of particles in contact with different thermostats, Phys. Rev. E 92 (2015) 032118.
[17] E. Tjhung, D. Marenduzzo, M.E. Cates, Spontaneous symmetry breaking in active droplets provides a generic route to motility, Proc. Natl. Acad. Sci. USA 109 (31) (2012) 12381–12386.
[18] M.L. Blow, S.P. Thampi, J.M. Yeomans, Biphasic, lyotropic, active nematics, Phys. Rev. Lett. 113 (2014) 248303.
[19] F. Bonelli, L.N. Carenza, G. Gonnella, D. Marenduzzo, E. Orlandini, A. Tiribocchi, Lamellar ordering, droplet formation and phase inversion in exotic active emulsions, (submitted on 16.02.18) to arXiv:cond-mat.
[20] S.P. Thampi, J. Yeomans, Active turbulence in active nematics, Eur. Phys. J. Spec. Top. 225 (4) (2016) 651–662.
[21] L. Giomi, Geometry and topology of turbulence in active nematics, Phys. Rev. X 5 (2015) 031003.
[22] V. Kumaran, Y.K.V.V.N.K. Babu, J. Sivaramakrishna, Multiscale modeling of lamellar mesophases, J. Chem. Phys. 130 (11) (2009) 114907.
[23] F. Corberi, G. Gonnella, A. Lamura, Ordering of the lamellar phase under a shear flow, Phys. Rev. E 66 (2002) 016114.
[24] A. Lamura, G. Amati, A. Xu, G. Gonnella, F. Massaioli, Scaling and hydrodynamic effects in lamellar ordering, Europhys. Lett. 71 (4) (2005) 651–657.
[25] G. Gonnella, A. Xu, A. Lamura, Morphologies and flow patterns in quenching of lamellar systems with shear, Phys. Rev. E 74 (1) (2006) 011505.
[26] V. Kumaran, Mesoscale description of an asymmetric lamellar phase, J. Chem. Phys. 130 (22) (2009) 224905.
[27] Gil Henkin, Stephen J. DeCamp, Daniel T.N. Chen, Tim Sanchez, Zvonimir Dogic, Tunable dynamics of microtubule-based active isotropic gels, Philosophical Transactions of the Royal Society of London A: Mathematical, Physical and Engineering Sciences 372 (2029) (2014).

[28] A. Tiribocchi, N. Stella, G. Gonnella, A. Lamura, Hybrid lattice Boltzmann model for binary fluid mixtures, Phys. Rev. E 80 (2009) 026701.
[29] A. Tiribocchi, G. Gonnella, D. Marenduzzo, E. Orlandini, F. Salvadore, Bistable defect structures in blue phase devices, Phys. Rev. Lett. 107 (2011) 237803.
[30] M.E. Cates, O. Henrich, D. Marenduzzo, K. Stratford, Lattice boltzmann simulations of liquid crystalline fluids: active gels and blue phases, Soft Matter 5 (2009) 3791–3800.
[31] G. De Magistris, A. Tiribocchi, C.A. Whitfield, R.J. Hawkins, M.E. Cates, D. Marenduzzo, Spontaneous motility of passive emulsion droplets in polar active gels, Soft Matter 10 (2014) 7826–7837.
[32] E. Tjhung, A. Tiribocchi, D. Marenduzzo, M.E. Cates, A minimal physical model captures the shapes of crawling cells, Nat. Commun. 6 (2015) 5420.
[33] E. Tjhung, M.E. Cates, D. Marenduzzo, Nonequilibrium steady states in polar active fluids, Soft Matter 7 (2011) 7453–7464.
[34] K. Kruse, J.F. Joanny, F. Jülicher, J. Prost, K. Sekimoto, Asters, vortices, and rotating spirals in active gels of polar filaments, Phys. Rev. Lett. 92 (2004) 078101.
[35] A.N. Beris, B.J. Edwards, Thermodynamics of Flowing Systems, in: Oxford Engineering Science Series, Oxford University Press, 1994.
[36] R. Aditi Simha, S. Ramaswamy, Hydrodynamic fluctuations and instabilities in ordered suspensions of self-propelled particles, Phys. Rev. Lett. 89 (2002) 058101.
[37] S.A. Brazovskiĭ, Phase transition of an isotropic system to a nonuniform state, J. Exp. Theor. Phys. 41 (1975) 85.
[38] G. Gompper, S. Zschocke, Ginzburg-Landau theory of oil-water-surfactant mixtures, Phys. Rev. A 46 (1992) 4836–4851.
[39] G. Gompper, C. Domb, M.S. Green, M. Schick, J.L. Lebowitz, Phase Transitions and Critical Phenomena: Self-assembling amphiphilic systems, in: Phase transitions and critical phenomena, Academic Press, 1994.
[40] E. Orlandini, G. Gonnella, J.M. Yeomans, Lattice boltzmann simulations of lamellar and droplet phases, Phys. Rev. E 58 (1998) 480–485.
[41] P.M. Chaikin, T.C. Lubensky, Principles of Condensed Matter Physics, Cambridge University Press, 2000.
[42] B.I. Halperin, David R. Nelson, Theory of two-dimensional melting, Phys. Rev. Lett. 41 (1978) 121–124.
[43] Leticia F. Cugliandolo, Pasquale Digregorio, Giuseppe Gonnella, Antonio Suma, Phase coexistence in two-dimensional passive and active dumbbell systems, Phys. Rev. Lett. 119 (2017) 268002.
[44] A. Lamura, G. Gonnella, A. Tiribocchi, Thermal and hydrodynamic effects in the ordering of lamellar fluids, Phil. Trans. R. Soc. A 369 (1945) (2011) 2592–2599.
[45] A. Tiribocchi, F. Bonelli, G. Gonnella, D. Marenduzzo, Spontaneous flow in polar active fluids: the effect of a phenomenological self propulsion-like term, Eur. Phys. J. E 39 (1) (2016) 1.

EPJ manuscript No.
(will be inserted by the editor)

Lattice Boltzmann Methods and Active Fluids

Giuseppe Gonnella[1], Giuseppe Negro[1], Nicola Carenza[1], Antonio Lamura[2], and Adriano Tiribocchi[3]

[1] Dipartimento di Fisica and Sezione INFN, Università degli Studi di Bari, 70126 Bari, Italy
[2] Istituto Applicazioni Calcolo, CNR, Via Amendola 122/D, 70126 Bari, Italy
[3] Dipartimento di Fisica and Sezione INFN, Università degli Studi di Padova, I-35131 Padova, Italy

Received: date / Revised version: date

Abstract. Insert your abstract here.

1 Introduction

The goal of this article is to describe the use of Lattice Boltzmann Methods in the study of large scale properties of active fluids [1–6], showing also recent progress in few relevant topics. Active fluids are living matter or biologically inspired systems with the common characteristic of being composed by self-propelled (or active) units that burn stored or ambient energy into work or systematic movement. An example in nature is given by the cell cytoskeleton (or by cell extracts) in bulk suspensions in presence of molecular motors (e.g. myosin or kinesin) [7, 8]. In these solutions molecular motors exert forces on cytoskeletal filaments (actin filaments and microtubules) [9] and trigger their motion in the surrounding fluid. These forces, exchanged through transient and motile contact points between filaments and motor proteins, result from the conversion of chemical energy, typically coming from ATP hydrolysis, into mechanical work. Such systems are commonly termed "active".

Active systems show many interesting physical properties, of general character, related to their collective behavior, remarkable especially when compared with their analogue in passive or equilibrium systems. Pattern formation is an example. A disordered array of microtubules may arrange into spiral or aster configurations when the concentration of motor proteins (for instance kinesin) is sufficiently high [7]. Suspensions of bacteria, in spite of their low Reynolds numbers, can exhibit turbulent flow patterns [10, 11], marked by traveling *jets* of high collective velocities and surrounding *vortices*. Active fluids also exhibit peculiar rheological properties. Depending on the characteristic of the active stress (contractile or extensile, see in the following), activity is either capable to heighten viscosity, enough to develop shear-thickening properties in contractile systems [12–16], or to induce a "superfluid" regime under suitable conditions in extensile suspensions. [17]. Other relevant properties have emerged in the study of fluctuation statistics [18–23], while non-equilibrium order-disorder transitions have been studied in several models [24]. Fluctuations and phase transitions have been especially analyzed in the context of agent-based models. The flocking transition [25], for instance, was the first one to be studied in a model of point-like particles moving at fixed speed and with aligning interaction [26]. Activity by alone actually favors aggregation and can induce a phase transition, often called motility induced phase transition (MIPS) [27]. This has been numerically studied by using simple particle-based models of active colloids with excluded volume interactions and different shapes [28–35]. The particle approach has been also largely used in other contexts, to simulate, for example, the self-organization of cytoskeleton filaments described as semiflexible filaments [36].

Different approaches aiming at a coarse-grained description based on general symmetry arguments and conservation laws have been developed for capturing essential or *universal* large scale behavior of active systems and for studying their material properties. The first continuum description in terms of density and polarization field, with interactions favoring alignment with polar order, was proposed in [37]. In this model, as in others where nematic interactions were considered [38–40], the medium in which particles are supposed to move does not contribute with its own dynamics to the evolution of the system. Hence the environment of the active system can be considered as a momentum-absorbing substrate and momentum is not conserved. On the other hand, there are systems in which the dynamics of the solvent can be relevant in a certain interval of length scales [41] and must be incorporated in the description. This was first done in [18], and developed for active filaments or orientable particles in [42, 43]. Here the action of the active components on the solvent is taken into account by introducing an active stress into a generalized form of the Navier-Stokes equation. The total stress will also include elastic contributions, depending on the polar or nematic character of the system, stemming from an appropriate free-energy expression, as in the passive or equilibrium counterpart of the systems in exam. A complete dynamical description of this complex fluid, usually called active gel, often includes convection-relaxation

⋆ *Present address:* Insert the address here if needed

equations governing the physics of suitable order parameters describing, for instance, the orientation of the active material (nematic or polar) or its concentration. To solve the dynamics described by these non-linear coupled partial differential equations, numerical methods are required. A suitable approach, largely used to study multicomponents and complex fluids whose dynamics obey such equations [44–49], is the Lattice Boltzmann Method (LBM) [50], a computational fluid dynamics scheme which solves the Navier-Stokes equation. Among its features, this method is found to correctly capture the coupling between hydrodynamics and orientational order of liquid crystals (often known as backflow [51–53]), a crucial requirement to simulate the dynamics of active gels [13, 54].

In this article we will review the way LBM can be used to describe collective properties of active fluids, describing also recent developments concerning few issues where hydrodynamics plays a relevant role.

We will initially review the thermodynamics of active fluids whose internal constituents are orientable objects, such as active liquid crystals. After shortly introducing the order parameters and the free-energy usually adopted to describe their properties, we will show how the active behavior enters the model and how hydrodynamic equations can be written to correctly capture the physics. This will be done in Section 2.

Afterwards we will discuss different LBM strategies used to study simple and structured fluids. For a simple fluid, LBM solves a minimal Boltzmann kinetic equation governing the evolution of a single set of variables (the distribution functions), in terms of which hydrodynamic quantities can be written [55, 56]. A detailed description of the LB methods for a single fluid can be found in [50, 57, 58]. For structured fluids, a full LBM approach can be followed by introducing a further set of distribution functions for the order parameter that follow the dynamics of appropriate lattice Boltzmann equations that add to those describing the dynamics of the density and velocity of the fluid [44]. Then, interactions can be implemented by specific collision rules introduced on a phenomenologically ground or by making reference to a specific free-energy model that sets the thermodynamics of the system [44, 59, 60]. The first approach, in numerous variants, has been largely used in the context of binary mixtures, due to its practical convenience, with the collision step designed in order to favor separation of the A and B components of the mixture [61]. When the fluid structure becomes more complex the second approach becomes almost mandatory. The characteristics of a specific system will enter the lattice dynamic equations through a chemical potential and a pressure tensor that can be obtained by a given free-energy functional. Liquid crystals [49], but also ternary mixtures with surfactant [46] or other kinds of complex fluids [62], have been largely studied in this way. Finite difference methods, with possible numerical advantages, can be also applied to simulate the order parameter dynamical equations [48] and have been implemented in hybrid approaches coupled to LBM used as a solver for Navier-Stokes equations. These different options with details on possible algorithms and numerical implementation will be reviewed in Sect. 3.

The following sections will be dedicated to discuss some relevant topics in active fluids in which LBM has played an essential role. In Section 4 the main numerical results concerning the hydrodynamic instabilities generated by spontaneous flows [63, 64] will be reviewed. Understading how this occurs is fundamental, for instance, to assess the dynamics of topological defects as well as the physics of self-propelled droplets, objetcs which can capture some relevant features of motile cells [65, 66]. Section 5 will be devoted to review the most important results about such system. A field of research still in its infancy concerns the study of the rheological response of an active fluid to an external perturbation, such as a shear flow. In Section 6 we will review the most recent and pioneering achievements in this promising field, in which, for example, an active gel has been predicted to have either a solid-like or super-fluid-like behavior depending on the nature of the hydrodynamic instability [67]. As a further topic we will illustrate the results obtained via LBM simuations to investigate "active" turbulence [10, 68–70], a turbulent-like behavior observed in active fluids at low Reynolds numbers.

The versatility of LBM as a solver for hydrodynamics has been also used to study the flow generated by different kinds of swimmers, treated as discrete particles coupled to the surrounding fluid by proper boundary conditions [71]. In this case the solvent is described as a simple fluid whose dynamics can be solved by LBM. Although the study of the collective properties of these systems can be difficult within this approach due to the complicated structure of the flows induced by the swimmers, in a few cases this shortcoming has been overcame by using a mixed particle-continuum description . Section 7 will be briefly dedicated to describe how LBM has been extended to include active particles.

Mixtures of active and passive components are a new subject of research with new fascinating perspectives. These systems can be potentially realized by dispersing sticky bacteria [72] or self attractive cytoskeleton gels [73, 74] in water, or encapsulating an active nematic gel within a water-in-oil emulsion [73, 74]. In these systems the behavior due to active properties can be controlled not only by the strength of activity but also by fixing the amount of active fluid in the system. LBM have been largely applied to study fluid mixtures of several types and can be generalized to the case where one of the component is active. In the last section we will describe the most recent results obtained in this context.

2 Active fluid models

In this section we will focus on fluids whose internal units have an orientable character, a feature that crucially affects their reciprocal interactions, especially when a high density sample of active units is considered. In such cases the emerging orientational order on a macroscopic scale can be captured by proper order parameters, such as the

polarization vector $\boldsymbol{P}(\boldsymbol{r},t)$ and the tensor $\underline{\underline{\boldsymbol{Q}}}(\boldsymbol{r},t)$, often used to describe ordering in liquid crystals. These quantities will be introduced in 2.1.

The thermodyamics of these systems is usually described via a Landau-like free energy functional, depending upon powers of the order parameter and its gradients respecting the symmetries of the disordered phase. The different free-energy terms describing bulk and elastic properties of the active fluid will be discussed in 2.2, while 2.3 will be dedicated to describe how active terms are introduced in continuum models. In 2.4 we briefly discuss the thermodynamics of a fluid mixture with an active component, with and without alignment interaction. The latter case has been recently considered for the study motility induced phase separation in wet matter [75].

Finally the hydrodynamic equations describing both the evolution of the order parameter and of the velocity field will be shown in 2.5.

2.1 Order parameters

Active fluids whose internal constituents have an anisotropic shape (such as an elongated structure) encompass diverse systems ranging from bacterial colonies and algae suspensions [3] to the cytoskeleton of eukatyotic cells [76]. Depending upon the symmetries of such microscopic agents and upon their reciprocal interactions, these active fluids generally fall into two wide categories. The first one is the active *polar* fluid composed of elongated self-propelled particles, characterized by a head and a tail, whose interactions have polar symmetry. Such systems may order either in polar states, when all the particles are on average aligned along the same direction, or in states with nematic symmetry, when interactions favour alignment regardless of the particle's polarity. Examples range from actin filamens subject to polymerization and cross-linked with myosin [65,76–78] to bacteria self-propelled along the direction of their head [10] to microtubule filaments coupled with kinesin motors [7,73,79]. Fig. 1 shows, for example, the aggregated phase of a system of self-propelled Brownian polar dumbbells which, depending on the strength of the self-propulsion force, may arrange in a polar state (right) or in an isotropic state (left). **Figura Isabella DA Riconsiderare.** The second class includes head-tail symmetric, or *apolar*, particles that may move back and fort with no net motion, and order in nematic states. Examples of realizations in nature include *melanocytes* [80], i.e. melanin producing cells in human body, and *fibroblasts* [81], cells playing a central role in wound healing, both spindle-shaped with no head-tail distinction.

The continuum fields describing polar and nematic order are the vector field $\boldsymbol{P}(\boldsymbol{r},t)$ and the tensor field $Q_{\alpha\beta}(\boldsymbol{r},t)$ respectively (Greek subscripts denote the Cartesian components). They emerge either from a coarse grained description of a microscopical model [83] or from a theory based on general symmetry arguments [52,53]. Following, for instance, the former approach, for a system of rodlike particles the polarization field can be defined as

$$\boldsymbol{P}(\boldsymbol{r},t) = \langle \boldsymbol{\nu}(\boldsymbol{r},t)\rangle = \int \mathrm{d}\Omega f_P(\boldsymbol{\nu},\boldsymbol{r},t)\boldsymbol{\nu}, \tag{1}$$

where $f_P(\boldsymbol{\nu},\boldsymbol{r},t)$ is the probability density, encoding all the information coming from the microscopical model, of finding a particle at position $\boldsymbol{r}$ at time t oriented along the direction $\boldsymbol{\nu}$, and the integration is carried out over the solid angle Ω. The polarization can be also written as

$$\boldsymbol{P}(\boldsymbol{r},t) = P(\boldsymbol{r},t)\boldsymbol{n}(\boldsymbol{r},t), \tag{2}$$

where $\boldsymbol{n}(\boldsymbol{r},t)$ is a unit vector defining the local mean orientation of particles in the neighborhood of $\boldsymbol{r}$, and $P(\boldsymbol{r},t)$ is a measure of the local degree of alignment, ranging from 0 (in an isotropic state) to 1 (in a perfectly polarized state).

Differently, the nematic phase cannot be described by a vector field as, due to the head-tail symmetry of their constituents, both orientations $\boldsymbol{\nu}$ and $-\boldsymbol{\nu}$ equally contribute to the same ordered state. For a system of rodlike particles, the order is described by a nematic tensor which, in the uniaxial approximation (i.e. when a liquid crystal is rotationally symmetric around a single preferred axis), can be defined as

$$Q_{\alpha\beta}(\boldsymbol{r},t) = \langle \nu_\alpha\nu_\beta - \frac{1}{d}\delta_{\alpha\beta}\rangle = \int \mathrm{d}\Omega f_Q(\boldsymbol{\nu},\boldsymbol{r},t)(\nu_\alpha\nu_\beta - \frac{1}{d}\delta_{\alpha\beta}). \tag{3}$$

Again $f_Q(\boldsymbol{\nu},\boldsymbol{r},t)$ is the probability density to find a nematic particle oriented along $\boldsymbol{\nu}$ at position $\boldsymbol{r}$ and time t, while d is the dimensionality of the system. As for the polarization field, the nematic tensor can be also written in terms of the versor $\boldsymbol{n}$ (usually called *director* field) defining the local mean orientation of the particles

$$Q_{\alpha\beta}(\boldsymbol{r},t) = S(\boldsymbol{r},t)\left[n_\alpha(\boldsymbol{r},t)n_\beta(\boldsymbol{r},t) - \frac{1}{d}\delta_{\alpha\beta}\right]^{1}. \tag{4}$$

Note that, by defining the nematic tensor in this way, one can separate local anisotropic features out of isotropic ones. Indeed, the only scalar quantity that can be derived from a tensorial object, i.e. its trace, is identically null. In Eq. (4) $S(\boldsymbol{r},t)$ plays the same role of $P(\boldsymbol{r},t)$ in defining the degree of alignment of the molecules in the nematic phase. In fact, by multiplying Eq. (3) by $n_\alpha n_\beta$ and then summing over spatial components, one gets (in three dimensions)

$$S(\boldsymbol{r},t) = \frac{1}{2}\langle 3\cos^2\theta - 1\rangle, \tag{5}$$

where θ is the angle between the local preferential direction and the orientation of the particle. The scalar order parameter S achieves its maximum in the perfectly aligned state, where $\langle\cos^2\theta\rangle = 1$, while it falls to zero in the isotropic phase where the probability density f_Q is uniform over the solid angle and $\langle\cos^2\theta\rangle = 1/3$. Assuming $\boldsymbol{n}$ to be parallel to a cartesian axis, one can soon verify from Eq. (4) that $Q_{\alpha\beta}$ has two degenerate eigenvalues $\lambda_2 = \lambda_3 = -S/3$ (whose associated eigenvectors lie in

[1] See Appendix A for its extension to biaxial nematics.

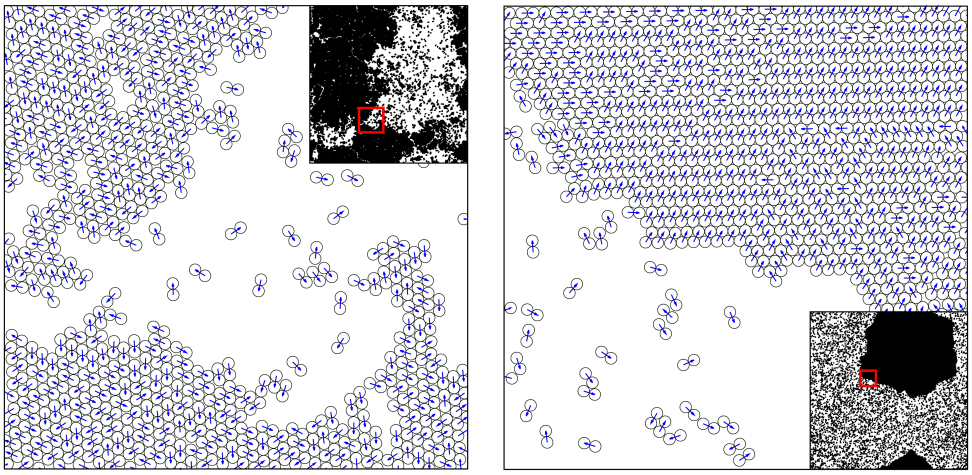

Fig. 1. System of self-propelled Brownian dumbbells for different values of the self-propulsion force corresponding to the Péclet number $Pe = 10$ and $Pe = 40$ respectively in the left and right panels. For the definition of the model and the meaning of parameters see [82]. Dumbbells have a tail and a head; the blue vectors represent the directions of self-propulsion of each dumbbell, related to the tail-head axis. Snapshots represent small portions of larger systems with total covered fraction area $\phi = 0.5$, corresponding in both cases to points in the phase diagram where phase separation between a dilute and a more dense aggregated phase is observed. Note that for small Péclet number (left panel) polar order is not present in the aggregated phase that only shows hexatic order, while for higher Péclet (right panel) the hexatic phase is globally polarised.

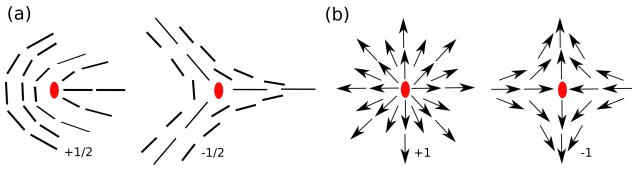

Fig. 2. Sketch of (a) half-integer topological defects in 2D nematic liquid crystals, and (b) integer topological defects in polar liquid crystals. These can only host defects with integer topological charge.

the plane normal to the particle axes) and a third non-degenerate one $\lambda_1 = 2S/3$, greater in module than λ_2 and λ_3 and related to the director itself. Such formalism can be also extended to threat the case of biaxial nematics, i.e. liquid crystals with three distinct optical axis. Unlike an uniaxial liquid crystal which has an axis of rotational symmetry (such as the director $\mathbf{n}$), a biaxial liquid crystal has no axis of complete rotational symmetry. As such theory is out of the scope of this review, we briefly mention it in Appendix A, focussing, in particular, on how biaxiality is included in the tensor order paramater and on the role it plays in the localization of topological defects.

2.1.1 Topological defects

Topological defects (often termed *disclinations* in liquid crystals) are regions where the order parameter cannot be defined [83,84]. A crucial difference between polar and nematic systems really lies on the nature of the topological defects allowed. As they play a relavant role in the dynamics of the velocity field in active fluids (as we shall see later), we provide here a brief introduction about the theory of topological defects and remind the reader to more specialized books (such as [84]) for further details.

A topolgical defect can be characterized by looking at the configuration of the order parameter far from its core. This can be done by computing the *winding* number, which is a measure of the strength of the topological defect and is defined as the number of times that the order parameter turns of an angle of 2π while moving along a close contour surrounding the defect core. Hence possible values of defect strengths critically depend upon the nature of the order parameter: indeed polar systems only admit topological defects with integer winding numbers (Fig. 2b), while nematic systems offer a wider scenario; in fact by virtue of the restored head-tail symmetry, the headless nematic director can give rise to disclination patterns that also allows for half-integer winding numbers (Fig. 2a). Fig. 3 shows, for example, two defects of charge ± 1 in an active contractile polar system: their mutual attracting interaction couples to the hyrodynamics generating a backflow [85,86] that moves the two defects closer and leads to their annihilation. On the contrary, if the system is extensile, backflow drives defects of opposite topological charge apart and suppresses pair annihilation [73, 86]. In simulations the correct position of a topological defect can be tracked either by looking at the polarization (or director for nematics) field profile or, only for nematics, by locating the regions where the scalar order parameter of the tensor field drops down. In the latter case, a further method, based on computing the degree of biaxiality around the defect core

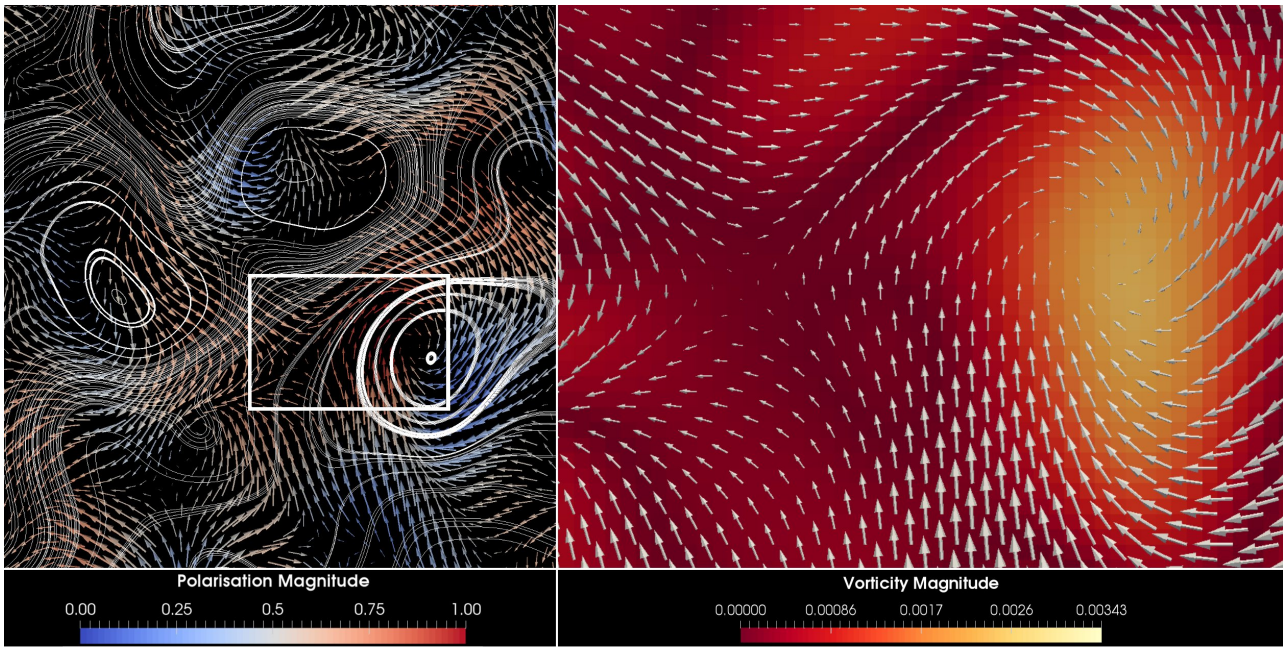

Fig. 3. Defect dynamics in active polar systems. The left panel shows the superposition of velocity streamlines to the polarization field, represented by arrows; red/long arrows correspond to ordered regions, while blue/short arrows are associated with the presence of topological defects, surrounded by regions with strong deformations of the polarization. Note that defects act as a source of vorticity: indeed most of the closed streamlines wrap the core of a defect. This is also shown in the right panel, showing the polarisation field superimposed to vorticity contour plot in the region highlighted by the white box in the left panel. Here two defects of charge ± 1 are interacting. In proximity of the defect cores the polarization magnitude is approximately null, as order is locally lost. These simulations have been performed using a LBM method for the model descirbed by the free energy in Eq. (9), considering only the polarization contributions.

is briefly discussed in Appendix A. In fact regions close to the defect core display biaxiality [87].

Note that, although defects appearing in the active fluid of Fig. 3 are points, other structures are possible. Defects are said to be topologically stable if a non uniform configuration of the order parameter cannot be reduced to a uniform state by a continuous transformation. A general criterion to establish whether a defect is topologically stable or not, is to look at the dimension n of the order parameter. In a d-dimensional space, the condition that all the n components of the order parameter must vanish at the defect core defines a "surface" of dimension $d-n$. Hence defects exist if $n \leq d$. In Fig. 3, for example, we have a two-dimensional system ($d=2$) and an order parameter (the polarization $\boldsymbol{P}$) with two components ($n=2$), and the defects allowed are points (or vortices). However point defects can be unstable in quasi-2d systems, i.e. when the order parameter fully lives in the three-dimensional space, as in such case one would have $n > d$: indeed the vector field in proximity of a vortex is always capable of escape out of the plane aligning with itself, thus removing the defect. In three-dimensional systems ($d=3$) one may have either point defects (if $n=3$) or lines (if $n=2$).

2.2 Free energy

In this section we will shortly review the free-energy expressions generally used to describe polar and nematic suspensions and often employed for active fluids, built from the order parameters discussed in the previous section.

Bulk properties and order-disorder phase transitions can be derived by a free energy functional with terms respecting the symmetries of the disordered phase, in the spirit of Landau approach. Free-energy F will only contain scalar terms invariant under space rotations, proportional to the order parameters and their powers. For a vector order-parameter scalar objects of the form $\boldsymbol{P}^{2m}$ can be considered, with m positive integer, usually arresting the expansion to the fourth order. For the nematic order parameter scalar quantities are objects of the form $\mathrm{Tr}(Q^m)$; note that there is no impediment here to odd power terms, by virtue of the invariance of $Q_{\alpha\beta}$ under inversions, but no linear term will appear in the expansion since $\mathrm{Tr}\, Q$ is identically null by definition. The presence of a third order term will lead to a first order nematic-isotropic transition through the establishment of metastable regions in the phase diagram [84]. Table 1 summarizes the bulk contributions to free energy for both polar and nematic systems; note that the uniaxial free energy can be derived from the biaxial case by writing the $\underline{\underline{\boldsymbol{Q}}}$ tensor through Eq. (4).

Table 1. The table summarizes bulk and elastic contributions to free energy for polar and nematic, both uniaxial and biaxial (see Appendix A), systems. Splay, twist and bending contributions have been written explicitly in terms of different elastic constants k_i $(i = 1, 2, 3)$ for both polar and uniaxial nematic gels, while in the most general case of a biaxial nematic we did not distinguish between different contributions. The last line in the Table shows how the elastic contribution looks like assuming that the medium is elastically isotropic, *i.e.*, $k_1 = k_2 = k_3$.

Free energy contributions		Polar Gel	Nematic Gel	
			Uniaxial	Biaxial
Bulk		$a\boldsymbol{P}^2 + b\boldsymbol{P}^4$	$rS^2 - wS^3 + uS^4$	$\tilde{r}Q_{ij}Q_{ji} - \tilde{w}Q_{ij}Q_{jk}Q_{ki} + \tilde{u}(Q_{ij}Q_{ji})^2$
Elastic	Splay	$\frac{k_1}{2}(\nabla \cdot \boldsymbol{P})^2$	$\frac{k_1}{2}(\nabla \cdot \boldsymbol{n})^2$	$\frac{L_1}{2}(\partial_k Q_{ij})^2 + \frac{L_2}{2}(\partial_j Q_{ij})^2 + \frac{L_3}{2}Q_{ij}(\partial_j Q_{ij})(\partial_j Q_{ij})$
	Twist	$\frac{k_2}{2}(\boldsymbol{P} \cdot \nabla \times \boldsymbol{P})^2$	$\frac{k_2}{2}(\boldsymbol{n} \cdot \nabla \times \boldsymbol{n})^2$	
	Bend	$\frac{k_3}{2}(\boldsymbol{P} \times \nabla \times \boldsymbol{P})^2$	$\frac{k_3}{2}(\boldsymbol{n} \times \nabla \times \boldsymbol{n})^2$	
Single constant approximation		$k(\nabla \boldsymbol{P})^2$	$k(\nabla \boldsymbol{n})^2$	$L_1(\partial_k Q_{ij})^2$

In order to take into account the energetic cost due to continuous deformations of the order parameters, elastic terms are also introduced in the free energy functional. In both polar and nematic systems three different kinds of deformations can be identified: splay, twist and bending, gauged to the theory through (in general) different elastic constants k_1, k_2, k_3. While splay fosters the formation of fan-out patterns of the director and polarization field, bending favors rounded circular patterns. Instabilities associated to such deformations underlie the establishment of defects of different strength. Twist is forbidden in pure bidimensional systems, since this kind of deformation implies the director to coil around an axis, normal to the director itself. Table 1 also provides a picture of the energetic cost due to different kinds of deformations in terms of $\boldsymbol{P}$ and $\boldsymbol{n}$, respectively for polar systems and uniaxial nematics, under the assumption of uniform ordering ($S = cost$). The most general case is provided by the elastic contributions in biaxial nematics and still applies to the uniaxial case with $S = S(\boldsymbol{r})$. In order to exploit which terms are related to which deformations, one should expand the $\underline{\underline{Q}}$ tensor into the elastic biaxial free energy in terms of the director through Eq. (4); doing so and grouping splay, twist and bend contributions one finds after some algebric effort that

$$L_1 = \frac{k_3 + 2k_2 - k_1}{9S^2},$$

$$L_2 = \frac{4(k_1 - k_2)}{9S^2},$$

$$L_3 = \frac{2(k_3 - k_1)}{9S^3}.$$

In many practical situations it is convenient to adopt the single constant approximation, consisting in setting all elastic constants equal to the same value, leading to a much simpler form for the elastic free energy [84].

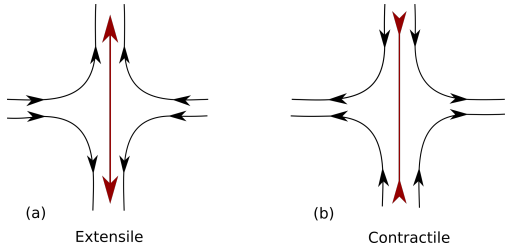

Fig. 4. Cartoon of **(a)** extensile and **(b)** contractile flow (black lines), and force dipoles (red arrows).

2.3 Active Forces

Sofar we reviewed well-known theoretical description for liquid crystals and fluids with anisotropic order parameter. We will see now how the active behavior of the constituents of the fluid can be expressed into the theoretical framework. The most direct way to develop the equations of motion for active systems at continuum level is by explicitly coarse-graining more detailed particle-based models [3, 39]. Hence, before starting the theoretical description, we spend few words in describing the swimming mechanism of some microorganism.

In general, the propulsive motion of active agents dispersed in a fluid creates a circulating flow pattern around each swimmer. The specific swimming mechanism of bacteria, for example, causes fluid to be expelled both forwards and backwards along the fore-aft axis, and drawn inwards radially towards this axis, creating an *extensile* flow pattern (Fig. 4). In some cytoskeleton extracts (such as the actomyosin protein complex), motor proteins can pull the filaments together, causing them to contract lengthwise and giving rise to a *contractile* flow opposite to that of the previous example (Fig. 4)[2]. Typically, activity creates a flow pattern that can be complicated in the near field, but whose far field is generically equivalent, at the

[2] A more detailed description of the hydrodynamics of swimmers is given in [2, 3, 88].

lowest order, to the action of a force dipole [89] and can be represented as such. By summing the contributions from each force dipole and coarse-graining [18], it is possible to show that the stress exerted by the active particles on the fluid has the form

$$\sigma_{\alpha\beta}^{\rm active} = -\zeta\phi Q_{\alpha\beta}, \tag{6}$$

where ζ is a phenomenological parameter that measures the activity strength, being negative for contractile systems and positive for extensile ones, while ϕ represents the concentration of the active material. Usually only terms linearly proportional to ζ are considered. In the case of polar active liquid crystals, the description can be carried out considering only the polarization field, re-expressing $\mathbf{Q}$ as a function of $\mathbf{P}$. The active stress in terms of the dynamical variable $\mathbf{P}(\boldsymbol{r},t)$ takes the form

$$\sigma_{\alpha\beta}^{\rm active} = -\zeta\phi\left(P_\alpha P_\beta - \frac{1}{d}|\mathbf{P}|^2\delta_{\alpha\beta}\right) \quad . \tag{7}$$

The expressions Eq. (6) and Eq. (7), as we will see later, have been largely applied in the study of active fluids.

Many biological systems also display a local chirality [90, 91]. Actin filaments, for example, are twisted in a right-ended direction [92] so that myosin motors tends also to rotate them while pulling, creating a torque dipole. A concentrated solution of DNA has long been known to exhibit a cholesteric or blue-phase in different salt conditions [93, 94]. Such system may be rendered motile if interacting with DNA or RNA polymerases or with a motor protein. The effect of torque dipoles can be incorporated in the description adding to the active stress a term of the form $\zeta_2\epsilon_{\alpha\beta\mu}\partial_\nu\phi(P_\mu P_\nu)$ [95], whose divergence is the force density associated with an ensemble of microscopic torque dipoles. The sign of the second activity parameter ζ_2 determines whether the system is right ($\zeta_2 > 0$) or left ($\zeta_2 < 0$) handed. These terms drive the system out of equilibrium by injecting energy into it, and, as those of Eq. (6) and Eq. (7), cannot be derived from a free energy functional. In this approach the active stress tesnor enters in the hydrodynamic equations governing the motion of the self-propelled particles suspension. These are constructed from general principles, by assuming that an active gel is described by (a) "conserved" variables, which are the fluctuations of the local concentration of suspended particles and the total (solute plus solvent) momentum density, and (b) "broken-symmetry" variables, which, in the nematic phase, is the deviation of the director field from the ground state.

A more general way to construct the equations of motion at a coarse-grained level, is to generalize forces-and-fluxes approach [96] to active systems [42]. Considering for example an active gel characterized by polarization $\mathbf{P}$ and velocity $\mathbf{v}$, or equivalently by the strain rate tensor $u_{\alpha\beta} = (\partial_\alpha v_\beta + \partial_\beta v_\alpha)/2$, the generalized hydrodynamic equations are derived using Onsager relations, thus expanding fluxes $\partial_t\mathbf{P}$ and the stress tensor in terms of their conjugate forces $-\delta F/\delta\mathbf{P}$ and $u_{\alpha\beta}$ respectively, with F polarization free energy. Active dynamics is obtained holding the system out of equilibrium by introducing a further pair of conjucate forces, namely the chemical potential difference between ATP and hydrolysis products and the rate of ATP consumption [42]. This approach can be further generilized [97]including thermal fluctuations, recasting the forces-and-fluxes approach in the language of coupled generalized Langevin equations [98].

Finally, we mention a more phenomenological model used to show self organization and scale-selection for the flow pattern in active matter. This approach is inspired by the use of the Brazowskii model [99, 100] for describing system with periodic order parameter and by related dynamical approaches in studies regarding the role of hydrodynamic fluctuations [101] in the onset of convection instability in Raylegh-Benard problem [102]. Higher order derivatives of the velocity gradients are considered in the stress tensor in addition to the usual dissipative terms:

$$\underline{\underline{\sigma}} = \left(\Gamma_2\nabla^2 + \Gamma_4\nabla^4\right)\left[\nabla\mathbf{v} + (\nabla\mathbf{v})^T\right]. \tag{8}$$

If Γ_2 is chosen to be negative, this corresponds to the injection of energy in a definite range of wavelengths, while $\Gamma_4 > 0$ corresponds to hyperviscosity flow damping. This is obtained by truncating a long-wavelength expansion of the stress tensor [103]. The resulting generalized Navier-Stokes equations have been proven to capture experimentally observed bulk vortex dynamics of bacterial suspensions and some rheological properties of active matter [11, 68, 104].

2.4 Fluid mixtures with an active component

The active stress expressions of Eqs. (6) and (7) depend on the concentration of the active material. This quantity in turn can be a dynamical field if one would like to take into account a inhomogeneous presence of the active material in the solution. Different kinds of models for the description of mixtures of self propelled and passive particles have been considered. For example, Brownian-like simulations [105–107] focused on the role of activity in separating the two components of the mixtures. In a continuum description, binary fluids with an active component have been considered in [65, 77, 78, 108] showing that the active part may cause instabilities on active passive interface. Here we only introduce, as an example among the different models that can be used to describe fluid mixtures with an active component, the free-energy for a binary mixture where the active component is a polar gel [77]. It is given by

$$F\left[\phi,\mathbf{P}\right] = \int d\mathbf{r}\,\{\frac{a}{4\phi_{cr}^4}\phi^2(\phi-\phi_0)^2 + \frac{k}{2}\left|\nabla\phi\right|^2 \tag{9}$$
$$-\frac{\alpha}{2}\frac{(\phi-\phi_{cr})}{\phi_{cr}}\left|\mathbf{P}\right|^2 + \frac{\alpha}{4}\left|\mathbf{P}\right|^4 + \frac{\kappa}{2}(\nabla\mathbf{P})^2 + \beta\mathbf{P}\cdot\nabla\phi\} \quad .$$

The first term, multiplied by the phenomenological constant $a > 0$, describes the bulk properties of the fluid; it is chosen in order to create two free energy minima, one ($\phi = 0$) corresponding to the passive material and the

other one ($\phi = 2$) corresponding to the active phase. The second one determines the interfacial tension between the passive and active phase, with k positive constant. The third and the fourth terms control the bulk properties of the polar liquid crystal. Here α is a positive constant and $\phi_{\rm cr} = \phi_0/2$ is the critical concentration for the transition from isotropic ($|P| = 0$) to polar ($|P| > 0$) states. The choice of $\phi_{\rm cr}$ is made to break the symmetry between the two phases and to confine the polarization field in the active phase $\phi > \phi_{\rm cr}$. The term proportional to $(\nabla P)^2$ describes the energetic cost due to elastic deformation in the liquid crystalline phase (see Table 1) in the single elastic constant approximation. Finally, the last term is a dynamic anchorage energy and takes into account the orientation of the polarization at the interface between the two phases. If $\beta \neq 0$, $\mathbf{P}$ preferentially points perpendicularly to the interface (normal anchoring): towards the passive (active) phase if $\beta > 0$ ($\beta < 0$).

Such model can be also extended to study active nematic gels, by using the nematic tensor in place of the polarization field [86,108,109]. In this case the coefficients of the expansion of $Tr(Q^n)$ in bulk free energy (see Table 1) would depend on the scalar field ϕ and the elasticity, again written in the single elastic constant approximation, would include a term of the form $L\partial_\alpha\phi Q_{\alpha\beta}\partial_\beta\phi$ (with L constant) to guarantee a perpendicular anchoring of the liquid crystal at the interface.

We finally mention a recent generalization of such models where emulsification of the active component is favored by the presence of surfactant added to the mixture [110]. This is done by allowing negative values of the binary fluid elastic constant k and by including a term of the form $\frac{c}{2}(\nabla^2\phi)^2$ (with c positive constant) to guarantee the stability of the free-energy. Results show, for example, that when the active component is contractile, a high enough activity favors the creation of passive droplets within an active matrix, while, for extensile activity, an emulsion of spontaneous rotating droplets in a passive fluid is found.

A different continuum model, specifically introduced to study the motility induced phase separation (MIPS) without direct appeal to orientational order parameters $\mathbf{P}$ or $\mathbf{Q}$, but only to the scalar concentration field ϕ, is the so called Active-model H [75]. In the old classification by Hohenberg and Halperin [111], the passive model H considers a diffusing, conserved, phase separating order parameter ϕ coupled to an isothermal and incompressible fluid flow through the advection-diffusion equation that will be introduced Sec. 2.5. The chemical potential that enters the dynamic equation of the passive model H is given by

$$\mu = \frac{\delta F}{\delta \phi} = a\phi + b\phi^3 - k\nabla^2\phi \ , \tag{10}$$

with a, b, k constants appearing in the Landau free energy for binary mixtures [112] (with a negative in order to have phase separation between the two fluid components and b and k positive for stability). The same terms appear in Eq. (9) without the polarization contributions. The active model is then constructed by adding a leading order time-reversal breaking active term of the form $\mu_a = \lambda\,(\nabla\phi)^2$ (with λ constant), not stemming from the free energy functional [75]. The deviatoric stress $\underline{\underline{\sigma}}$, that enters in the NS equations for the fluid flow, is, in d dimensions,

$$\sigma^a_{\alpha\beta} = -\hat{\zeta}\left(\partial_\alpha\phi\partial_\beta\phi - \frac{1}{d}\left(\nabla\phi\right)^2\delta_{\alpha\beta}\right), \tag{11}$$

and can be obtained from the free energy, according to the formula reported in the second row of Table 2, only if $\hat{\zeta} = k$. If $\hat{\zeta} \neq k$ this is not true anymore and Eq. (11) is the sole leading-order contribution to the deviatoric stress for scalar active matter. Again here, $\zeta < 0$ describes contractile systems while $\zeta > 0$ the extensile ones. While μ_a has been found to create a jump in the thermodynamic pressure across interfaces and to alter the static phase diagram [113], the active stress $\underline{\underline{\sigma}}^a$ creates a negative interfacial tension in contractile systems that arrests the coarsening [75].

2.5 Hydrodynamic equations

We can now introduce the hydrodynamic equations for active liquid crystals. Evolution equations for mass density $\rho(\boldsymbol{r},t)$ and velocity $\boldsymbol{v}(\boldsymbol{r},t)$ are given by

$$\nabla\cdot\boldsymbol{v} = 0, \tag{12}$$

$$\rho\left(\partial_t + \boldsymbol{v}\cdot\nabla\right)\boldsymbol{v} = -\nabla p + \nabla\cdot\underline{\underline{\sigma}}^{total}, \tag{13}$$

with the energy balance equation generally neglected in this context. The first one is the incompressible condition for mass density, while the second one is the incompressible Navier-Stokes equation, where p is the isotropic pressure and $\underline{\underline{\sigma}}^{total}$ is the total stress tensor [53] that can be split into the equilibrium/passive and non-equilibrium/active contributions:

$$\underline{\underline{\sigma}}^{total} = \underline{\underline{\sigma}}^{passive} + \underline{\underline{\sigma}}^{active}. \tag{14}$$

The passive part is, in turn, the sum of three terms:

$$\underline{\underline{\sigma}}^{passive} = \underline{\underline{\sigma}}^{viscous} + \underline{\underline{\sigma}}^{elastic} + \underline{\underline{\sigma}}^{interface}. \tag{15}$$

The first term is the viscous stress written as $\sigma^{viscous}_{\alpha\beta} = \eta(\partial_\alpha v_\beta + \partial_\beta v_\alpha)$ where η is the shear viscosity[3] An explicit form for the elastic and interface stress is reported for the polar and nematic case in Table 2.

[3] In the compressible case, the viscous stress tensor also includes a term proportional to the divergence of the velocity, such that:

$$\sigma^{viscous}_{\alpha\beta} = \eta(\partial_\alpha v_\beta + \partial_\beta v_\alpha) + \left(\tilde{\zeta} - \frac{2\eta}{d}\right)\partial_\gamma v_\gamma\delta_{\alpha\beta}, \tag{16}$$

where we denoted the bulk viscosity with $\tilde{\zeta}$. Notice that this term drops in the limit of an incompressible fluid by virtue of Eq. (12).

Table 2. The molecular field $\boldsymbol{\Xi}$ is a vector, whose components are denoted with h_α, for polar gels and a tensor $\mathbf{H}$ for nematic gels. κ is the elastic constant of the liquid crystal and the parameters ξ and λ depend on the geometry of the miscroscopic constituents($|\xi| > 0$, $|\xi| < 0$ and $|\xi| = 0$ for rod-like, disk-like and spherical particles, respectively). In addition these parameters establish whether the fluid is flow aligning ($|\xi| > 1$) or flow tumbling ($|\xi| < 1$) under shear; $\underline{\underline{D}} = (\underline{\underline{W}} + \underline{\underline{W}}^T)/2$ and $\underline{\underline{\Omega}} = (\underline{\underline{W}} - \underline{\underline{W}}^T)/2$ represent the symmetric and the antisymmetric parts of the velocity gradient tensor $W_{\alpha\beta} = \partial_\beta v_\alpha$.

	Polar Gel	Nematic Gel
$\sigma^{elastic}_{\alpha\beta}$	$\frac{1}{2}(P_\alpha h_\beta - P_\beta h_\alpha) - \frac{\xi}{2}(P_\alpha h_\beta + P_\beta h_\alpha) - \kappa \partial_\alpha P_\gamma \partial_\beta P_\gamma$	$2\lambda\left(Q_{\alpha\beta} - \frac{\delta_{\alpha\beta}}{3}\right) Q_{\gamma\nu} H_{\gamma\nu} - \lambda H_{\alpha\gamma}\left(Q_{\gamma\beta} + \frac{\delta_{\gamma\beta}}{3}\right)$ $-\lambda\left(Q_{\alpha\gamma} + \frac{\delta_{\alpha\gamma}}{3}\right) H_{\gamma\beta} - \partial_\alpha Q_{\gamma\nu} \frac{\delta \mathcal{F}}{\delta \partial_\gamma Q_{\nu\gamma}} + Q_{\alpha\gamma} H_{\gamma\beta} - H_{\alpha\gamma} Q_{\gamma\beta}$
$\sigma^{interface}_{\alpha\beta}$	$\left(f - \phi \frac{\delta F}{\delta \phi}\right) \delta_{\alpha\beta} - \frac{\partial f}{\partial(\partial_\beta \phi)} \partial_\alpha \phi$	$\left(f - \phi \frac{\delta F}{\delta \phi}\right) \delta_{\alpha\beta} - \frac{\partial f}{\partial(\partial_\beta \phi)} \partial_\alpha \phi$
$\boldsymbol{S}$	$-\underline{\underline{\Omega}} \cdot \mathbf{P} + \xi \underline{\underline{D}} \cdot \mathbf{P}$	$[\lambda \underline{\underline{D}} + \underline{\underline{\Omega}}]\left(\boldsymbol{Q} + \frac{\boldsymbol{I}}{3}\right) + \left(\boldsymbol{Q} + \frac{\boldsymbol{I}}{3}\right)[\lambda \underline{\underline{D}} - \underline{\underline{\Omega}}] - 2\lambda\left(\boldsymbol{Q} + \frac{\boldsymbol{I}}{3}\right)(\boldsymbol{Q}\boldsymbol{\nabla}\boldsymbol{v})$

The order parameter $\boldsymbol{\Psi}$ of the active liquid crystal (that is $\underline{\underline{\boldsymbol{Q}}}$ for nematics and $\boldsymbol{P}$ for polar systems) evolves accordingly to

$$(\partial_t + \boldsymbol{v} \cdot \nabla)\, \boldsymbol{\Psi} - \boldsymbol{S} = \Gamma \boldsymbol{\Xi}\ , \tag{17}$$

known as *Beris-Edwards equations*, within the theory liquid crystal hydrodynamics described through the Q-tensor. The term $\boldsymbol{S}$ accounts for the response of the orientational order to the extensional and rotational components of the velocity gradient and is reported for the polar [114] and nematic [83] case in the third row of Table 2. The molecular field $\boldsymbol{\Xi} = \delta F/\delta \boldsymbol{\Psi}$ governs the relaxation of the orientational order to equilibrium, and is multiplied by a collective rotational-diffusion constant Γ. The left-hand side of Eq. (17) is commonly addressed as material derivative of the order parameter $\boldsymbol{\Psi}$, and can be formally derived making use of Liouville equations. In fact one can write $D_t \boldsymbol{\Psi} = \partial_t \boldsymbol{\Psi} + \{\boldsymbol{\Psi}, \mathcal{H}\}$, where $\{...\}$ are the Poisson parethesis and the Hamiltonian is $\mathcal{H} = F + \frac{1}{2}\int \rho \boldsymbol{v}^2$.

A more phenomenological procedure to derive the material derivative explicitly is based on the fact that order parameters can be advected by the fluid. Here we outline the procedure referring only to the polarisation field. We first notice that the relative position $\tilde{\boldsymbol{r}}$ of two close points in the fluid evolves accordingly to the following equation:

$$D_t \tilde{\boldsymbol{r}} = \partial_t \tilde{\boldsymbol{r}} + (\tilde{\boldsymbol{r}} \cdot \nabla)\tilde{\boldsymbol{r}} + \underline{\underline{D}} \cdot \tilde{\boldsymbol{r}} + \underline{\underline{\Omega}} \cdot \tilde{\boldsymbol{r}}. \tag{18}$$

The first two contributions are the usual lagrangian derivative while the third and fourth ones account respectively for rigid rotations and deformations of the fluid element. Thus the material derivative for the polarisation field will include the first three terms since a vector advected by the flow is capable to follow any rigid motion; for what concerns the last term in Eq. (18) this cannot enter directly into the material derivative of a vector field, but it must be weighted through an alignment parameter ξ, ruling the dynamical behavior of the vector field under enlargement and/or tightening of flow tubes. This allows us to obtain the material derivative for the polarization field simply substituting $\boldsymbol{P}$ in place of $\tilde{\boldsymbol{r}}$.

Finally the time evolution of the concentration field $\phi(\boldsymbol{r}, t)$ of the active material is governed by a convection-diffusion equation

$$\partial_t \phi + \nabla \cdot (\phi \boldsymbol{v}) = \nabla \cdot \left(M \nabla \frac{\delta F}{\delta \phi} \right), \tag{19}$$

where M is the mobility and $\delta F/\delta\phi$ is the chemical potential. A more generalized form of the material derivative has been used to model, for example, actin polymerization in motile eukaryotic cells [65], by substituting $\nabla \cdot (\phi \boldsymbol{v}) \to \nabla \cdot (\phi \boldsymbol{v} + w \boldsymbol{P})$, where w is a constant related to the velocity of actin polymerization.

3 Lattice Boltzmann Method

A certain number of approaches are feasible when dealing with the description of fluid systems; each of them can be classified according to the level of spatial approximation. A molecular approach would hardly access the time and space scales relevant for a complete hydrodynamic description of the systems here considered. At a mesoscopic level, kinetic theory furnishes a description of irreversible and non-equilibrium thermodynamic phenomena in terms of a set of distribution functions encoding all necessary informations related to space positions and velocities of particles. Continuum equations give a description of irreversible phenomena by using macroscopic variables slowly varying in time and space. This last approach has the notnegligigle advantage that one has to deal with a few fields. On the other hand, when considering continous equations, one has to face some technical issues arising from the stability of numerical implementation and discretization schemes [115]. Moreover, many numerical methods aimed at solving the continuous equations, exhibit criticalities in the amount of computational resources, mostly in terms of processing times and memory requirement, or in the implementation of boundary conditions in complex geometries. To avoid these issues lattice-gas-automaton (LGA) models were first developed starting from the pioneering work of Frisch *et al.* [116]. This kinematic approach to

hydrodynamics is based on the description of the dynamics of a number of particles moving on a suitable lattice. Both mass and momentum conservation are imposed in collisions between particles; moreover an exclusion principle is imposed to restrict the number of particles with a given velocity at a certain lattice point to be 0 or 1. This latter feature allows for a description of the local particle equilibrium through the Fermi-Dirac statistics [117]. Despite LGA proved to be very efficient in simulating the Navier-Stokes equation from a computational point of view and in managing boundary conditions, it suffers from non-Galilean invariance, due to density dependence of the convection coefficient and from an unphysical velocity dependence of the preassure, arising directly from the discretization procedure [57].

Lattice Boltzmann methods were then developed to overcome these difficulties. Particles in the LGA method are formally substituted by a discretized set of distribution functions, so that hydrodynamic variables are indeed expressed at each lattice point in terms of such distribution functions. Despite the fact that Lattice Boltzmann is a mesoscopic numerical method, it has a number of advantages that resulted in the broad usage of this method in many branches of hydrodynamics. Firstly LB algorithms are appreciably stable and they are characterized by their simplicity in the treatment of boundary conditions. Not to be neglected is the fact that LB algorithms are particularly suitable to parallel approach.

In the following of this Section we will first provide a simple overview of the method, without getting too technical, in order to convey to the reader the purpose of this approach. In Section 3.1 we will first introduce LBM for a simple fluid, while Section 3.2 will be devoted to recover the continuum hydrodynamic equations, already presented in Section 2.5, through a Chapman-Enskog expansion. In Section 3.3 we will describe some routes to adapt LBM to the case of complex fluids through the introduction of a forcing term; in Section 3.5 we will focus on some algorithms that has been recently used in the numerical investigation of active matter. Finally, in Section 3.6 we will focus on the implementation of boundary conditions.

3.1 General features of lattice Boltzmann method

The lattice Boltzmann approach to hydrodynamics is based on a phase-space discretized form of the Boltzmann equation [50, 118–121] for the distribution function $f(\boldsymbol{r}, \boldsymbol{\xi}, t)$, describing the fraction of mass at position $\boldsymbol{r}$ moving with velocity $\boldsymbol{\xi}$ at the time t. Since the discretization is performed both in real and velocity space, the algorithm is expressed in terms of a set of discretized distribution functions $\{f_i(\boldsymbol{r}_\alpha, t)\}$, defined on each lattice site $\boldsymbol{r}_\alpha$ and related to a discrete set of N lattice speeds $\{\boldsymbol{\xi}_i\}$, labelled with an index i that varies from 1 to N (see Fig. 5). In the case of the *collide and stream* version of the algorithm, the evolution equation for the distribution functions has the form

$$f_i(\boldsymbol{r} + \boldsymbol{\xi}_i \Delta t, t + \Delta t) - f_i(\boldsymbol{r}, t) = \mathcal{C}(\{f_i\}, t), \tag{20}$$

where $\mathcal{C}(\{f_i\}, t)$ is the collisional operator that drives the system towards equilibrium and depends on the distribution functions; its explicit form will depend upon the particular implementation of the method. Eq. (20) describes how fluid particles collide in the lattice nodes and move afterwards along the lattice links in the time step Δt towards neighboring sites at distance $\Delta x = \xi_i \Delta t$. This latter relationship is no more considered in finite difference lattice Boltzmann models (FDLBM) which are directly based on the Boltzmann equation [122–126]. In these kind of models the discrete velocity set can be chosen with more freedom, making possible to use non uniform grids, selecting lattice velocities independently from the lattice configuration[4]. This results to be extremely useful when it is necessary to release the constraint of having a constant temperature in the system [127, 128]. This might be also helpful in the case of LB models for multicomponent systems where the components have different masses and this would result in having different lattice speeds, one for each fluid species. Beside the wider range of applicability of the FDLBM with respect to the LBM, the latter furnishes a simple and efficient way to solve the hydrodynamics equations; moreover we are not aware of any implementation of the FDLB algorithm developed to study active matter; for this reasons we will avoid any further discussion on this topic.

In the case of a simple fluid, in absence of any external force, assuming the BGK approximation with a single relaxation time [129], one writes

$$\mathcal{C}(\{f_i\}, t) = -\frac{1}{\tau}(f_i - f_i^{eq}), \tag{22}$$

where f_i^{eq} is the equilibrium distributions and τ is the relaxation time, connected to the viscosity of the fluid, as it will be seen. The mass and momentum density are defined as

$$\rho(\boldsymbol{r}, t) = \sum_i f_i(\boldsymbol{r}, t), \tag{23}$$

$$\rho(\boldsymbol{r}, t)\boldsymbol{v}(\boldsymbol{r}, t) = \sum_i f_i(\boldsymbol{r}, t)\boldsymbol{\xi}_i, \tag{24}$$

where summations are performed over all discretized directions at each lattice point. By assuming both mass and momentum density to be conserved in each collision, it is

[4] When dealing with FDLBM it is useful to introduce more than only one set of distribution functions $\{f_{ki}\}$, where the extra index k has been used to label each set to a group of descrete velocities $\{\boldsymbol{\xi}_{ki}\}$, while index i still denotes the streaming direction. The evolution equation for distribution functions for the FDLBM reads:

$$\partial_t f_{ki} + (\boldsymbol{\xi}_{ki} \cdot \nabla) f_{ki} = \mathcal{C}(\{f_{ki}\}, t). \tag{21}$$

Here differential operators must be discretized: Runge-Kutta or midpoint schemes can be used to compute the time derivative while there are several possibilities to compute the advective term on the left-hand side of the previous equation. For the reader interested in the details of the implementation we suggest to refer to Refs. [125, 127].

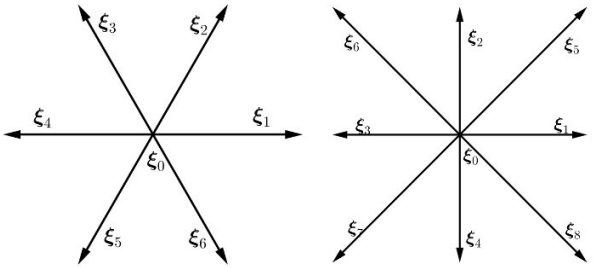

Fig. 5. Graphical representation of lattice speeds for geometries $D2Q7$ and $D2Q9$, respectively shown in the left and right panels.

found that conditions in Eq. (23), (24) must hold also for the equilibrium distribution functions:

$$\rho(\boldsymbol{r},t) = \sum_i f_i^{eq}(\boldsymbol{r},t), \tag{25}$$

$$\rho(\boldsymbol{r},t)\boldsymbol{v}(\boldsymbol{r},t) = \sum_i f_i^{eq}(\boldsymbol{r},t)\boldsymbol{\xi}_i. \tag{26}$$

Moreover, it is necessary to introduce further constraints on the second moment of the equilibrium distribution functions to recover continuum equations, as it will become more evident in the following. Further constraints on higher order moments may become necessary to simulate more complex systems: for instance full compressible flows or supersonic adaptation of the algorithm may require the specification of moments up to the third, while for a complete hydrodynamic description in which heat transfer is also taken into account, even the fourth moment needs to be specified [127]. Active matter systems such as bacterial and microtubules suspensions reasonably fulfil the incompressible condition, so that in the following we will only impose constraints up to second order moments.

Another peculiar fact about LBM is that viscosity explicitly depends upon the choice of the lattice structure, so that in order to deal with a specific form for the viscous part of the stress tensor, we are forced to fix a particular discretized lattice. Due to the fact that sufficient lattice symmetry is required to recover the correct Navier-Stokes equation in the continuum limit [116], not all the possible lattice structures can be adopted. By denoting the space dimensions by D and the number of lattice speeds by Q, Table 3 shows the velocities $\{\boldsymbol{\xi}_i\}$ and the corresponding weights in the equilibrium distribution functions (see next Section) for the most frequent choices. Here the quantity $c = \Delta x/\Delta t$, connected to the speed of sound of the algorithm, has been introduced as the ratio between the lattice spacing Δx and the time step Δt. Figure 5 illustrates explicitly the lattice structures in the two-dimensional case.

Table 3. Lattice speeds with their weights ω_i for spatial dimensions $D = 2$ and $D = 3$ and number of neighboring nodes Q.

Lattice	$\boldsymbol{\xi}_i$	ω_i
D2Q7	$(0,0)$	$1/2$
	$c(\cos(i\pi/3), \sin(i\pi/3))$	$1/12$
D2Q9	$(0,0)$	$4/9$
	$(\pm c, 0)$ $(0, \pm c)$	$1/9$
	$(\pm c, \pm c)$	$1/36$
D3Q15	$(0,0,0)$	$2/9$
	$(\pm c,0,0)$ $(0,\pm c,0)$ $(0,0,\pm c)$	$1/9$
	$(\pm c, \pm c, \pm c)$	$1/72$
D3Q19	$(0,0,0)$	$1/3$
	$(\pm c,0,0)$ $(0,\pm c,0)$ $(0,0,\pm c)$	$1/18$
	$(\pm c,\pm c,0)$ $(\pm c,\pm c,0)$ $(0,\pm c,\pm c)$	$1/36$
D3Q27	$(0,0,0)$	$8/27$
	$(\pm c,0,0)$ $(0,\pm c,0)$ $(0,0,\pm c)$	$2/27$
	$(\pm c,\pm c,0)$ $(\pm c,\pm c,0)$ $(0,\pm c,\pm c)$	$1/54$
	$(\pm c,\pm c,0)$ $(\pm c,\pm c,0)$ $(0,\pm c,\pm c)$	$1/216$

3.2 Lattice Boltzmann for a simple fluid

In this Section we will present a basic lattice Boltzmann algorithm to solve the hydrodynamic equations (12) and (13) for a simple fluid; in this case the term on the right hand side of the Navier-Stokes equation (13) reduces to the preassure gradient plus the mere viscous contribution $\partial_\beta \sigma^{viscous}_{\alpha\beta}$, under the assumption that no external force is acting on the fluid.

Conditions (25) and (26) can be satisfied by expanding the equilibrium distribution functions up to the second order in the fluid velocity v [57]:

$$f_i^{eq} = A_s + B_s v_\alpha \xi_{i\alpha} + C_s v^2 + D_s v_\alpha v_\beta \xi_{i\alpha}\xi_{i\beta}, \tag{27}$$

where the index s relates the i-th distribution function to the square module of the corresponding lattice velocity, and the greek index denotes the Cartesian component. This expansion is valid as far as the Mach number $Ma = v/c_s$ is kept small, c_s being the speed of sound, whose explicit expression in turn depends upon the lattice discretization [130]. The present assumption has the important consequence that LB models based on the previous expansion of the equilibrium distribution functions have great difficulty in simulating compressible Euler flows, that usually take place at high Mach numbers. This issue arises in standard LB approaches because of the appearence of third order nonlinear deviations from the Navier-Stokes equation [131]. Qian and Orzsag demonstrated in [132] that such nonlinear deviations grow together with Ma^2, so that they can be neglected in the low Mach number regime but become important in the compressible limit[5]. For such reasons it is necessary to ensure that velocities

[5] In order to overcome the limit posed by the low Mach number regime many variations of the standard LBM have been developed. Alexander *et al.* proposed a model where the high Mach number regime could be achieved by decreasing the speed of sound [117], discrete-velocity models [133, 134] were later introduced allowing for simulation of the compressible Euler equation in a wider range of Mach numbers. Other im-

never exceed a critical threshold that can be reasonably chosen such that $Ma \lesssim 0.3$ [132].

Besides constraints expressed by Eq. (25) and (26), an additional condition on the second moment of the equilibrium distribution functions is imposed so that

$$\sum_i f_i^{eq} \xi_{i\alpha}\xi_{i\beta} = \frac{c^2}{3}\rho\delta_{\alpha\beta} + \rho v_\alpha v_\beta. \tag{28}$$

This is a necessary condition to recover the Navier-Stokes equation in the continuum limit. By substituting the expansion (27) in the constraints (25), (26) and (28), a suitable choice for the expansion coefficients is found to be

$$A_0 = \rho - 20A_2 \quad A_1 = 4A_2 \quad A_2 = \frac{\rho}{36} \tag{29}$$

$$B_0 = 0 \quad B_1 = 4B_2 \quad B_2 = \frac{\rho}{12c^2} \tag{30}$$

$$C_0 = -\frac{2\rho}{3c^2} \quad C_1 = 4C_2 \quad C_2 = -\frac{\rho}{24c^2} \tag{31}$$

$$D_0 = 0 \quad D_1 = 4D_2 \quad D_2 = \frac{\rho}{8c^4}, \tag{32}$$

where for the sake of clarity we have explicitly chosen a $D2Q9$ lattice geometry. It is possible to show analytically [137], requiring isotropy of the fourth-order tensor of velocities and Galilean invariance, that the equilibrium distribution functions can be written in a more general way as

$$f_i^{eq} = \rho\omega_i \left[1 + 3\frac{v_\alpha\xi_{i\alpha}}{c^2} - \frac{3}{2}\frac{v^2}{c^2} + \frac{9}{2}\frac{(v_\alpha\xi_{i\alpha})^2}{c^4}\right] \tag{33}$$

where the weights ω_i are given in Table 3.

Finally, we add for completeness that it is also possible to adopt a discretization in velocity space based on the quadrature of a Hermite polynomial expansion of the Maxwell-Boltzmann distribution [130]. One then gets a lattice Boltzmann equation that allows us to exactly recover a finite number of leading order moments of the equilibrium distribution functions. In this case the quantity c is fixed and given by $c = 2$ for the geometry $D2Q7$ and by $c = \sqrt{3}$ for the other geometries in Table 3. For a detailed discussion the interested reader may refer to Ref. [130].

Chapman-Enskog expansion The remaining part of this Section will be dedicated to show that the algorithm presented here correctly reproduces continuum equations (12) and (13). Two different approaches can be followed. The first one starts from a Taylor expansion of the left-hand side of Eq. (20) [138], whereas the second one, discussed below, uses a multiscale expansion of distribution functions and derivatives in the Knudsen number $\epsilon = \lambda/L$, a dimensionless number defined as the ratio between the molecular mean free path λ and a characteristic length L of the system. This number determines whether a macroscopic continuum mechanics or a microscopic statistical mechanics formulation of fluid dynamics should be used. For small values of ϵ (for instance if $\epsilon \ll 1$) the mean free path is much smaller than L and a contiuum theory is a good approximation. In such case the Knudsen number can be treated as a parameter of a multiscale expansion in which spatial density fluctuations of order $\mathcal{O}(\epsilon^{-1})$ relax over time scales of order $\mathcal{O}(\epsilon^{-2})$. A suitable expansion for temporal and spatial derivatives as well as for distribution functions is

$$f_i = f_i^{(0)} + \epsilon f_i^{(1)} + \epsilon^2 f_i^{(2)}, \tag{34}$$

$$\partial_t = \epsilon\partial_{t_1} + \epsilon^2\partial_{t_2}, \tag{35}$$

$$\partial_\alpha = \epsilon\partial_{\alpha_1}, \tag{36}$$

built assuming that there is a diffusion time scale t_2 slower than the convection one t_1.

We start by expanding the left-hand side of eqation (20) to the second order in Δt:

$$\Delta t(\partial_t + \xi_{i\alpha}\partial_\alpha)f_i + \frac{(\Delta t)^2}{2}\left(\partial_t^2 + 2\xi_{i\alpha}\partial_\alpha\partial_t + \xi_\alpha\xi_\beta\partial_\alpha\partial_\beta\right) f_i = -\frac{1}{\tau}(f_i - f_i^{eq}), \tag{37}$$

where we use Eq. (22) to express the collision operator. By substituting Eq. (34), (35) and (36) into Eq. (37) we obtain

$$\begin{aligned}
&\Delta t\left[(\epsilon\partial_{t_1} + \epsilon^2\partial_{t_2}) + \epsilon\partial_{\alpha_1}\right](f_i^{(0)} + \epsilon f_i^{(1)} + \epsilon^2 f_i^{(2)}) \\
&+(\Delta t)^2\left[\frac{1}{2}(\epsilon\partial_{t_1} + \epsilon^2\partial_{t_2})^2 + \epsilon\xi_{i\alpha}\partial_\alpha(\epsilon\partial_{t_1} + \epsilon^2\partial_{t_2})\right. \\
&\left.+\frac{1}{2}\epsilon^2\xi_\alpha\xi_\beta\partial_{\alpha_1}\partial_{\beta_1}\right](f_i^{(0)} + \epsilon f_i^{(1)} + \epsilon^2 f_i^{(2)}) \\
&= -\frac{1}{\tau}(f_i^{(0)} + \epsilon f_i^{(1)} + \epsilon^2 f_i^{(2)} - f_i^{eq}).
\end{aligned} \tag{38}$$

By retaining only terms of order ϵ^2, the previous equation reads

$$\begin{aligned}
&\epsilon\Delta t\left(\partial_{t_1} f_i^{(0)} + \xi_{i\alpha}\partial_{\alpha_1} f_i^{(0)}\right) \\
&+\epsilon^2\left[\Delta t\left(\partial_{t_1} f_i^{(1)} + \xi_{i\alpha}\partial_{\alpha_1} f_i^{(1)} + \partial_{t_2} f_i^{(0)}\right)\right. \\
&\left.+\ \Delta t^2\left(\frac{1}{2}\partial_{t_1}^2 + \frac{1}{2}\xi_{i\alpha}\xi_{i\beta}\partial_{\alpha_1}\partial_{\beta_1} + \xi_{i\alpha}\partial_{\alpha_1}\partial_{t_1}\right) f_i^{(0)}\right] \\
&= -\frac{f_i^{(0)} - f_i^{eq}}{\tau} - \frac{\epsilon f_i^{(1)} + \epsilon^2 f_i^{(2)}}{\tau}.
\end{aligned} \tag{39}$$

Finally, grouping terms of same order in ϵ, we get

$$f_i^{(0)} = f_i^{eq} + \mathcal{O}(\epsilon), \tag{40}$$

$$\partial_{t_1} f_i^{(0)} + \xi_{i\alpha}\partial_{\alpha_1} f_i^{(0)} = -\frac{1}{\tau\Delta t} f_i^{(1)} + \mathcal{O}(\epsilon), \tag{41}$$

$$\begin{aligned}
&\partial_{t_1} f_i^{(1)} + \xi_{i\alpha}\partial_{\alpha_1} f_i^{(1)} + \partial_{t_2} f_i^{(0)} \\
&+\frac{\Delta t}{2}\left(\partial_{t_1}^2 + 2\xi_{i\alpha}\partial_{\alpha_1}\partial_{t_1} + \xi_{i\alpha}\xi_{i\beta}\partial_{\alpha_1}\partial_{\beta_1}\right) f_i^{(0)} \\
&= -\frac{1}{\tau\Delta t} f_i^{(2)} + \mathcal{O}(\epsilon).
\end{aligned} \tag{42}$$

plementations are based on a Taylor expansion of the equilibrium distributions up to higher orders together with suitable constraints on the third and fourth moments [130, 135, 136].

In the following paragraphs we will use these relations to recover continuum equations up to the second order in the Knudsen number.

Recover Continuity Equation To recover the continuity equation one can start by summing Eq. (40) over lattice velocities with the constraints given in Eq. (25) and Eq. (26). One then gets

$$\sum_i f_i^{(0)} = \rho, \qquad \sum_i f_i^{(1)} = \sum_i f_i^{(2)} = 0, \tag{43}$$

and, by using Eq. (26), we obtain

$$\sum_i f_i^{(0)} \xi_{i\alpha} = \rho v_\alpha, \qquad \sum_i f_i^{(1)} \xi_{i\alpha} = \sum_i f_i^{(2)} \xi_{i\alpha} = 0. \tag{44}$$

By performing a summation over lattice velocities in Eq. (41), one gets

$$\partial_{t_1} \rho + \partial_{\alpha_1} (\rho v_\alpha) = 0 + \mathcal{O}(\epsilon), \tag{45}$$

which is the continuity equation at first order in the Knudsen number. To recover the complete time derivative according to (35), we need to compute the term $\partial_{t_2}\rho$. By applying the differential operators $\epsilon\partial_{t_1}$ and $\epsilon\xi_{i\beta}\partial_{\beta_1}$ to Eq. (41) we get

$$\partial_{t_1}^2 f_i^{(0)} + \xi_{i\alpha}\partial_{\alpha_1}\partial_{t_1} f_i^{(0)} = -\frac{1}{\tau\Delta t}\partial_{t_1} f_i^{(1)} + \mathcal{O}(\epsilon^2), \tag{46}$$

$$\xi_{i\beta}\partial_{\beta_1}\partial_{t_1} f_i^{(0)} + \xi_{i\alpha}\xi_{i\beta}\partial_{\alpha_1}\partial_{\beta_1} f_i^{(0)} = -\frac{1}{\tau\Delta t}\xi_{i\beta}\partial_{\beta_1} f_i^{(1)} + \mathcal{O}(\epsilon^2), \tag{47}$$

and, by summing both equations, we get

$$\begin{aligned}(\partial_{t_1}^2 + 2\xi_{i\alpha}\partial_{\alpha_1}\partial_{t_1} + \xi_{i\alpha}\xi_{i\beta}\partial_{\alpha_1}\partial_{\beta_1}) f_i^{(0)} \\ = -\frac{1}{\tau\Delta t}(\partial_{t_1} + \xi_{i\beta}\partial_{\beta_1}) f_i^{(1)} + \mathcal{O}(\epsilon^2).\end{aligned} \tag{48}$$

Note that the left-hand side of this equation is exactly the term in round brackets of Eq. (42), that now becomes

$$\begin{aligned}\partial_{t_2} f_i^{(0)} + \left(1 - \frac{1}{2\tau}\right)(\partial_{t_1} - \xi_{i\alpha}\partial_{\alpha_1}) f_i^{(1)} \\ = -\frac{1}{\tau\Delta t} f_i^{(2)} + \mathcal{O}(\epsilon).\end{aligned} \tag{49}$$

By summing over lattice directions and using Eq. (43) and Eq. (44), we get

$$\partial_{t_2}\rho = 0 + \mathcal{O}(\epsilon^2), \tag{50}$$

that, together with Eq. (45), reads

$$(\epsilon\partial_{t_1} + \epsilon^2\partial_{t_2})\rho + \epsilon\partial_{\alpha_1}(\rho v_\alpha) = 0 + \mathcal{O}(\epsilon^2). \tag{51}$$

Finally, after restoring the canonical differential operators (through Eq. (35) and Eq. (36)), we get the continuity equation

$$\partial_t \rho + \partial_\alpha(\rho v_\alpha) = 0 + \mathcal{O}(\epsilon^2) \tag{52}$$

Recover Navier-Stokes Equations The procedure to recover the Navier-Stokes equation is analogous albeit less straightforward than that used for the continuity equation. We will proceed by calculating the first-order moment of Eq. (41) and Eq. (42). First multiply by $\xi_{i\beta}$ both members of Eq. (41) and sum over index i, to get

$$\partial_{t_1}(\rho v_\alpha) + \partial_{\beta_1}\left(\frac{c^2}{3}\rho\delta_{\alpha\beta} + \rho v_\alpha v_\beta\right) = 0 + \mathcal{O}(\epsilon). \tag{53}$$

To get the Navier-Stokes equation to second order in the Knudsen number we need to calculate the first-order moment of equation (42). We can then multiply Eq. (49) by $\xi_{i\gamma}$ to obtain

$$\begin{aligned}\partial_{t_2}\xi_{i\gamma} f_i^{(0)} + \left(1 - \frac{1}{2\tau}\right)(\partial_{t_1} - \xi_{i\alpha}\partial_{\alpha_1})\xi_{i\gamma} f_i^{(1)} \\ = -\frac{1}{\tau\Delta t}\xi_{i\gamma} f_i^{(2)} + \mathcal{O}(\epsilon^2),\end{aligned} \tag{54}$$

and, by summing over lattice velocities, we are left with

$$\partial_{t_2}(\rho v_\alpha) - \left(1 - \frac{1}{2\tau}\right)\partial_{\beta_1}\left[\sum_i f_i^{(1)}\xi_{i\alpha}\xi_{i\beta}\right] = 0. \tag{55}$$

Now we must determine an expression for the summation in square brackets. From Eq. (40) and (41) we note that

$$\begin{aligned}\sum_i f_i^{(1)}\xi_{i\alpha}\xi_{i\beta} = -\tau\Delta t(\partial_{t_1} + \xi_{i\gamma}\partial_{\gamma_1})\left(\sum_i f_i^{eq}\xi_{i\alpha}\xi_{i\beta}\right) \\ = -\tau\Delta t\left[\partial_{t_1}\left(\frac{c^2}{3}\rho\delta_{\alpha\beta} + \rho v_\alpha v_\beta\right) + \partial_{\gamma_1}\left(\sum_i f_i^{eq}\xi_{i\alpha}\xi_{i\beta}\xi_{i\gamma}\right)\right],\end{aligned} \tag{56}$$

where we have used Eq. (28) in the second equality. The second term of the second line of Eq. (56) can be written in terms of the equilibrium distribution functions given in (33) and of the related coefficients (30)

$$\partial_{\gamma_1}\left(\sum_i f_i^{eq}\xi_{i\alpha}\xi_{i\beta}\xi_{i\gamma}\right) = \frac{c^2}{3}\partial_{\gamma_1}\left[\rho(\delta_{\alpha\beta}v_\gamma + \delta_{\alpha\gamma}v_\beta + \delta_{\beta\gamma}v_\alpha)\right], \tag{57}$$

while the first round bracket in the second line of Eq. (56) can be written by means of Eq. (45) and Eq. (53)

$$\begin{aligned}\partial_{t_1}\left(\frac{c^2}{3}\rho\delta_{\alpha\beta} + \rho v_\alpha v_\beta\right) = -\frac{c^2}{3}\partial_{\gamma_1}(\rho v_\gamma)\delta_{\alpha\beta} \\ + v_\beta\partial_{t_1}(\rho v_\alpha) + v_\alpha\partial_{t_1}(\rho v_\beta) - v_\alpha v_\beta\partial_{t_1}\rho \\ \simeq -\frac{c^2}{3}\left[\partial_{\gamma_1}(\rho v_\gamma)\delta_{\alpha\beta} + (v_\alpha\partial_{\beta_1}\rho + v_\beta\partial_{\alpha_1}\rho)\right].\end{aligned} \tag{58}$$

In the last line terms of order v^3 were neglected, an approximation valid as far as the Mach number is kept small. Now substituting Eq. (58) and Eq. (57) into Eq. (56) we find, after some algebra, that

$$\sum_i f_i^{(1)}\xi_{i\alpha}\xi_{i\beta} = -\tau\Delta t\frac{c^2}{3}\rho\left[\partial_{\beta_1}v_\alpha + \partial_{\alpha_1}v_\beta\right]. \tag{59}$$

This term, in turn, enters Eq. (55), which now reads

$$\partial_{t_2}(\rho v_\alpha) - \left(\tau - \frac{1}{2}\right)\Delta t \frac{c^2}{3}\partial_{\beta_1}\left[\rho\left(\partial_{\beta_1} v_\alpha + \partial_{\alpha_1} v_\beta\right)\right] = 0 \tag{60}$$

Finally summing this equation with Eq. (53) and using the canonical differential operators (i.e. Eq. (35) and Eq. (36)), we obtain the Navier-Stokes equation

$$\partial_t(\rho v_\alpha) + \partial_\beta\left(\rho v_\alpha v_\beta\right) = \tag{61}$$

$$-\partial_\alpha p_i + \Delta t\left(\tau - \frac{1}{2}\right)\frac{c^2}{3}\partial_\beta\left[\rho\left(\partial_\beta v_\alpha + \partial_\alpha v_\beta\right)\right], \tag{62}$$

where $p_i = (c^2/3)\rho$ is the isotropic pressure and the shear viscosity is given by

$$\eta = \rho c_s^2 \Delta t\left(\tau - \frac{1}{2}\right). \tag{63}$$

3.3 LBM beyond simple fluids

So far we have implemented a lattice Boltzmann method for a simple fluid in the absence of any forcing term, with only viscous contributions to the stress tensor. On the other hand when dealing with more complex systems, such as multicomponents or multiphase fluids, the stress tensor may include further contributions (such as elastic and interfacial ones, see Table 2) which have a non-trivial dependence on order parameters and on their derivatives. In this Section we will show two different strategies adopted to numerically implement such terms. Briefly, while in the first they are included in a forcing term appearing in the second moment equation of the equilibrium distribution functions, in the second one they enter through an external forcing added to the collision operator in the lattice Boltzmann equation.

3.3.1 First method

To implement a general symmetric stress tensor contribution in the Lattice Boltzmann scheme previously introduced, we again impose the constraints of Eq. (25) and Eq. (26) on the zeroth and on the first moment of the equilibrium distribution functions, while the second moment (28) is modified according to the following relation

$$\sum_i f_i^{eq}\xi_{i\alpha}\xi_{i\beta} = -\sigma_{\alpha\beta} + \rho v_\alpha v_\beta. \tag{64}$$

Here $\sigma_{\alpha\beta}$ stands for the total stress tensor including isotropic contributions but deprived of viscous ones. Note that, due to the symmetry of the left hand side of Eq. (64), this algorithm can be applied to models that involve only symmetric contributions to the stress tensor. For instance, this method is suitable to study binary mixtures, as the stress tensor associated to the concentration contribution is indeed symmetric, but not for liquid crystals, as the antisymmetric part of the relative stress tensor does not vanish (see Table 2). This latter case will be discussed in the following sections. To satisfy (64) [49,54], the equilibrium distribution functions can be expanded as follows

$$\begin{aligned} f_i^{eq} = {} & A_s + B_s v_\alpha \xi_{i\alpha} + C_s v^2 \\ & + D_s v_\alpha v_\beta \xi_\alpha \xi_\beta + G_s^{\alpha\beta}\xi_{i\alpha}\xi_{i\beta}, \end{aligned} \tag{65}$$

where an extra term term, quadratic in lattice velocities, has been added to include a general stress tensor in the model. As for a simple fluid, the coefficients of the expansion can be calculated by imposing constraints of Eq. (25), Eq. (26) and Eq. (64). For a $D2Q9$ geometry a suitable choice is given by

$$\begin{aligned} A_0 = \rho - 20A_2 \quad A_1 = 4A_2 \quad A_2 = \frac{\mathrm{Tr}\,\sigma}{24c^2} \\ B_0 = 0 \quad B_1 = 4B_2 \quad B_2 = \frac{\rho}{12c^2} \\ C_0 = -\frac{2\rho}{3c^2} \quad C_1 = 4C_2 \quad C_2 = -\frac{\rho}{24c^2} \\ D_0 = 0 \quad D_1 = 4D_2 \quad D_2 = \frac{\rho}{8c^4} \\ G_s^{\alpha\beta} = 0 \quad G_s^{\alpha\beta} = 4G_2^{\alpha\beta} \quad G_2^{\alpha\beta} = \frac{\sigma^0_{\alpha\beta}}{8c^2}, \end{aligned} \tag{66}$$

where we denoted by $\sigma^0_{\alpha\beta}$ the traceless part of $\sigma_{\alpha\beta}$.

One can now proceed to recover the Navier-Stokes equation by using a Chapman-Enskog expansion[6]. We will also assume that the fluid is incompressible and ignore third-order terms in the fluid velocity.

Taking the first moment of Eq. (41), one gets

$$\partial_{t_1}(\rho v_\alpha) + \partial_{\beta_1}\left(\rho v_\alpha v_\beta\right) = \partial_{\beta_1}\sigma_{\alpha\beta} + \mathcal{O}(\epsilon), \tag{67}$$

which is the Navier-Stokes equation at first order in Knudsen number. To recover the Navier-Stokes equation at second order, we start from Eq. (55), where we need to evaluate the second moment of $f_i^{(1)}$

$$\begin{aligned} \sum_i f_i^{(1)}\xi_{i\alpha}\xi_{i\beta} &= -\tau\Delta t(\partial_{t_1} + \xi_{i\gamma}\partial_{\gamma_1})\left(\sum_i f_i^{eq}\xi_{i\alpha}\xi_{i\beta}\right) \\ &= -\tau\Delta t\left[\partial_{t_1}\left(-\sigma_{\alpha\beta} + \rho v_\alpha v_\beta\right) + \partial_{\gamma_1}\left(\sum_i f_i^{eq}\xi_{i\alpha}\xi_{i\beta}\xi_{i\gamma}\right)\right], \end{aligned} \tag{68}$$

The first time derivative in square brackets is negligible at the leading order under the assumption of incompressibility [49], while

$$\partial_{t_1}(\rho v_\alpha v_\beta) = v_\alpha \partial_{t_1}(\rho v_\beta) + v_\beta \partial_{t_1}(\rho v_\alpha) \tag{69}$$

that shows, together with Eq. (67), that this term gives a null contribution. Finally, using Eq. (57) we get

$$\sum_i f_i^{(1)}\xi_{i\alpha}\xi_{i\beta} = -\tau\Delta t\frac{c^2}{3}\rho\left[\partial_{\beta_1} v_\alpha + \partial_{\alpha_1} v_\beta\right], \tag{70}$$

[6] The second moment constraint on the equilibrium distribution functions is not necessary for the derivation of the continuity equation. Hence the procedure to recover this equation is not affected by the modifications introduced in the new version of the algorithm.

the same result of Eq. (59) which allows one to restore the Navier-Stokes equation.

3.3.2 Second method

An alternative route to the solution of the LB equation (20) relies on the use of a pure forcing method [48, 139]. In this case the total stress tensor enters the model via a forcing term $\mathcal{F}_i$ without any additional constraint on the second moment of the equilibrium distribution functions, as done in Eq. (64). The collision term $\mathcal{C}_{f_i}$ assumes the simple form of the BGK approximation supplemented by a forcing term

$$\mathcal{C}(\{f_i\},t) = -\frac{1}{\tau}[f_i(\boldsymbol{r},t) - f_i^{eq}(\boldsymbol{r},t)] + \Delta t \mathcal{F}_i, \qquad (71)$$

where the equilibrium distribution functions f_i^{eq} are again expressed as a second-order expansion in the velocity $\boldsymbol{v}$ of the Maxwell-Boltzmann distribution [137]. The fluid momentum is now given by

$$\rho v_\alpha = \sum_i f_i \xi_{i\alpha} + \frac{1}{2} F_\alpha \Delta t, \qquad (72)$$

where F_α is the cartesian component of the force density acting on the fluid. The choice of the equilibrium distribution functions and of their constraints is kept as in Section 3.2, with coefficients given by Eqs. (29)-(32) for a $D2Q9$ lattice. The term $\mathcal{F}_i$ can be written as an expansion at the second order in the lattice velocity vectors [140]:

$$\mathcal{F}_i = \omega_i \left[A + \frac{B_\alpha \xi_{i\alpha}}{c_s^2} + \frac{C_{\alpha\beta}(\xi_{i\alpha}\xi_{i\beta} - c_s^2 \delta_{\alpha\beta})}{2c_s^4} \right], \qquad (73)$$

where coefficients A, B_α and $C_{\alpha\beta}$ are functions of F_α. In order to correctly reproduce hydrodynamics equation, the moments of the force must verify the following relations

$$\begin{aligned} \sum_i \mathcal{F}_i &= A \qquad & \sum_i \mathcal{F}_i \xi_{i\alpha} &= B_\alpha \\ \sum_i \mathcal{F}_i \xi_{i\alpha}\xi_{i\beta} &= c_s^2 A \delta_{\alpha\beta} + \frac{1}{2}\left[C_{\alpha\beta} + C_{\beta\alpha}\right], \end{aligned} \qquad (74)$$

which lead to [141]

$$\mathcal{F}_i = \left(1 - \frac{1}{2\tau}\right) \omega_i \left[\frac{\xi_{i\alpha} - v_\alpha}{c_s^2} + \frac{\xi_{i\beta} v_\beta}{c_s^4} \xi_{i\alpha} \right] F_\alpha, \qquad (75)$$

To recover the continuity (12) and the Navier-Stokes (13) equations it suffices to require that

$$F_\alpha = \partial_\beta (\sigma_{\alpha\beta}^{total} - \sigma_{\alpha\beta}^{viscous}). \qquad (76)$$

From the Chapman-Enskog expansion (see Appendix B for the details of the calculation) it results that the fluid viscosity in Eq. (16) is $\eta = \rho \Delta t c_s^2 (\tau - 1/2)$. No extra contributions appear in the continuum equations (12) and (13), apart from a term of order v^3 which can be neglected if the Mach number is kept small. With this formulation, the effects of the stress tensor are not included in the second moment of the equilibrium distribution functions, as done in Section 3.3.1. The fluid momentum is measured as the average between the pre- and post-collisional values of the velocity v, as usually done when using a forcing term [142, 143].

Other approaches to the numerical solution of the LB equation introduce spurious terms which cannot always be kept under control. For a complete discussion the interested reader may refer to Ref. [141]. The one presented here has proved to be effective for simple fluids [141], multi-component [144] and multi-phase fluid systems [145, 146] even though, as far as we known, a full external forcing algorithmm has not been applied to active systems yet.

3.4 Coupling with convection-diffusion equation

The scope of Lattice Botlzmann goes far beyond the treatment of hydrodynamics; indeed it has proven to be a fundamental tool to solve general conservation equations [147]. Beside many implementations devoted to hydrodynamics studies, such as the ones cited at the end of the previous section, recently a LB approach has also been used to solve Einstein equations for gravitational waves [148].

To furnish an example of how LB can be generalized to solve generic partial differential equations we devote this section to report on two characteristic ways to solve the dynamics of order parameters coupled to hydrodynamics in a fluid system. Because of its semplicity, in the following of this section we will focus on the treatment of the convection-diffusion equation (19) for a concentration field. The first possibility is to develop a full LBM approach in which the convection-diffusion equation is solved by introducing a new set of distribution functions $\{g_i(\boldsymbol{r},t)\}$ connected to the concentration field, beside the distribution functions $\{f_i(\boldsymbol{r},t)\}$ needed to solve the hydrodynamics. Another route is to follow a hybrid approach where the convection-diffusion equation is solved via a standard finite difference algorithm while hydrodynamics is still solved through a LB algorithm.

Full LBM approach To solve the hydrodynamic equations for a binary system through a full LB approach the introduction of a new set of distribution functions $\{g_i(\boldsymbol{r},t)\}$ is needed. The index i again assigns each distribution function to a particular lattice direction indicated by the velocity vector $\boldsymbol{\xi}_i$. The concentration field $\phi(\boldsymbol{r},t)$ is thus defined as

$$\phi(\boldsymbol{r},t) = \sum_i g_i(\boldsymbol{r},t). \qquad (77)$$

As in standard Lattice-Boltzmann model, these distribution functions evolve according to the following equation

$$g_i(\boldsymbol{r} + \boldsymbol{\xi}_i \Delta t, t + \Delta t) - g_i(\boldsymbol{r},t) = -\frac{1}{\tau_\phi}(g_i - g_i^{eq}), \qquad (78)$$

where the BGK approximation for the collisional operator has been used. A new relaxing time τ_ϕ has been introduced since the relaxing dynamics of the concentration field may consistently differ from that of the underlying fluid. In Eq. (78) we have also introduced the set of equilibrium distribution functions $\{g_i^{eq}(\boldsymbol{r},t)\}$ that fulfill the following relation

$$\sum_i g_i^{eq}(\boldsymbol{r},t) = \phi(\boldsymbol{r},t). \tag{79}$$

This ensures that the concentration field is conserved during the evolution.

To recover the convection-diffusion equation in the continuum limit, it is necessary to impose the following constraints on the first and second moment of the equilibrium distribution functions

$$\sum_i g_i^{eq}\xi_{i\alpha} = \phi v_\alpha, \tag{80}$$

$$\sum_i g_i^{eq}\xi_{i\alpha}\xi_{i\beta} = \phi v_\alpha v_\beta + c^2\tilde{\gamma}\mu\delta_{\alpha\beta}. \tag{81}$$

Here the mobility parameter $\tilde{\gamma}$ tunes the diffusion constant M that appears on the right-hand side of the convection-diffusion equation. A suitable choice of the distribution function which fulfills Eq. (79), Eq. (80) and Eq. (81) can be written as a power expansion up to the second order in the velocity

$$g_i^{eq} = H_s + J_s v_\alpha \xi_{i\alpha} + K_s v^2 + M_s v_\alpha v_\beta \xi_\alpha \xi_\beta, \tag{82}$$

where again the index $s = |\boldsymbol{\xi}_i|^2/c^2$ relates the i-th distribution function to the corresponding lattice velocity, and the coefficients of the expansion can be computed from Eqs. (66) through the formal substitution

$$\rho \to \phi \qquad \sigma_{\alpha\beta} \to -c^2\tilde{\gamma}\mu\delta_{\alpha\beta}. \tag{83}$$

The continuum limit of the convection-diffusion equation can be performed through a Taylor expansion of the left-hand side of Eq. (78) and by using Eqs. (79)-(81) [47]. This leads to the following expression of the diffusion constant

$$M = \tilde{\gamma}c^2\Delta t\left(\tau_\phi - \frac{1}{2}\right). \tag{84}$$

This algorithm can be generalized to describe the evolution of more complex order parameters, such as the nematic tensor $Q_{\alpha\beta}$, whose dynamics is governed by the Beris-Edwards equation of motion (Eq. (17)). Since $Q_{\alpha\beta}$ is a traceless symmetric tensor, in d dimensions, at least $d(d+1)/2-1$ extra distribution functions $\{G_{i,\alpha\beta}(\boldsymbol{r},t)\}$ are needed, which are related to $Q_{\alpha\beta}$ through

$$Q_{\alpha\beta} = \sum_i G_{i,\alpha\beta}. \tag{85}$$

The rest of the algorithm can be thus developed as the one presented for the concentration field. In Section 3.5 we will go back to LBM for liquid crystal dynamics and we will present another algorithm that employs a predictor-corrector numerical scheme.

Hybrid LBM approach An alternative approach to solve the Navier-Stokes equation and a convection-diffusion equation for an order parameter is based on a hybrid method, in which a standard LBM solves the former while a finite-difference scheme integrates the latter.

Let us consider, for instance, the evolution equation (19) of the concentration field $\phi(\boldsymbol{r},t)$. Space $\boldsymbol{r}$ and time t can be discretized by defining a lattice-step Δx_{FD} and a time-step Δt_{FD} for which $\Delta x_{FD} = \Delta x_{LB}$ (namely the scalar field is defined on the nodes of the same lattice used for the LB scheme) and $\Delta t_{LB} = m\Delta t_{FD}$, with m positive integer. At each time step the field ϕ evolves according to Eq. (19) and is updated in two partial steps.

1. Update of the convective term by means of an explicit Euler algorithm

$$\phi^*(\boldsymbol{r}_\alpha) = \phi - \Delta t_{FD}(\phi\partial_\alpha v_\alpha + v_\alpha\partial_\alpha\phi), \tag{86}$$

   where all variables appearing at the right-hand side are computed at position $\boldsymbol{r}_\alpha$ and time t. Note that the velocity field $\boldsymbol{v}$ is obtained from the lattice Boltzmann.
2. Update of the diffusive part

$$\phi(\boldsymbol{r}_\alpha, t+\Delta t_{FD}) = \phi^* + \Delta t_{FD}\left(\nabla^2\frac{\delta\mathcal{F}}{\delta\phi}\right)_{\phi=\phi^*} \tag{87}$$

Such method, besides being relatively simple to implement, combines a good numerical stability with a reduced computational cost with respect to the full LBM approach [48]. In fact in this latter case, for each field to evolve, one would need a number of distribution functions equal to the number of lattice velocities, significantly increasing the amount of memory necessary at runtime.

In addition the LB algorithm shows reduced computational costs with respect to other approaches. For instance, while the number of floating point operations needed to integrate the hydrodynamics equations on a $L\times L$ square grid is $\sim L^D$ for LBM (where D is the spatial dimension of the system), it is of order $\sim (\ln L)L^D$ for pseudo-spectral models [149]. It is thus evident that on sufficiently big computational grids the time performance of LB algorithm is better than the equivalent pseudo-spectral methods.

3.5 LBM for Active Fluids

As outlined in Section 2, many properties of active matter are captured by liquid crystal hydrodynamics. Here we describe a LB method that solves both the Navier-Stokes equation and the Beris-Edwards equation through a full LB approach, a method often employed to numerically investigate active matter [49,62].

As the liquid crystal stress tensor entering the Navier-Stokes equation is generally not symmetric, one could either (i) build an algorithm in which it is fully included through an external forcing term (as described in Section 3.3.2) or (ii) separate the symmetric part from the antysimmetric one, by including the former in the second moment of the equilibrium distribution functions and

treating the latter as an external forcing term. Although the two procedures are equivalent, only the second approach, first introduced by Denniston *et al.* [49], has been developed so far.

In this method two sets of distribution functions, $\{f_i\}$ and $\{G_{i,\alpha\beta}\}$, are defined and are connected to the hydrodynamics variables (i.e. density, momentum and order parameter) through Eqs. (23), (24) and (85). Their evolution equations are solved by using a predictor-corrector-like scheme

$$f_i(\boldsymbol{r}+\boldsymbol{\xi}_i\Delta t, t+\Delta t) - f_i(\boldsymbol{r},t) = \frac{\Delta t}{2}\left[\mathcal{C}(\{f_i\},\boldsymbol{r},t) + \mathcal{C}(\{f_i^*\},\boldsymbol{r}+\boldsymbol{\xi}_i\Delta t, t+\Delta t)\right], \tag{88}$$

$$G_{i,\alpha\beta}(\boldsymbol{r}+\boldsymbol{\xi}_i\Delta t, t+\Delta t) - G_{i,\alpha\beta}(\boldsymbol{r},t) = \frac{\Delta t}{2}\left[\mathcal{C}(\{G_{i,\alpha\beta}\}\boldsymbol{r}+\boldsymbol{\xi}_i\Delta t, t) + \mathcal{C}(\{G_{i,\alpha\beta}\}\boldsymbol{r}+\boldsymbol{\xi}_i\Delta t, t)\right], \tag{89}$$

where f_i^* and $G^*_{i,\alpha\beta}$ are respectively first order approximation to $f_i^*(\boldsymbol{r}+\boldsymbol{\xi}_i\Delta t, t+\Delta t)$ and $G^*_{i,\alpha\beta}(\boldsymbol{r}+\boldsymbol{\xi}_i\Delta t, t+\Delta t)$ obtained by setting $f_i^* \equiv f_i$ and $G^*_{i,\alpha\beta} \equiv G_{i,\alpha\beta}$ in Eq. (88) and (89). The collisional terms are given by a combination of the usual collision operator in the BGK approximation plus a forcing term

$$\mathcal{C}(\{f_i\},\boldsymbol{r},t) = -\frac{1}{\tau_f}(f_i - f_i^{eq}) + p_i, \tag{90}$$

$$\mathcal{C}(\{G_{i,\alpha\beta}\},\boldsymbol{r},t) = -\frac{1}{\tau_G}(G_{i,\alpha\beta} - G^{eq}_{i,\alpha\beta}) + M_{i,\alpha\beta}, \tag{91}$$

where τ_f and τ_G are two distinct relaxation times, and p_i and $M_{i,\alpha\beta}$ are the two additional forcing terms.

In order to recover continuum equations one must impose constraints on the zeroth, first and second moments of the equilibrium distribution functions and on the forcing terms. The local conservation of mass and momentum is ensured by (25) and (26), while the second moment is given by Eq. (64), in which the stress tensor on the right hand side includes the sole symmetric part. The antisymmetric contribution $\sigma^{anti}_{\alpha\beta}$ is introduced through the forcing term p_i, which fulfills the following relations

$$\sum_i p_i = 0, \qquad \sum_i p_i\xi_{i\alpha} = \partial_\beta \sigma^{anti}_{\alpha\beta}, \qquad \sum_i p_i\xi_{i\alpha}\xi_{i\beta} = 0. \tag{92}$$

The remaining distribution functions $G_{i,\alpha\beta}$ obey the following equations

$$\sum_i G^{eq}_{i,\alpha\beta} = Q_{\alpha\beta},$$

$$\sum_i G^{eq}_{i,\alpha\beta}\xi_{i\gamma} = Q_{\alpha\beta}v_\gamma,$$

$$\sum_i G^{eq}_{i,\alpha\beta}\xi_{i\gamma}\xi_{i\delta} = Q_{\alpha\beta}v_\gamma v_\delta,$$

while the forcing term $M_{i,\alpha\beta}$ satisfies

$$\sum_i M^{eq}_{i,\alpha\beta} = \Gamma H_{\alpha\beta} + S_{\alpha\beta},$$

$$\sum_i M^{eq}_{i,\alpha\beta}\xi_{i\gamma} = \left(\sum_i M^{eq}_{i,\alpha\beta}\right) v_\gamma.$$

We finally note that the predictor-corrector scheme has been found to improve the numerical stability of the algorithm and to eliminate lattice viscosity effects (usually emerging from the Taylor expansion and appearing in the viscous term, in the algorithms discussed so far) to the second order in Δt. To show this, one can Taylor expand equation (88) to get

$$(\partial_t + \xi_{i\alpha}\partial_\alpha) f_i(\boldsymbol{r},t) - \mathcal{C}(\{f_i\}) = -\frac{\Delta t}{2}(\partial_t + \xi_{i\alpha}\partial_\alpha)\left[(\partial_t + \xi_{i\alpha}\partial_\alpha) f_i - \mathcal{C}(\{f_i\})\right] + \mathcal{O}(\Delta t^2). \tag{93}$$

The left-hand side is of $\mathcal{O}(\Delta t)$ and coincides with the term in square brackets. One could then write at second order in Δt

$$(\partial_t + \xi_{i\alpha}\partial_\alpha) f_i(\boldsymbol{r},t) = \mathcal{C}(\{f_i\}) + \mathcal{O}(\Delta t^2). \tag{94}$$

An analogous calculation for $G_{i,\alpha\beta}$ shows that

$$(\partial_t + \xi_{i\gamma}\partial_\gamma) G_{i,\alpha\beta}(\boldsymbol{r},t) = \mathcal{C}(\{G_{i,\alpha\beta}\}) + \mathcal{O}(\Delta t^2), \tag{95}$$

thus recovering the proper Lattice Boltzmann equations.

A hybrid version of the algorithm, widely employed in the study of active matter, solves the Navier-Stokes equation through a predictor-corrector Lattice-Boltzmann approach and the Beris-Edward equation by means of a standard finite-difference method [62, 150].

Further models involving more than just one order parameter have been developed in recent years, such as the theory discussed in Section 2.4, in which the liquid crystal order parameter (the polarization field) is coupled to the concentration field of a binary fluid mixture. Again a hybrid approach, in which both equations of the concentration and of the polarization have been solved through finite difference methods, has been used [110, 151].

3.6 Boundary conditions

In many practical situations, such as in a system under shear flow, one may be interested in studying the physics of the system within a confined geometry. In this section we describe the implementation of boundary conditions of a sheared bidimensional fluid defined on a lattice of size $L_x \times L_y$ and confined between two parallel flat walls located at $y = 0$ and $y = L_y$. Two key requirements are necessary for a correct description of the physics:

- no flux accross the walls,
- fixed velocity v_x^* along the walls.

which correspond to the following relations on the wall sites:

$$\sum_i f_i \xi_{ix} = \rho v_x^*, \qquad \sum_i f_i \xi_{iy} = 0. \tag{96}$$

Assuming a $D2Q9$ lattice geometry (see Fig. 5) with the walls located along the lattice links (i.e. along the lattice vectors $\boldsymbol{\xi}_1$,$\boldsymbol{\xi}_3$), one can explicitly write the previous relations at $y = 0$ (the bottom wall):

$$f_2 + f_5 + f_6 - f_4 - f_7 - f_8 = 0, \tag{97}$$
$$f_1 + f_5 + f_8 - f_3 - f_6 - f_7 = \rho v_x^*. \tag{98}$$

Notice that after the propagation step, functions f_0, f_1, f_4, f_7 and f_8 are known, so that one can use relations (97) and (98) to determine the three unknown distribution functions f_2, f_5, f_6. This system of equations can be closed by adding the bounce-back rule:

$$f_2 = f_4. \tag{99}$$

The two remaining distribution functions f_5 and f_6 are then given by [152]

$$f_5 = \frac{1}{2}(2f_7 + f_3 - f_1 + \rho v_x^*) \tag{100}$$
$$f_6 = \frac{1}{2}(2f_8 + f_1 - f_3 - \rho v_x^*). \tag{101}$$

With this choice for inward-pointing distributions, the desired momentum at the boundary is achieved. Unfortunately this scheme does not allow for the local conservation of mass since, after the collision step, inward-pointing distributions are not streamed. In [153] an improvement of this scheme was proposed to overcome such a problem. In the following we will use notation f_{pi} to identify the outgoing distribution function in a wall lattice site at time $t - \Delta t$, while f_i denotes those streamed from neighboring sites at time t. Besides conditions in (96) it is required that the fraction of mass moving towards the wall or eventualy still on a wall site at time $t - \Delta t$ is the same that moves from the wall or stay still on the walls at time t. This is expressed for a bottom-wall site by the following relation:

$$f_{p0} + f_{p7} + f_{p4} + f_{p8} = f_0 + f_5 + f_2 + f_6, \tag{102}$$

where f_0 must be determined by solving the system of Eqs. (96) and (102) together with the bounce-back condition (99). This leaves unchanged the solutions for the unknown f_5 and f_6 in Eqs. (100) and (101), but provides a new expression for f_0 that is thus given by:

$$f_0 = \rho - (f_1 + f_3) - 2(f_4 + f_7 + f_8). \tag{103}$$

Such scheme can be easily adjusted to the case of the pure forcing method presented in Sec. 3.3.2. The only difference lies in the momentum conservation relations [154] that in such case read as follows,

$$\sum_i f_i \xi_{ix} + \frac{\Delta t}{2} F_x = \rho v_x^*, \qquad \sum_i f_i \xi_{iy} + \frac{\Delta t}{2} F_y = 0. \tag{104}$$

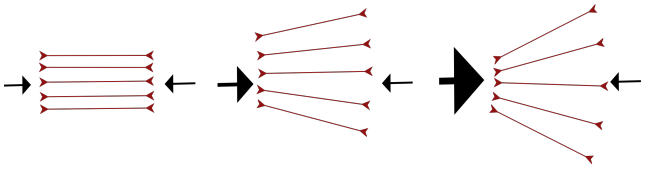

Fig. 6. Sketch of instability and spontaneous symmetry breaking mechanism for contractile systems. When the system is completely ordered (left panel) force dipoles compensate each other, while if a splay deformation is present (middle panel) the density of contractile forces is greater on the left than on the right. This determines a flow that produces further splay (right panel), resulting in a macroscopic flowing state.

The system of Eqs. (104) together with Eq. (102) admits the following solutions:

$$f_5 = \frac{1}{2}\left(2f_7 + f_3 - f_1 + \rho v_x^* - \frac{\Delta t}{2}(F_x + F_y)\right), \tag{105}$$
$$f_6 = \frac{1}{2}\left(2f_8 + f_1 - f_3 - \rho v_x^* + \frac{\Delta t}{2}(F_x - F_y)\right), \tag{106}$$
$$f_0 = \rho - (f_1 + f_3) - 2(f_4 + f_7 + f_8) + \frac{\Delta t}{2} F_y, \tag{107}$$

where the outward-pointing distribution f_2 was fixed by the bounce back condition (96).

4 Spontaneous flow

Many remarkable phenomena in the physics of active fluids are hydrodynamical consequences of the presence of active forcing in the dynamical equations of the fluid. The first effect that was studied, to which this section is devoted, is the occurrence of spontaneous flow in fluids with sufficiently strong activity. Numerical methods, and LBM in particular, have been essential in the study of this problem, both for supporting theoretical analysis of instabilities and for the understanding of non-linear regimes. Here we will put the accent on numerical studies, while a more complete review of analytical studies of instabilities in active fluids can be found in [3].

The hydrodynamic description of suspensions of self-propelled particles, described in Sect. 2.5 with Eqs. (6) or (7), was first given in [18]. In this work the possible instabilities of different modes were also discussed: contractile and extensile gels are unstable to splay and bend respectively, giving rise to a macroscopic flow. It has also been shown that orientational order is destabilized by small wave number perturbations by splay of the axis of orientation, with a velocity field oriented at 45 degrees with respect to this axis. Bend and twist waves are also predicted that in absence of hydrodynamics would reduce to simply diffusively decaying modes. To understand the mechanism proposed in [18], let us consider the case of contractile dipoles initially perfectly ordered, as in the sketch on the left of Fig.6. In this situation the force

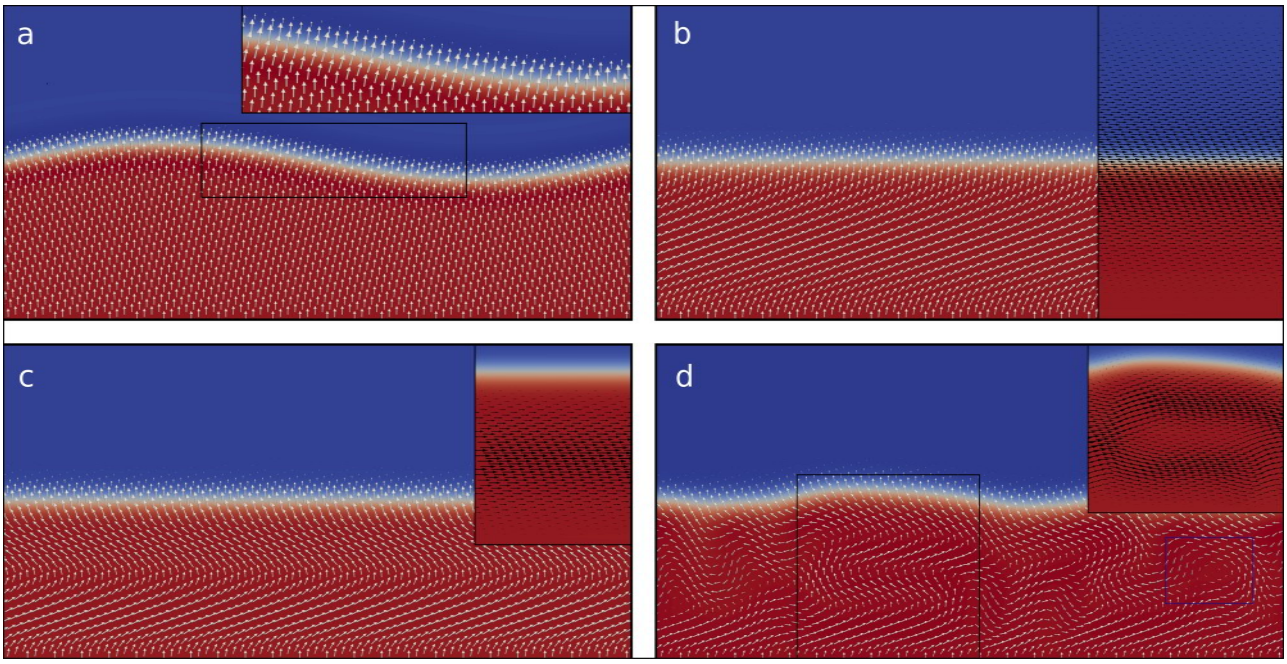

Fig. 7. Instability and spontaneous flow in extensile mixtures. The polarization field is confined in one of the phases of a binary mixture and satisfies hometropic anchoring both at the lower bound of the channel and at the interface between the two fluid components; moreover the interface is modulated in a sinusoidal fashion, determining a weak splay instability in the polarisation field, as shown in panel (a). Starting from this configuration and turning on the extensile activity, two regimes are found. For weak active doping, shown in panel (b), the interface relaxes towards a flat profile and the polarisation pattern undergoes bending deformations, while the velocity field, shown in the right part of panel (b), is parallel to direction of the channel and confined in proximity of the interface. If activity is raised, the bending deformations of the polarisation field are tightened (as clearly visible in panel (c)) and a unidirectional flow field develops in centre of the polar fluid and mostly parallel to the walls (see the corresponding inset). When active doping exceeds a critical threshold (see panel (d)) the polarisation field undergoes instabilities leading to the formation of chaotic non-stationary polarisation patterns. In such condition the interface loses its flat profile, although the velocity field remains roughly parallel to the channel direction.

dipoles balance each other and the net flow, obtained by the sum of those due to the single dipoles represented in Fig. 4, is null. However, if a small splay deformation is present (middle panel in Fig.6), the density of contractile forces on the left is larger than that on the right, and a flow sets up. This flow causes further splay which destabilizes the system that starts to flow macroscopically. For extensile activity, under the same splay deformation the initial flow (directed to the left in this case) would align the dipoles and no net macroscopic flow would appear. By repeating the same argument used for contractile fluids, it can be shown that extensile fluids get unstable to bend deformations.

The spontaneous flow instability for contractile systems was illustrated in [63] for the simple geometry of a bidimensional thin film confined on a one-dimensional substrate, with planar anchoring on the confining surfaces. For small thicknesses or small activity, boundary effects are prevailing and the gel remains in an unperturbed, static, homogeneously polarized state. Above a critical thickness or a critical activity, a polarization tilt appears and the system flows with a finite shear gradient. The previously mentioned analysis has been later extended to films where undulations of the free surface are also considered [3,155]. In particular Sankararaman et. al [155] constructed dynamical equations for the concentration field, the polarization field and the height of the film thickness. Activity was found to have two main effects on the evolution of the height field: (i) a splay induced flow that tilts the free surface and (ii) an active contribution to the effective tension. The latter can be understood by noting that active stresses pull or push the fluid along the long axis of the particles, giving additional elastic contribution to the stretching along that axis. Through stability analysis they found that, for contractile stresses, splay destabilizes **the surface?**, while the activity contribution to tension stabilizes the surface. For extensile activity the opposite happens.

The previous results are illustrated in Figs.7 and 8. Here the onset of instability and spontaneous flow is shown for the polar active binary mixture described in section 2.4, in which an active polar gel coexists with a passive component. Homeotropic anchoring is set both at the lower bound of the channel and at the interface between

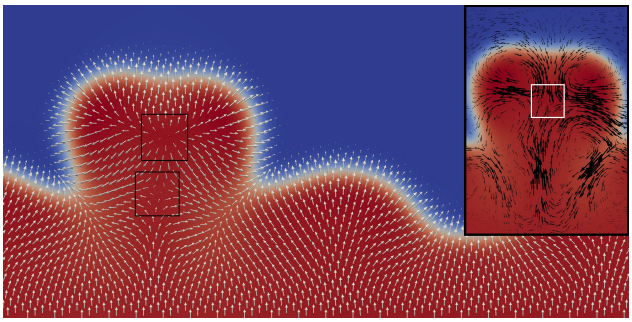

Fig. 8. Splay deformation and defect formation in a contractile mixture. Starting from condition presented in panel (a) of Fig. 7, strong contractile activity is imposed in the system. This leads to a catastrophic dynamics: the splay deformation of the initial condition is tightened until the initial sinusoidal shape in the interface between the two fluids is completely lost and replaced with an undulated profile driven by splay deformations of the polarisation, as clearly visible in the center of the system. Notice also the formation of two defects of opposite charge that have been framed with two black squares. Defect formation strongly influences the hydrodynamics of the system, as shown in the inset, where the velocity field develops a quadrupolar backflow in their neighborhood.

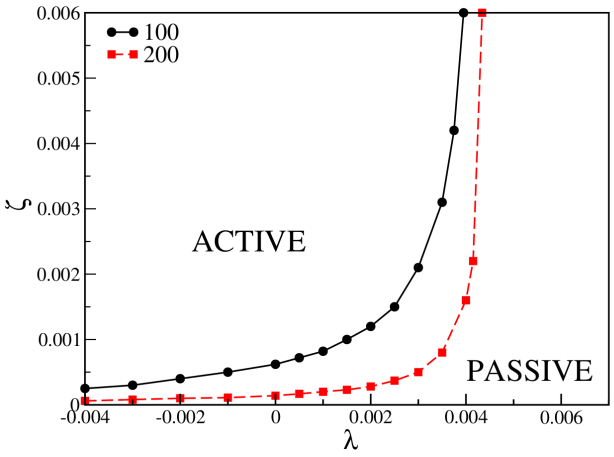

Fig. 9. Phase diagram from [13] in the two activity parameters plane (λ, ζ) for an active nematic liquid crystal. The lines define regions of passive immotile state, and active, macroscopic motile state for two different system sizes.

the two fluid components. The system is numerically studied by means of a hybrid Lattice Boltzmann method which combines a LB treatment for the Navier-Stokes equation with a finite difference algorithm to solve the order parameters dynamics (Section 3.5). The interface is initially modulated by a sinusoidal perturbation, determining a weak splay pattern in the polarization field, as shown in Fig. 7(a). As expected, for weak extensile activity, the system is stable under splay deformations which are replaced by static bending patterns (see Fig. 7(b)). These give rise to a macroscopic flowing state as it can be seen by looking at the velocity field in the zooms of Figs. 7(b) and 7(c), with the polarization field becoming unstable for sufficiently high activity (Fig. 7(d)). Strong contractile activity tightens splay deformations of the initial condition until, by increasing the strength of activity, as shown in Fig. 8, the initial sinusoidal shape of the interface between the two fluids is completely lost and replaced by a irregular profile driven by splay deformations of the polarisation field. Fig. 8 also shows the presence of two defects of opposite charge (+1 and −1), framed with two black squares. They strongly influence the velocity pattern of the system, as shown in the inset where a quadrupolar backflow can be observed in their neighborhood.

The first papers where spontaneous flow was systematically studied numerically were [13,156]. A two-dimensional nematic gel confined between two walls with different anchoring conditions was studied by a hybrid version of LBM. The model is the same of that described in Section 2 for active nematic liquid crystals. The dynamics of the order parameter $\mathbf{Q}$ is governed by Eq. (17), with Ξ replaced by $\mathbf{Q}$ and $\mathbf{S}$ given in the last row of Table 2, with an extra active term, besides the active stress term in the NS equations, of the form $\lambda\mathbf{Q}$. This term was suggested on the basis of symmetry considerations and also obtained by a microscopic derivation in [39]. λ is positive for systems with self alignment effects [63], like concentrated actomyosin suspensions, and negative for dilute suspensions. The main results concerning the occurrence of spontaneous flow are summarized in Fig. 9 for two different system width $L = 100,200$, which confirm the presence of a transition between a passive and an active phase as predicted analytically. For small L or small ζ there is no flow and the polarization field is homogeneous. In the active phase instead a spontaneous flow is observed. Alongside the activity parameters ζ and λ, the other key parameter is the flow alignment parameter ξ. In fact the transition is attained for sufficiently extensile suspensions, in the case of flow-aligning ($|\xi| > 1$) liquid crystals, and for sufficiently contractile ones for flow-tumbling materials ($|\xi| < 1$). In the flow-aligning case the velocity profile is characterized by the presence of bands, i.e. areas of constant shear, separated by narrow regions where the shear gradient reverse, similar to shear bands in non active materials [157] with the number of wavelengths in the channel increasing with ζ. Flow tumbling materials rearrange themselves so that only the two boundary layers flow in steady state. Two-dimensional simulations, with periodic boundary conditions, show additional instabilities, with the spontaneous flow appearing as patterns made up of convection rolls. Boundary conditions for the model in [13] are described in detail in [158], while the numerical method in [159]. The complete phase diagram was studied, for a quasi-1D system, in [160], extending previous works to the complete (ξ, ζ) plane, varying also the initial orientation of the the director field.

A detailed numerical study of the dynamical spontaneous flow transition in polar active films (not by LBM

but directly integrating dynamic equations) is presented in [161]. In this work the effects of varying concentration were explicitly taken into account. The free-energy of the model is similar in spirit to that of Eq.(9) but only one phase for the concentration of the active fluid is considered (the free-energy is at most quadratic in the concentration field and no phase separation phenomena can occur). The phase diagram in a plane of two variables related to activity ζ and a parameter that controls self-advection of the polarization field, shows the transitions to spontaneous flow and, for high activity and self-advection, to a spontaneous periodic oscillatory banded flow. The latter, accompanied by strong concentration inhomogeneities, is not present in active nematic systems. We finally mention another LBM study on spontaneous flow, where the effects of a phenomenological term $\tilde{\lambda}\mathbf{v}$ in the dynamic equation for the polarization field $\mathbf{P}$(Eq. (17)), favouring the alignment between the polarization field and the velocity, were studied [110]. It was shown that the interplay between alignment and activity gives rise to very different behaviors under different boundary conditions and depending on the contractile or extensile character of the fluid. Due to the competition between alignment and activity-induced spontaneous flow, which would tend to favour misaligned patterns, stationary active patterns are transformed into continuously moving ones that can be either chaotic or oscillatory according to the strength of the alignment term.

The occurrence of spontaneous flow may also be accompanied by the formation of topological defects. In fact the dynamics of the order parameter field and the velocity field are interconnected through a feedback loop. The hydrodynamics instabilities give rise to lines of distortions in the order parameter field that are unstable to the formation of defect pairs [86]. In [162,163] an extensile active nematic has been considered and the dynamics of defects characterized. Two main stages have been identified: first ordered regions undergo hydrodynamic instability generating lines of strong bend deformation that relax by forming oppositely charged pairs of defects. Annihilation of defect pairs of different charge restores nematic ordered regions wich undergo further instabilities. In passive liquid crystals the coupling between the order parameter and the flow has significant effect on the motion of defects, generating a more intense flow around positive charged defects than for negative charged ones [85]. This phenomenon is still present in active liquid crystals, as suggested by the quadrupolar flow centered around the +1 defects in the inset of Fig.8. The presence of activity gives rise to an even richer phenomenology. Full defects hydrodynamics in 2D polar active fluids was studied by lattice Boltzmann simulations with a hybrid scheme in [164]. In this paper it was found that extensile activity favours spirals and vortices, like the defect highlighted by a blue square in Fig. 7d, while contractile activity favours aster-like defects in the polarization field like the ones boxed in Fig. 8. The defect-defect interactions are also described. In a contractile fluid two asters repel each other reaching a steady state with a fixed distance, that increases increasing activity. In the extensile case two asters turn into two rotating spirals, leading to a final state where the rotation continues at approximately constant rotational velocity. For low activity the angular velocity increases with ζ, while above a critical value an oscillatory behavior is observed, where half clockwise rotation is followed by half an anticlockwise one, consistently with the previous cited oscillatory and chaotic behaviors appearing in spontaneous flow transition for high activity [13].

Defects dynamics is particularly rich in drops of active fluids. This is not surprising given the complexity of defect topology known for passive liquid crystals [165]. So far, numerical studies available are mostly concerned with two-dimensional systems, and we will give a review in the next section.

5 Self-propelled droplets

We have already discussed in the previous section the importance of boundary conditions and how they effects the hydrodynamics of an active fluid. In general geometrical constraints greatly affect the defects patterns in passive liquid crystals and this suggest a very rich phenomenology also in confined active fluids. In an active nematic droplet on a substrate for example, imposing no normal componetn of the orientation field at any bounding surface leads to inhomogeneities in the active stress that generate flows driving the spreading process with novel growth laws and drop shapes. This was first studied alatically in [166], under conditions of partial wetting with small equilibrium contact angle, and local polarization anchored parallel to the surface of the drop. In 1+1 dimensions the shape of the standing drop is determined primarily by the interplay of active stresses and surface tension, with the liquid- crystal elasticity of the ordered filaments playing a role near the contact line. In a three-dimensional drop, the anchoring conditions impose the existence of defects in the polarization field, and the nature of the active stresses play a central role, as extensile active stresses lead to flat drops whereas contractle droplets are fatter than passive ones. Diffeerent defects also determine different kinetics and final states. Aster-like defect line at the centre of the drop lead to a linear growth law of the the radius in time, while for a vortex defect, spreading is arrested at long enough times and the final height profile of the drop is a non-monotone function of radius.

Two-dimensional active droplet endowed with internal nematic or polar order and surrounded by an isotropic Newtonian fluid has been used as a minimal set up to try to mimic the basic mehacnis of crawling cells, cellular motility in bulk, intracellular movemnt, and transport [3]. The minimal models developed have helped to understand whether cell motion is sustained by continuous action of cells complex biochemical networks or subsist an autonomous physical mechanism of motility.

With this aim the motility and the spontaneous division of an active nematic droplet, described by a set of equations similar to Eqs. (13)-(17)-(19), was studied in [109] by finite difference methods. The initial configuration consists of a circular droplet of radius R, with director field

uniformly aligned, and forced to be normal at the inrface, and the flow velocity identically zero. The normal anchoring condition at the interface and the disk topology, would alone create in passive nematic droplets two $+1/2$ disclination(like the ones dipslayed in Fig. 2(a)) repelling each other. The repulsion is balanced by the surface tensions, leading to an elongation of the droplet along the line joining the defects [167].As explained in the previous section, in bulk systems, contractile and extensile active stresses favor, respectively, splayed and bent configurations of the nematic director through feedback mechanisms mediated by the flow. As aconsequence, a uniformly oriented reference configuration becomes unstable once the internal active stress exceeds a critical value. For a contractile droplet with homeotropic boundary, the axisymmetric structure of the director drives a typical quadrupolar straining flow, causing repulsion between the defects,

At sufficiently high contractile activity the interior of the droplet becomes unstable to splay and the no longer axially symmetric backflow causes the droplet to move. This motility mechanism is classified as a particular form of swimming: the droplet generates a flow in an ambient fluid and uses this to propel itself. Motility occurs as the combination of two processes: the initial elongation of the droplet, driven by the straining flow produced by the defects, and the instability of this configu- ration to splay. The existence of the intermediate elongated configuration is guaranteed by the fact that viscous and pressure forces exerted by the flow on the droplet are balanced by the resistance due to interfacial tension forces.

For large capillary numbers, the capillary forces are no longer sufficient to achieve this balance, the droplet continuously stretches and eventually divides before the splay instability can develop. Because of the interplay between the active stresses and the defective geometry of the nematic director, the system is able to mimic two of the defining functions of living cells: spontaneous division and motility.

The generic mechaniscm of motility of active polar dropelts was investigated in [65]. When the activity parameter exceeds a given threshold, an initially circular or spherical droplet spontaneously breaks that inversion symmetry, leading to an elastic splay of the polarity field and to motion along $\pm\mathbf{P}$. This spontaneous symmetry breaking manifests itself as a supercritical Hopf bifurcation, which can alternatively be viewed as a continuous nonequilibrium phase-transition.

Spontaneous motility of passive emulsion droplets in polar active gels was studied in [168]. When the polarisation of the active gel is anchored normal to the droplet at its surface, the formation of a hedgehog defect drives an active flow which propels the droplet forward. In an extensile gel, motility can occur even with tangential anchoring, which is compatible with a defect-free polarisation pattern??. In this case, upon increasing activity the droplet first rotates uniformly, and then undergoes a discontinuous nonequilibrium transition into a translationally motile state, powered by bending deformations in the surrounding active medium.

Finally, we mention one of the few three-dimensional studies concerning the dynamics of active droplets. The effects of microscopic chirality on the motility of active droplets were considered in [95]. Some of the features of the motility modes observed resemble those of some single-celled protozoa.

We have seen that spontaneous flow is particularly relevant for droplets since it is at the origin of their motile character. Therefore it is quite natural to have extended the previous studies to the description of biological cells. A minimal model capturing the behavior of crawling cells was introduced in [78].

The dynamics of cell motility and division and was also put in relation with the results found in [169]. Here active fluid droplets immersed in a two-dimensional external fluid are simulated using an Immersed Boundary method to describe the fluid droplet interface as a Lagrangian mesh.

6 Rheology

The flux generated by the presence of activity can interact with external flows to modify the rheological response of their suspension.

Many experimental studies have confirmed a decrease in viscosity for pushers and an increase for pullers. Sokolov et al. [16] confined *Bacillus subtilis* bacteria, which are pushers, in a quasi-2D liquid film. Their experiments yielded viscosity estimates below that of the solvent at low concentrations. At higher densities the viscosity was found to increase and exceed that of the solvent. More precise measurements using *E. coli* bacteria were obtained by Gachelin et al. [170] and Lopez [171]. In the former bacteria are indeed found to decrease the viscosity below that of the solvent for low shear rates. However the relative viscosity increases with the shear rate, reaching a maximum above unity before shear thinning again. Lopez performed their experiments in a conventional Tailor Couette rheometer specifically build to handle low torques and viscosities. The relative viscosity in their case displayed similar trends with shear rate, with a low-shear-ate plateau with relative viscosity less than one caused by activity, followed by shear thickening. Increasing the density of bacteria was found to decrease the value of the plateau towards zero, that means that the relative viscosity goes to zero. The measured viscosity, within experimental uncertainty, actually vanishes in oxygenated suspensions for volume fractions in excess of 1. This surprising superfluid-like behavior should not be seen as a violation of thermodynamic principles, as the bacteria consume chemical energy. Rather, it suggests that the viscous dissipation in the flowing suspension is macroscopically balanced by the input of energy from swimming, thus allowing for a sustained flow without any applied torque. The case of puller swimmers has been addressed by Rafai et al. [172], who measured the viscosity of a suspension of *Chlamydomonas reinhardtii* in a Taylor-Couette flow. The suspension viscosity was always found to exceed that of the medium and to increase with concentration.The effect of activity was

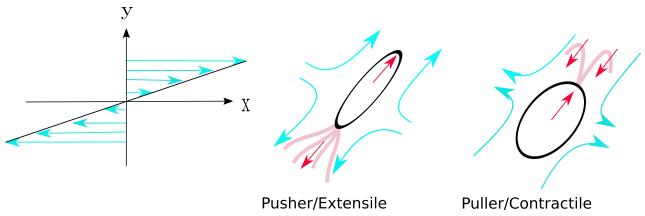

Fig. 10. Sketch of shear flow profile in a channel(cyan arrows on the left panel) compared to contractile (center panel) and extensile(right panel) flow.

spotted comparing the results between dead bacteria an living ones, with the suspension of leaving bacterial always being significantly more viscous than the dead one. Weak shear thinning was also reported for high shear rates. A direct comparison of three different types of swimmers was recently performed by McDonnel et al [173], considering *Dunaliella tertiolecta E. Coli* and *mouse sprematozoa*. In each case they compared live and dead cells. The viscosities measured were always above those of suspending medium, with living cells algae suspensions more viscous than dead ones, while both E. Coli and spermatozoa appeared less viscous when alive than dead.

Most experimental measurements and theoretical models have focused on the steady-flow rheology, but the competition between flow alignment and orientational realization produces viscoelastic behavior in unsteady flows. Lopez's experiments using E. Coli bacteria also analyzed the transient stress response upon startup and cessation of shear flow. They observe a platau at the steady viscosity measured two transient regime corresponding respectively to the switch on and the switch of the applied shear characterized by positive and negative peaks respectively appear. This stress overshoots followed by relaxation indicate elasticity. In [174] the superfluidic behavior has been experimentally investigated. They found that bacterial superfluids under shear exhibit unusual symmetric shear bands, defying the conventional wisdom on shear-banding of complex fluids, where the formation of steady shear bands necessarily breaks the symmetry of unsheared samples. The basic mechanism for viscosity modification by a suspension of microswimmers was first explained by Hatawalne et. al. [175]. They studied theoretically the rheology of SPP, making several predictions for the rheology of such systems. The main mechanism is sketched in Fig.10. Under an applied shear profile (left panel) extensile systems (middle panel) enforce the applied flow, decreasing the viscosity of the suspension, while the flow generated by contractile systems opposes to the external flow thus resulting in an increase of the apparent viscosity.

They first derive the coarse-grained equations governing the rheology of suspensions of active particles, and derived several predictions later validated by simulations and experiments. Liverpool et al. [176] did the same kind of study for polar active gels. They start form a molecular model, and they derive the constitutive equations for the stress tensor in the isotropic phase and in phases with liquid crystalline order. The stress relaxation in the various phases is discussed.

In [177] the behavior of a suspension of active polar particles under shear was analyzed. An extremely rich variety of phenomena was found, including the effective reduction or increase of the apparent viscosity predicted by Hatawlne, depending on the nature of the active stresses and the flow-alignment properties of active particles. The analytical treatment of the linear regime, where the stress-strain relation is linear, demonstrates that activity lowers the linear viscosity of both extensile, rod-shaped particle and contractile, disk-shaped particle suspensions, while it increases the viscosity of contractile, rod-shaped particle and extensile, disc-like particle suspensions. Increasing activity the rheological response becomes on linear. In this regime both stability analysis and numerical integration of the equations of motion, suggest, depending on the value of activity and strain rate, the possibility of more exotic scenarios including non-monotonic stress-strain behavior, hysteresis, yield-stress behavior and a superfluid phase with vanishing viscosity. The linear viscoelastic properties of an active suspension can be derived applying spatially uniform oscillatory shear flow at frequency ω in the $x-y$ plane obtaining, at linear order in the fields, the $x-y$ component of the stress tensor [3]

$$\sigma_{xy} = \left[\eta + \frac{(\alpha_Q - \zeta\Delta\mu)\,\xi}{-i\omega + \tau_Q^{-1}}\right] v_{xy} \ , \tag{108}$$

with $v_{x,y} = \frac{1}{2}(\partial_x v_y + \partial_y v_x)$, $\tau_Q \sim 1/\alpha_Q$ relaxation time of the order parameter and η viscosity of the suspending medium. We see that viscosity, which is obtained taking the limit $\omega \to 0$, can be either enhanced or reduced depending on the sign of ζ, giving rise to shear thickening or thinning respectively. In addition nothing rules out a negative viscosity [3].

Lattice Boltzmann methods have been used to confirm numerically most of the theoretical and experimental predictions on the rheological properties of active suspensions, and in particular to spot out the role of hydrodynamics. We will now review some of the numerical work done with LB.

Cates et al. [178] studied, by the already cited hybrid LBM the rheological the properties of a slab of active gel close to the isotropic-nematic(I/N) transition. For contractile gels and free-boundary conditions, they found a divergence of the apparent viscosity at the I-N spinodal. Extensile gels, in contrast, enter a zero-viscosity phase of N/N shear bands as the spinodal is approached. In the nonlinear regime, both extensile and contractile materials show nonmonotonic effective flow curves, with details strongly dependent on initial and boundary conditions. Finally, extensile (contractile) activity stabilizes (sup-presses) I/N shear banding.

In [67] a 2D extensile nematic gel was studied in more detail, comparing results between planar anchoring(*fixed boundary conditions*) and the case in which the director is free to rotate at the boundary planes(*free boundary conditions*). In the case of free boundary conditions, at low

activity, the static roll pattern observed in confined gels without shear is destroyed even at low shear rates, while at high shear rates a homogeneous flow is recovered. The flow pattern at very low shear rates is unsteady and is spatially nonuniform. In this case the shear stress take both positive and negative values. Enlarging activity the system displayed a clear evidence of a finite viscosity at low shear rates, while at high shear rates the laminar flow is again reestablished. For very high activity the chaotic patterns observed without applied shear are only slightly perturbed at small strain rates, with the appearance of a noticeable upward curvature in the flow curve (stress σ over shear rate $\dot{\gamma}$). In the case of fixed boundary conditions, at low activity and shear rates the flow curves display a linear regime, while for high shear rates or high activity the results are in line with previous case.

Foffano et al. [14] attempted to link micro and macrorheology of active nematics. To do so they compared macroscopic shear numerical experiments with the results of simulations where a spherical probe particle was dragged through the active fluid. The bulk rheology shows that in sheared nematics the effective viscosity differs for different anchoring conditions at the container walls given the anisotropic nature of the fluid. They also addressed the question of the role played by the anchoring conditions on the walls and by the system size L. To do so they considered both normal anchoring and planar anchoring at the walls. They found that the effective viscosity increases with L in contractile active fluids and decreases with L in extensile ones. Normal anchoring also enhances the apparent viscosity.

When a spherical particle is dragged through the active fluid, the drag force does not depend linearly on the probe radius, violating the Stokes law. When the director field is anchored tangentially to the particle surface contractility increases the drag, while extensile activity reduces it in line with the macrorheology results. In the case of normal anchoring at the probe surface, pulling orthogonally to the far-field director leads to results similar to the tangential anchoring, while dragging the particle along the director leads the particle to move faster in the contractile neamatics than it does in extensile nematics.

7 Active turbulence

Spontaneous flow in active suspensions evolves, for sufficient strength of the active component, into complex patterns for the velocity field that, at qualitative level, look chaotic resembling those of simple fluids in the passage from laminar to turbulent behavior, as suggested by streamlines of the velocity field in Fig. 3. This observation, as mentioned in the introduction, first came from experiments conducted on highly concentrated bacterial suspensions, where the velocity field was found to develop coherent vortical structures as well as jets at high velocities [10,179,180]. Transient jet-like fluid motion was found [10] with the speed of the jets $> 100\mu m/s$ significantly larger than the speed of an individual bacterium ($\sim 10\mu m/s$). The fluid pattern observed on length scales of 100-200 mm is reminiscent of a von Karman vortex street, which arises in fluids when the Reynolds number is much larger (~ 50) than that of a single bacterium cell ($\sim 10^{-4}$). This justifies the terms *bacterial turbulence* and *active turbulence*, used to denote this kind of flow [10]. Similar behaviors have been also reported in experiments on suspensions of both puller and pushers bacteria [10, 181, 182], as well microtubules bundles [73] or acto-myosin systems and microalgae [183].

A theoretical description of this complex behavior was first presented by a phenomenological model based on the Stokes equations, adapted to take into account the swimming mechanism of bacteria, each acting as a dipole stress on the fluid [184]. This model, solving the equations in two dimensions using realistic parameters, empirically reproduces the observed velocity fields.

The first attempt of a quantitative analysis of turbulent behavior was first done by Wensink *et al.* in [68], with a combination of experiments, simulations of self-propelled rods (SPR) and continuum theory aimed at identifying the statistical properties of self-sustained mesoscale turbulence in dense suspensions of Bacillus subtilis. Experimental and numerical data coming from SPR simulations for the energy spectrum, exhibit power law scaling regimes better observed in two dimensions for both small ($k^{5/3}$) and large ($k^{-8/3}$) wave numbers; however the power-law exponents differ from the characteristic $k^{-5/3}$ decay of $2d$ high Reynolds numbers turbulence, as it will be discussed later. Similar results were also found making use of the continuum theory of Toner and Tu [185], supplemented with the Swift-Honenberg stress tensor presented in Eq.(8), containing higher order derivatives of the velocity gradient. Experimental data in $3d$ look qualitatively similar but show an intermediate plateau region not present in two-dimensional systems, to indicate the spreading of kinetic energy over a wider range of scales. The same model was used in a subsequent paper [11] to consistently reproduce velocity statistics and correlations in a highly concentrated $3d$ suspension of B.subtilis, while in [104] the linear stability analysis was presented.

Beside bacteria, eukariotic cells with self-motile properties also show self-sustained flows. In [69] a suspension of spermatozoa was found to develop a directed energy cascade characterized by a power scaling law k^{-3} at high wave numbers, a behavior that is found in quasi-$2d$ turbulent flows. Recently, active turbulence features were also found in a system of self-assembled ferromagnetic Nickel microparticles dispersed at the water-air interface, while subjected to an external oscillating magnetic field [186]. Self-assembled spinners locally inject energy in the solvent via generation of local vortex flows, thus leading to the subsequent energy cascade towards larger scales. The hydrodynamic state is characterized by a power-law decay $k^{-5/3}$ of the energy spectrum at low packing fractions, but when this increases, steric and magnetic interactions become important so that even the the exponent start to deviate while the system undergoes a transition toward a new phase where spinners are replaced by non-rotating clusters. The experimental observation were qual-

itatively reinforced through numerical simulations of discs suspended in $2d$ geometries whose dynamics was solved using the Multi-Particle-Collision approach.

The model of Wensink *et al.* [68], previously discussed, has the advantage of simplicity with respect to the active gel theory of sect 2.5. In that model the scale of variation for the velocity field is set phenomenologically, by varying the ratio between coefficient in (8), thus the explicit dynamics of the active components is neglected, so that one cannot derive any information on the relations between the velocity, the active component fluctuations, and the order parameter patterns with its inherent defect dynamics. A more complete analysis of these features can be performed by considering the nematic gel theory of Section 2.5 as first done in [187]. Here decay spectra for kinetic energy and enstrophy were calculated for a quite small $2d$ system with periodic boundary conditions. Always using finite differences methods to solve the Beris-Edwards and the Navier-Stokes equations of Section 2.5, Giomi carefully analyzed the statistics of vortices in [188], finding that their areas are exponentially distributed and giving insights into the relations between the topological properties of the nematic director and the geometry of the flow. In particular he found that the chaotic regime is due to a feedback mechanism between the advection of nematic $\pm 1/2$ disclinations and vortical flows, whose structure is in turn closely related to presence of disclinations in their neighborhood, as demonstrated in refs. [85,189]. The number of both $+1/2$ disclinations and vortices is found to be linearly proportional to the strength of the active injection, while creating and annihilation rates of oppositely charged defects exhibit a quadratic dependence. Moreover, not only the statistics but also the disclination dynamics is highly dominated by vortical flows: indeed defects are found to be transported by the fluid along the edge of vortices at an angular velocity that is again linearly dependent from activity. As a consequence the annihilation lifetime of disclinations is inversely proportional to the angular velocity hence, to the active parameter. The energy and enstrophy spectra were respectively observed to decay as k^{-4} and k^{-2}, in the limit of high wave numbers, with no significant dependence neither on the value nor on the kind of activity (extensile or contractile).

The importance of relations between defects and vorticity has also been highlighted in ref. [70] where a phenomenological continuum theory for overdamped active nematic liquid crystals is introduced. Three different non-equilibrium steady states are found according to the mutual effects of active torques and active convection: when the first is dominant over the second a defect order nematic is developed, where the comet tail of $+1/2$ disclinations are aligned throughout the system; when instead active convection dominates over torques an undulated nematic free-of-defect state is formed. Nevertheless when these contributions are equally important a turbulent nematic state emerges, being characterised by a sharp increase both in vorticity and in the number of defects.

The growing interest in active turbulence over the last decade is motivated by some peculiar aspects: firstly fluid active systems mostly evolve in the low Reynolds number regime, so that the development of a turbulent state is highly surprising, secondly the search for an universality class for this phenomena is extremely challenging, due to the breadth of the actual scenario. Moreover even the physical mechanism that drives active systems toward the turbulent state is remarkable: energy injection takes place on small scales l of the same order of the length of microswimmers, setting an upper bound for the spectral range of energy injection $k_l \sim 2\pi/l$, while the typical wavenumbers k over which the turbulent flows take place, namely those regions where energy spectra exhibit power-law decay, are such that $k/k_l < 1$. Hence, energy, that has been injected by the active components on micro scales, is transported on much bigger scales, through complex hydrodynamics mechanisms. This is somehow reminescent of two-dimensional classical turbulence in which energy pumped into the system by an external force at a certain scale l_f is not dissipated by viscosity, but tranferred to larger scales giving rise to an *inverse energy cascade* [190]. By requiring a scale independent energy-flux, one finds the Kolmogorov solution for the energy spectra $\sim k^{-5/3}$, in the inertial range $k \ll k_f = 2\pi/l_f$. Yet another inertial region is expected in the direct-cascade range $k \gg k_f$, where the requirement of constant enstrophy flux gives a solution for the spectrum $\sim k^{-3}$.

In spite of the effort taken up to now, a complete characterization for the variety of behaviors observed in the scope of bacterial turbulence is still lacking. Indeed beside the qualitative similarity between bacterial and classical turbulent flows, it is evident, from the wide phenomenology presented before, that arguments valid for the classical high-Re turbulence do not hold for active matter systems, because of the plurality of behaviors observed, nor any alternative theory has already been able to fully provide a consistent explanation of such phenomena.

An insight into the mechanism due to energy injection and dissipation has been outlined by Bratanov *et al.* in [191]. In this work the spectral properties of the same model as in [68] are analyzed. They found a power-law energy spectrum at large scales, even in absence of an inertial range, namely a region of constant energy flux. Moreover the exponents are not universal but they depend on the energy parameters and exhibit system size dependence. They notice that the presence of further non-linearities introduced in the model, with respect to the only advective term in the Navier-Stokes equation (13), provides additional freedom to the energy exchange between different scales, leading to the scale-by-scale balance between linear forcing and energy consuming terms and non linear terms.

Recently a connection between bacterial and classical turbulence has been established by Doostmohammadi *et al.* in [192] and by Shendruk *et al.* [193] , where continuum equations for the active nematic theory of Section 2.2 were solved through a hybrid lattice Boltzmann method. Shendruk found that by confining active nematics in a microchannel, the system exhibits various morphological behaviors in dependence of the intensity of active doping; for small activities they found an unidirectional spontaneous

flow regime, followed by an oscillating laminar flowing state, that becomes turbulent for enough intense values of the activity parameter. One of the results presented in this work is the appearence of an intermediate state between the laminar regime and the turbulent one, addressed as *Ceilidh dance*. This represents the motion of paired disclinations in the nematic pattern moving along the channel, that, advected by the vortical flow, exchange partners, producing a dynamical ordered state that is reminescent of Ceilidh dancing. The transition to the turbulent state is fully analyzed in the work of Doostmohammadi: here vorticity puffs are used to characterize the transition. Unlike the inertial puffs that drive high-Re systems toward a full turbulent state and are initiated by external forcings, in this case these are driven by the internal injection of energy on small scales. Far from the turbulent transition, the turbulent fraction, namely the area fraction occupied by the active puffs, is almost null, since they often vanish before splitting, but when the active doping becomes more intense while approaching the turbulent threshold, their lifetime grows and splitting becomes more likely. When the turbulent threshold is exceeded the turbulent fraction grows with a power-law $\sim (A - A_{cr})^{0.275\pm0.043}$, where the adimensional active number $A = \sqrt{\zeta h^2/K}$, being h the channel width and A_{cr} the turbulent threshold. The exponent characterizing the transition closey matches the universal critical exponent of the $(1 + 1)$ directed percolation ($\beta = 0.276$). Moreover this is in turn very close to the exponent measured in Couette flows for inertial turbulence [194] (since in that case $\beta = 0.28 \pm 0.03$).

The works of Shendruk and Doostmohammadi had so shed light on the route to follow to fully charachterize the turbulent behavior, but still a number of questions has to be answered: which mechanism drives the system towards the turbulent state? How energy is exchanged between different lengthscales? Is it possible to confine and tune the turbulent behavior? These questions have still to be answered and are still open to firther research.

8 Colloids

In this last section we briefly review the simulation studies investigating the physics of particle suspensions (such as colloids) dispersed in a fluid, in the context of active matter and performed via Lattice Boltzmann methods. The systems studied so far can be divided in two broad classes. The first one, on which large part of the recent research has been addressed, encompasses those made up of active particles dispersed in a passive fluid, while the second one, whose physcics remains still largely unexplored, includes those in which passive particles are dispersed in an active medium.

In recent years several models, pertaining to the first group, have been proposed to simulate microscopic swimmers interacting with a fluid at low Reynolds number. Ramachandran *et al.* [195], for instance, described a swimmer by extending the method introduced by Ladd [140, 196, 197] to model solid passive particles to the active ones. This is done by adding an active force distributed at the boundary between the fluid and a solid particle, where stick boundary conditions, bouncing back the incoming fluid at the particle surface, are implemented. Particle's self-propulsion is triggered when an asymmetric force distribution is applied, while a symmetric one only perturbs the fluid in the surrounding of the particle without generating any net motion. The former case describes the movers (or polar particles) while the latter one the shakers (or apolar particles). A complementary mechanism promoting particle's self-propulsion was proposed in Ref. [198], and consisted in adding a constant amount of momentum with fixed magnitude to the particle, and then, to restore momentum conservation, to subtract the same amount to the fluid nodes connected to the solid ones. This approach has been used to study the collective dynamics of self-propelled particles dispersed in a fluid solvent, and was found to reproduce, for instance, the formation of transient particles' aggregates as well as the transition of the particle mean square displacement from diffusive towards ballistic motion at low concentration [199]. A similar mechanism has been also used to investigate the hydrodynamics of active rotators [200], systems capturing, for example, the rotating motion of molecular motors on the cell membrane [201].

An alternative approach has been afterwards used to simulate suspensions of swimming particles (again built using the Ladd method) starting from the squirmer model introduced by Lighthill [202, 203], in which particle's motion is triggered by a predefined axisymmetric tangential velocity distribution imposed on the surface of the particle. By using such velocity distribution as boundary condition of the Stokes and the continuity equations (as the inertia of the fluid is neglected), the mean fluid flow induced by a minimal squirmer can be computed

$$u(\theta) = B_1 \sin(\theta) + \frac{B_2}{2} \sin(2\theta), \tag{109}$$

where only the first two terms of an expansion with Legendre polynomials have been kept on the right hand side of Eq. (109). Here θ is a polar angle and $\theta = 0$ defines the swimming direction of the squirmers. The dimensionless parameter $\epsilon = B_2/B_1$ defines the type of squirmer: $\epsilon > 0$ describes a puller (or contractile squirmer) while $\epsilon < 0$ describes a pusher (or extensile squirmer). The case with $\epsilon = 0$ corresponds to an apolar squirmer (or shaker).

Lattice Boltzmann has been also proven to be a powerful method to investigate the hydrodynamics of active three-bead linear swimmers [204], a system in which an analytic solution is available [205]. Here the swimmer is constituted of three spheres of predefined radius linked with sufficiently thin rods to neglect hydrodynamic interactions. Lengths and angles between the rods can be modified in a periodic and time irreversible manner by the action of internal forces and torques, which favour change in the swimmer shape and potentially motion when coupled to the fluid. Unlike the Ladd approach, in this model there is no net interface separating the fluid from the bead, whose interior is then essentially fluid. Although less realistic, this condition is acceptable as intertial effects are

negligible. The swimmer-fluid interaction is incorporated through three steps, the first of which computes the total linear and angular momenta of the swimmer. Afterwards position and shape of the swimmer are updated with respect to the original one (such that linear and angular momentum are conserved) and finally the motion of the swimmer is coupled to the fluid to obtain updated fluid velocities used to calculate the equilibrium distribution functions of the LBM [71, 204]. Such approach was found to reproduce analytical results with sufficient accuracy, in particular when swimmers with a high number of beads (even more than three) and close to each other or near a surface are considered, although with less computational efficiency than other methods (such as the Oseen tensor approach) due to the increasing of lattice resolution [204]. An alternative and computationally simpler way to model solid object on a grid was suggested by Smith and Denniston [206]. Here the surface of the swimmer is represented by a large number of point particles, which ensure a non-slip condition by introducing a drag force between the particles and the nodes of the lattice Boltzmann mesh [71]. Although this method was found efficient in simulating the swimming velocity of a single swimmer, it suffered of large discretization errors affecting inter-swimmer hydrodynamic interactions.

Due to a limited computational efficiency, the models described so far have been rarely applied to simulate highly anisotropic particles. This drawback has been recently circumvented by de Graaf et al. [207, 208], that modeled active colloids of arbitrary shape as clusters of spheres coupled to the LB fluid through the scheme introduced by Ahlrichs and Düenweg [209]. Unlike the Ladd method, in this approach particles are described as points coupled to the fluid through a frictional force, acting both on the solvent and on the solute, which depends on the relative velocity. When a high enough number of points is coupled to the fluid, the LB fluid inside the particle co-moves with the coupling points and models a hydrodynamically solid object [210,211]. Self-propulsion is achieved by means of a persistence force applied along a direction vector assigned to the particle, while an equal and opposite counter force is applied to the fluid [212–214]. Its location sets the nature of the swimmer (whether contractile or extensile) and the structure of the fluid flow in its surrounding. Besides being a facile approach, this method has the advantage to incorporate hydrodynamic interactions with higher order multipole moments, in addition to the usual dipole ones, and to well reproduce far-field theoretical results in system with periodic boundary conditions and in a spherical cavity with no-slip walls [215]. A likewise computationally efficient method, in which swimmers are described using the point-force implementation developed by Nash *et al.* [212], has been used to perform unprecedented large-scale LB simulations of $\sim 10^6$ hydrodynamically interacting swimmers in a cubic box with periodic boundary conditions [216]. In this work the authors show that swimmers move in a correlated fashion well below the transition to the bacterial turbulence, and elaborated a novel kinetic approach capturing such behavior with results in quantitative agreement with LB simulations.

More recently Lattice Boltzmann methods have been extended to simulate more complicated physical systems in which active particles play once more a relevant role. A remarkable example is the process of cross-streamline migration (often called margination [217]) of stiff active particles (such as synthetic nanoparticles used for drug-delivery) in blood flows, studied in Ref. [218]. Such phenomenon is attributed to hydrodynamic interaction of red blod cells with stiff particles, and disappears when red blood cells are absent. Active particles are modeled by triangulated spheres whose internal grid nodes are massless points flowing with the local fluid velocity and connected each other through stiff harmonic springs and bending potential to preserve the grid arrangement. This approach is often referred as immersed boundary method [219,220]. A force is then applied to the center of mass of the particles (which become active) and along the opposite direction with respect to the fluid flow.

A much less investigated system is that in which a passive particle is embedded in active fluid. This has been done in Ref. [14, 15], where LB simulations show a violation of the Stokes' law when a particle (modeled by using the Ladd's method) is dragged in an active fluid and, even more strikingly, a negative viscous drag in the steady state of a contractile fluid for large enough particles. Such simulated microreological experiment, in principle realizable in the laboratory, highlights the fact that, although at its infancy, the study of these systems may unveil novel and intriguing physics, potentially useful for the design of novel active soft materials.

Clearly many efforts have been addressed to model systems which (i) correctly describe the hydrodynamics of active particles and (ii) capture new dynamical and mechanical properties of great importance for future practical applications. Several directions of research can be envisaged starting from the results achieved so far. A largely unexplored field is that of the active rheology, in which suspensions of particles (e.g. passive) are subject to an external perturbation (such as a shear flow) in an active liquid crystal. Here the nature of the active system (either contractile or extensile) as well as the particle volume fraction and the shear stress may dramatically affect the rheological response. In addition the presence of topological defects, due to the conflict anchoring of the liquid crystal with that on particle's surface, may foster the formation of turbulent-like velocity patterns, whose physics is still under investigation. LB simulations performed so far usually neglect thermal fluctuations, which may however be crucial especially when the particle's size decreases up to nanometers. Even more intriguing seems the possibility of a multiscale coupling of the LB with other simultation methods, such as dissipative particle dynamics or immersed boundary method, to capture, for instance, the near-contact interaction of active colloids at the interface of a binary fluid.

References

1. J. Toner, Y. Tu, and S. Ramaswamy. Hydrodynamics and phases of flocks. *Ann. Phys.*, 318:170, 2005.
2. S. Ramaswamy. The mechanics and statistics of active matter. *Annu. Rev. Condens. Matter Phys.*, 1:323, 08 2010.
3. M.C. Marchetti, J.F. Joanny, S. Ramaswamy, T.B. Liverpool, J.J. Prost, M. Rao, and R.A. Simha. Hydrodynamics of soft active matter. *Rev. Mod. Phys.*, 85:1143, 7 2013.
4. J. Elgeti, R.G. Winkler, and G. Gompper. Physics of microswimmerssingle particle motion and collective behavior: a review. *Rep. Prog. Phys.*, 78:056601, 05 2015.
5. G. Gonnella, D. Marenduzzo, A. Suma, and A. Tiribocchi. Motility-induced phase separation and coarsening in active matter. *C. R. Phys.*, 16:316, 04 2015.
6. C. Bechinger, R. Di Leonardo, H. Löwen, C. Reichhardt, G. Volpe, and G. Volpe. Active particles in complex and crowded environments. *Rev. Mod. Phys.*, 88:045006, 2016.
7. T. Surrey, F. Nédélec, S. Leibler, and E. Karsenti. Physical properties determining self-organization of motors and microtubules. *Science*, 292:1167, 5 2001.
8. P.M. Bendix, G.H. Koenderink, D. Cuvelier, Z. Dogic, B.N. Koeleman, W.M. Brieher, C.M. Field, L. Mahadevan, and D.A. Weitz. A quantitative analysis of contractility in active cytoskeletal protein networks. *Biophys. J.*, 94:117960, 04 2008.
9. J. Howard. Mechanics of motor proteins and the cytoskeleton. *BioEssays*, 25, 2003.
10. C. Dombrowski, L. Cisneros, S. Chatkaew, R.E. Goldstein, and J.O. Kessler. Self-concentration and large-scale coherence in bacterial dynamics. *Phys. Rev. Lett.*, 93:098103, 8 2004.
11. J. Dunkel, S. Heidenreich, K. Drescher, H. H. Wensink, M. Bär, and Raymond E. Goldstein. Fluid dynamics of bacterial turbulence. *Phys. Rev. Lett.*, 110:228102, May 2013.
12. Y. Hatwalne, S. Ramaswamy, M. Rao, and R.A. Simha. Rheology of active-particle suspensions. *Phys. Rev. Lett.*, 92:118101, 3 2004.
13. D. Marenduzzo, E. Orlandini, M.E. Cates, and J.M. Yeomans. Steady-state hydrodynamic instabilities of active liquid crystals: Hybrid lattice boltzmann simulations. *Phys. Rev. E*, 76:031921, Sep 2007.
14. G. Foffano, J.S. Lintuvuori, A.N. Morozov, K. Stratford, M.E. Cates, and D. Marenduzzo. Bulk rheology and microrheology of active fluids. *Eur. Phys. J. E*, 35:98, 10 2012.
15. G. Foffano, J.S. Lintuvuori, K. Stratford, M.E. Cates, and D. Marenduzzo. Colloids in active fluids: Anomalous microrheology and negative drag. *Phys. Rev. Lett.*, 109:028103, 2012.
16. A. Sokolov and I.S. Aranson. Reduction of viscosity in suspension of swimming bacteria. *Phys. Rev. Lett.*, 103:148101, 9 2009.
17. M.E. Cates, S.M. Fielding, D. Marenduzzo, E. Orlandini, and J.M. Yeomans. Shearing active gels close to the isotropic-nematic transition. *Phys. Rev. Lett.*, 101:068102, 8 2008.
18. R.A. Simha and S. Ramaswamy. Hydrodynamic fluctuations and instabilities in ordered suspensions of self-propelled particles. *Phys. Rev. Lett.*, 89:058101, 7 2002.
19. H. Chaté, F. Ginelli, and R. Montagne. Simple model for active nematics: Quasi-long-range order and giant fluctuations. *Phys. Rev. Lett.*, 96:180602, 5 2006.
20. V. Narayan, S. Ramaswamy, and N. Menon. Long-lived giant number fluctuations in a swarming granular nematic. *Science*, 317:105, 7 2007.
21. J. Deseigne, O. Dauchot, and H. Chaté. Collective motion of vibrated polar disks. *Phys. Rev. Lett.*, 105:098001, 8 2010.
22. N. Kumar, S. Ramaswamy, and A.K. Sood. Symmetry properties of the large-deviation function of the velocity of a self-propelled polar particle. *Phys. Rev. Lett.*, 106:118001, 3 2011.
23. F. Cagnetta, F. Corberi, G. Gonnella, and A. Suma. Large fluctuations and dynamic phase transition in a system of self-propelled particles. *Phys. Rev. Lett.*, 119:158002, 10 2017.
24. C. Bechinger, R. Di Leonardo, H. Löwen, and C. Reichhardt G. Volpe. Active particles in complex and crowded environments. *Rev. Mod. Phys*, 88:045006, 2016.
25. A. Cavagna and I. Giardina. Bird flocks as condensed matter. *Annu. Rev. Condens. Matter Phys.*, 5(1):183, 2014.
26. T. Vicsek, A. Czirk, E. Ben-Jacob, I. Cohen, and O. Shochet. Novel type of phase transition in a system of self-driven particles. *Phys. Rev. Lett.*, 75:1226, 8 1995.
27. M.E. Cates and J. Tailleur. Motility-induced phase separation. *Annu. Rev. Condens. Matter Phys.*, 6:219–244, 03 2015.
28. F. Peruani, A. Deutsch, and M. Bär. Nonequilibrium clustering of self-propelled rods. *Phys. Rev. E*, 74:030904, 9 2006.
29. A. Baskaran and M.C. Marchetti. Enhanced diffusion and ordering of self-propelled rods. *Phys. Rev. Lett.*, 101:268101, 12 2008.
30. Y. Yang, V. Marceau, and G. Gompper. Swarm behavior of self-propelled rods and swimming flagella. *Phys. Rev. E*, 82:031904, 2010.
31. Y. Fily and M.C. Marchetti. Athermal phase separation of self-propelled particles with no alignment. *Phys. Rev. Lett.*, 108:235702, 6 2012.
32. I. Buttinoni, J. Bialké, F. Kümmel, H. Löwen, C. Bechinger, and T. Speck. Dynamical clustering and phase separation in suspensions of self-propelled colloidal particles. *Phys. Rev. Lett.*, 110:238301, 6 2013.
33. G.S. Redner, M.F. Hagan, and A. Baskaran. Structure and dynamics of a phase-separating active colloidal fluid. *Phys. Rev. Lett.*, 110:055701, 1 2013.
34. L.F. Cugliandolo, P. Digregorio, G. Gonnella, and A. Suma. Phase coexistence in two-dimensional passive and active dumbbell systems. *Phys. Rev. Lett.*, 119:268002, 9 2017.
35. P. Digregorio, D. Levis, A. Suma, L.F. Cugliandolo, G. Gonnella, and I. Pagonabarraga. Full phase diagram of active brownian disks: from melting to motility-induced phase separation. *preprint*.
36. F. Nédélec, T. Surrey, A.C. Maggs, and S. Leibler. Self-organization of microtubules and motors. *Nature*, 389:305, 9 1997.
37. J. Toner and Y. Tu. Long-range order in a two-dimensional dynamical xy model: How birds fly together. *Phys. Rev. Lett.*, 75:4326, 12 1995.

38. H. Gruler, U. Dewald, and M. Eberhardt. Nematic liquid crystals formed by living amoeboid cells. *Eur. Phys. J. B*, 11:187, 09 1999.
39. S. Ramaswamy, R.A. Simha, and J. Toner. Active nematics on a substrate: Giant number fluctuations and long-time tails. *E.P.L.*, 62:196, 04 2003.
40. A. Baskaran and M.C. Marchetti. Nonequilibrium statistical mechanics of self-propelled hard rods. *J. Stat. Mech. Theory Exp.*, 2010:04019, 04 2010.
41. V. Shaller, C. Weber, C. Semmrich, E. Frey, and A.R. Bausch. Polar patterns of driven filaments. *Nature*, 467:73, 2010.
42. K. Kruse, J.F. Joanny, F. Jülicher, J. Prost, and K. Sekimoto. Asters, vortices, and rotating spirals in active gels of polar filaments. *Phys. Rev. Lett.*, 92:078101, 2 2004.
43. F. Jülicher, K. Kruse, J. Prost, and J.F. Joanny. Active behavior of the cytoskeleton. *Phys. Rep.*, 449:3, 2007.
44. M.R. Swift, E. Orlandini, W.R. Osborn, and J.M Yeomans. Lattice boltzmann simulations of liquid-gas and binary fluid systems. *Phys. Rev. E*, 54:5041, Nov 1996.
45. G. Gonnella, E. Orlandini, and J.M. Yeomans. Spinodal decomposition to a lamellar phase: Effects of hydrodynamic flow. *Phys. Rev. Lett.*, 78:1695, 3 1997.
46. A. Lamura, G. Gonnella, and J.M. Yeomans. A lattice boltzmann model of ternary fluid mixtures. *E.P.L.*, 45(3):314, 1999.
47. J.M. Yeomans and G. Gonnella. *Kinetics of Phase Transitions*. 03 2009.
48. A. Tiribocchi, N. Stella, G. Gonnella, and A. Lamura. Hybrid lattice boltzmann model for binary fluid mixtures. *Phys. Rev. E*, 80:026701, 8 2009.
49. C. Denniston, E. Orlandini, and J.M. Yeomans. Lattice boltzmann simulations of liquid crystal hydrodynamics. *Phys. Rev. E*, 63:056702, Apr 2001.
50. S. Succi. *The Lattice Boltzmann Equation: For Fluid Dynamics and Beyond*. Numerical Mathematics and Scientific Computation. Clarendon Press, 2001.
51. F.M. Leslie. Some constitutive equations for liquid crystals. *Arch. Ration. Mech. Anal.*, 28(4):265, 01 1968.
52. P.C. Martin, O. Parodi, and P.S. Pershan. Unified hydrodynamic theory for crystals, liquid crystals, and normal fluids. *Phys. Rev. A*, 6:2401, Dec 1972.
53. A.N. Beris and B.J. Edwards. *Thermodynamics of Flowing Systems*. Oxford Engineering Science Series. Oxford University Press, 1994.
54. E. Orlandini, M.E. Cates, D. Marenduzzo, L. Tubiana, and J.M. Yeomans. Hydrodynamic of active liquid crystals: A hybrid lattice boltzmann approach. *Mol. Cryst. Liq. Cryst.*, 494:293, 12 2008.
55. G.R McNamara and G. Zanetti. Use of the boltzmann equation to simulate lattice-gas automata. *Phys. Rev. Lett.*, 61:2332, Nov 1988.
56. F.J. Higuera, S. Succi, and R. Benzi. Lattice gas dynamics with enhanced collisions. *E.P.L.*, 9(4):345, 1989.
57. H. Chen, S. Chen, and W.H. Matthaeus. Recovery of the navier-stokes equations using a lattice-gas boltzmann method. *Phys. Rev. A*, 45:R5339–R5342, Apr 1992.
58. S. Succi. *The Lattice Boltzmann Equation: For Complex States of Flowing Matter*. Oxford University Press, 2018.
59. M.R. Swift, W.R. Osborn, and J.M. Yeomans. Lattice boltzmann simulation of nonideal fluids. *Phys. Rev. Lett.*, 75:830, Jul 1995.
60. Q. Li, K.H. Luo, and X.J. Li. Forcing scheme in pseudopotential lattice boltzmann model for multiphase flows. *Phys. Rev. E*, 86:016709, Jul 2012.
61. X. Shan and H. Chen. Lattice boltzmann model for simulating flows with multiple phases and components. *Phys. Rev. E*, 47:1815, Mar 1993.
62. M. E. Cates, O. Henrich, D. Marenduzzo, and K. Stratford. Lattice boltzmann simulations of liquid crystalline fluids: active gels and blue phases. *Soft Matter*, 5:3791–3800, 2009.
63. R. Voituriez, J.F. Joanny, and J. Prost. Spontaneous flow transition in active polar gels. *E.P.L.*, 70:404, 05 2005.
64. D. Marenduzzo and E. Orlandini. Hydrodynamics of nonhomogeneous active gels. *Soft Matter*, 6(4):774, 2010.
65. E. Tjhung, D. Marenduzzo, and M.E. Cates. Spontaneous symmetry breaking in active droplets provides a generic route to motility. *Proc. Natl. Acad. Sci. U.S.A.*, 109(31):12381–12386, 2012.
66. E. Tjhung, A. Tiribocchi, D. Marenduzzo, and M. E. Cates. A minimal physical model captures the shapes of crawling cells. *Nat. Comm.*, 6:5420, 2015.
67. S. M. Fielding, D. Marenduzzo, and M. E. Cates. Nonlinear dynamics and rheology of active fluids: Simulations in two dimensions. *Phys. Rev. E*, 83:041910, Apr 2011.
68. H.H. Wensink, J. Dunkel, S. Heidenreich, K. Drescher, H. Lowen R.E. Goldstein, and J.M. Yeomans. Meso-scale turbulence in living fluids. *Proceedings of the National Academy of Sciences*, 109, 09 2012.
69. A. Creppy, O. Praud, X. Druart, P.L. Kohnke, and F. Plouraboué. Turbulence of swarming sperm. *Phys. Rev. E*, 92:032722, Sep 2015.
70. E. Putzig, G.S. Redner, A. Baskaran, and A. Baskaran. Instabilities, defects, and defect ordering in an overdamped active nematic. *Soft Matter*, 12:3854–3859, 2016.
71. C.M. Pooley and J.M. Yeomans. Lattice boltzmann simulation techniques for simulating microscopic swimmers. *Comput. Phys. Commun.*, 179(1):159, 2008. Special issue based on the Conference on Computational Physics 2007.
72. J. Schwarz-Linek, C. Valeriani, A. Cacciuto, M.E. Cates, D. Marenduzzo, A.N. Morozov, and W.C.K. Poon. Phase separation and rotor self-assembly in active particle suspensions. *Proc. Natl. Acad. Sci. USA*, 109(11):4052, 2012.
73. T. Sanchez, D.T.N. Chen, S.J. Decamp, M. Heymann, and Z. Dogic. Spontaneous motion in hierarchically assembled active matter. 491:431–434, 11 2012.
74. P. Guillamat, J. Ignés-Mullol, and F. Sagués. Control of active liquid crystals with a magnetic field. *Proc. Natl. Acad. Sci. USA*, 113(20):5498, 2016.
75. A. Tiribocchi, R. Wittkowski, D. Marenduzzo, and M.E. Cates. Active model h: Scalar active matter in a momentum-conserving fluid. *Phys. Rev. Lett.*, 115:188302, Oct 2015.
76. D. Bray. *Cell Movements: From Molecules to Motility, 2nd Edition*. Garland Publishing, 2000.
77. E. Tjhung, M.E. Cates, and D. Marenduzzo. Nonequilibrium steady states in polar active fluids. *Soft Matter*, 7:7453–7464, 2011.
78. E. Tjhung, A. Tiribocchi, D. Marenduzzo, and M.E. Cates. A minimal physical model captures the shapes of crawling cells. *Nat.Commun.*, 6:5420, 2015.
79. S.J. DeCamp, G.S. Redner, A. Baskaran, M.F. Hagan, and Z. Dogic. Orientational order of motile defects in active nematics. *Nat. Mater.*, 14:11110, 2015.

80. R. Kemkemer, D. Kling, D. Kaufmann, and H. Gruler. Elastic properties of nematoid arrangements formed by amoeboid cells. *Eur. Phys. J. E*, 1(2):215, 2000.
81. G. Duclos, S. Garcia, H.G. Yevick, and P. Silberzan. Perfect nematic order in confined monolayers of spindle-shaped cells. *Soft Matter*, 10:2346, 2014.
82. I. Petrelli, P. Digregorio, L.F. Cugliandolo, G. Gonnella, and A. Suma. Active dumbbells: dynamics and morphology in the coexisting region. *arXiv:1805.06683v1[cond-mat.stat-mech]*, 2018.
83. P.G. de Gennes and J. Prost. *The physics of liquid crystals*. The International series of monographs on physics 83 Oxford science publications. Oxford University Press, 2nd ed edition, 1993.
84. P.M. Chaikin and T.C. Lubensky. *Principles of condensed matter physics*, volume 10.1017/CBO9780511813467. 1995.
85. G. Tóth, C. Denniston, and J.M Yeomans. Hydrodynamics of topological defects in nematic liquid crystals. *Phys. Rev. Lett.*, 88:105504, Feb 2002.
86. Luca Giomi, Mark J. Bowick, Xu Ma, and M. Cristina Marchetti. Defect annihilation and proliferation in active nematics. *Phys. Rev. Lett.*, 110:228101, May 2013.
87. N. Schopohl and T. J. Sluckin. Defect core structure in nematic liquid crystals. *Phys. Rev. Lett.*, 59:2582–2584, Nov 1987.
88. J. Yeomans. *The hydrodynamics of active systems*. Proceedings of the International School of Physics "E. Fermi". IOS Press, 2016.
89. T.J. Pedley and J.O. Kessler. Hydrodynamic phenomena in suspensions of swimming microorganisms. *Annu. Rev. Fluid Mech.*, 24(1):313, 1992.
90. S. Zhou, A. Sokolov, O. Lavrentovich, and I.S. Aranson. Living liquid crystals. *Proceedings of the National Academy of Sciences*, 111(4):1265–1270, 2014.
91. S.R. Naganathan, S. Frthauer, M. Nishikawa, F. Jlicher, and S.W. Grill. Active torque generation by the actomyosin cell cortex drives leftright symmetry breaking. *eLife*, 3:e04165, dec 2014.
92. R.H. Depue and R.V. Rice. F-actin is a right-handed helix. *J. Mol. Biol.*, 12:302, 1965.
93. F. Livolant. Cholesteric liquid crystalline phases given by three helical biological polymers: Dna, pblg and xanthan. a comparative analysis of their textures. *J. Phys. France*, 47(1605), 1986.
94. F. Livolant. Ordered phases of dna in vivo and in vitro. *Physica A*, 176(117), 1991.
95. E. Tjhung, M.E. Cates, and D. Marenduzzo. Contractile and chiral activities codetermine the helicity of swimming droplet trajectories. *Proceedings of the National Academy of Sciences*, 114(18):4631–4636, 2017.
96. S.R. De Groot and P. Mazur. *Non-Equilibrium Thermodynamics*. Dover Books on Physics. Dover Publications, 2013.
97. S. Ramaswamy. Active matter. *Journal of Statistical Mechanics: Theory and Experiment*, 2017(5):054002, 2017.
98. G. Mazenko. *Nonequilibrium Statistical Mechanics*. Physics textbook. Wiley, 2006.
99. S. A. Brazovskiĭ. Phase transition of an isotropic system to a nonuniform state. *J. Exp. Theor. Phys.*, 41:85, 1975.
100. E. Orlandini G. Gonnella and J.M Yeomans. Lattice boltzmann simulations of lamellar and droplet phases. *Phys. Rev. E*, 58:480–485, 1998.
101. J. Swift and P.C. Hohenberg. Hydrodynamic fluctuations at the convective instability. *Phys. Rev. A*, 15:319–328, Jan 1977.
102. S. Chandrasekhar. *Hydrodynamic and Hydromagnetic Stability*. Dover Books on Physics Series. Dover Publications, 1981.
103. H. Bellout and F. Bloom. *Incompressible Bipolar and Non-Newtonian Viscous Fluid Flow*. Advances in Mathematical Fluid Mechanics. Springer International Publishing, 2013.
104. J. Dunkel, S. Heidenreich, M. Bär, and R.E. Goldstein. Minimal continuum theories of structure formation in dense active fluids. *New J. Phys.*, 15:045016, 4 2013.
105. S.R. McCandlish, A. Baskaran, and M.F. Hagan. Spontaneous segregation of self-propelled particles with different motilities. *Soft Matter*, 8(8):2527–2534, 2012.
106. A.Y. Grosberg and J.F. Joanny. Nonequilibrium statistical mechanics of mixtures of particles in contact with different thermostats. *Phys. Rev. E*, 92:032118, 2015.
107. J. Stenhammar, R. Wittkowski, D. Marenduzzo, and M.E. Cates. Activity-induced phase separation and self-assembly in mixtures of active and passive particles. *Phys. Rev. Lett.*, 114, 2015.
108. M.L Blow, S.P. Thampi, and J.M Yeomans. Biphasic, lyotropic, active nematics. *Phys. Rev. Lett.*, 113:248303, 2014.
109. L. Giomi and A. DeSimone. Spontaneous division and motility in active nematic droplets. *Phys. Rev. Lett.*, 112:147802, Apr 2014.
110. F. Bonelli, L.N. Carenza, G. Gonnella, D. Marenduzzo, E. Orlandini, and A. Tiribocchi. Lamellar ordering, droplet formation and phase inversion in exotic active emulsions. *submitted, on 16/02/2018, to ArXiv cond-mat.*, 2017.
111. P.C. Hohenberg and B.I. Halperin. Theory of dynamic critical phenomena. *Rev. Mod. Phys.*, 49:435, Jul 1977.
112. A.J. Bray. Theory of phase-ordering kinetics. *Advances in Physics*, 43(3):357–459, 1994.
113. R. Wittkowski, A. Tiribocchi, J. Stenhammar, R. J. Allen, D. Marenduzzo, and M.E. Cates. Scalar ϕ^4 field theory for active-particle phase separation. *Nat. Comm.*, 5, 2014.
114. W. Kung, M.C. Marchetti, and K. Saunders. Hydrodynamics of polar liquid crystals. *Phys. Rev. E*, 73:031708, 3 2006.
115. R. LeVeque. *Finite Difference Methods for Ordinary and Partial Differential Equations: Steady-State and Time-Dependent Problems*. Society for Industrial and Applied Mathematics, Philadelphia, PA, USA, 2007.
116. U. Frisch, B. Hasslacher, and Y. Pomeau. Lattice-gas automata for the navier-stokes equation. *Phys. Rev. Lett.*, 56:1505–1508, Apr 1986.
117. F.J. Alexander, H. Chen, S. Chen, and G.D. Doolen. Lattice boltzmann model for compressible fluids. *Phys. Rev. A*, 46:1967–1970, Aug 1992.
118. R. Benzi, S. Succi, and M. Vergassola. The lattice boltzmann equation: theory and applications. *Phys. Rep.*, 222(3):145 – 197, 1992.
119. D.H. Rothman and S. Zaleski. *Lattice-Gas Cellular Automata (Simple Models of Complex Hydrodynamics)*, volume 10.1017/CBO9780511524714. 1997.
120. B. Chopard and M. Droz. *Cellular Automata Modeling of Physical Systems*, volume 10.1017/CBO9780511549755. 1998.

121. D.A Wolf-Gladrow. *Lattice Gas Cellular Automata and Lattice Boltzmann Models*, volume 10.1007/b72010. 2000.
122. N. Cao, S. Chen, S. Jin, and D. Martínez. Physical symmetry and lattice symmetry in the lattice boltzmann method. *Phys. Rev. E*, 55:R21–R24, Jan 1997.
123. R. Mei and W. Shyy. On the finite difference-based lattice boltzmann method in curvilinear coordinates. *J. Comput. Phys.*, 143(2):426 – 448, 1998.
124. T. Lee and Ching-Long Lin. A characteristic galerkin method for discrete boltzmann equation. *J. Comput. Phys.*, 171, 2001.
125. V. Sofonea and R.F. Sekerka. Viscosity of finite difference lattice boltzmann models. *J. Comput. Phys.*, 184, 2003.
126. V. Sofonea, A. Lamura, G. Gonnella, and A. Cristea. Finite-difference lattice boltzmann model with flux limiters for liquid-vapor systems. *Phys. Rev. E*, 70, 10 2004.
127. M. Watari and M. Tsutahara. Two-dimensional thermal model of the finite-difference lattice boltzmann method with high spatial isotropy. *Phys. Rev. E*, 67:036306, Mar 2003.
128. G. Gonnella, A. Lamura, and V. Sofonea. Lattice boltzmann simulation of thermal nonideal fluids. *Phys. Rev. E*, 76:036703, Sep 2007.
129. P.L. Bhatnagar, E. P. Gross, and M. Krook. A model for collision processes in gases. i. small amplitude processes in charged and neutral one-component systems. *Phys. Rev.*, 94:511–525, May 1954.
130. X. Shan, Xue-Feng Yuan, and H. Chen. Kinetic theory representation of hydrodynamics: a way beyond the navierstokes equation. *J. Fluid Mech.*, 550:413441, 2006.
131. Y. Guangwu, C. Yaosong, and H. Shouxin. Simple lattice boltzmann model for simulating flows with shock wave. 59:454–459, 12 1998.
132. Y. H. Qian and S. A. Orszag. Lattice bgk models for the navier-stokes equation: Nonlinear deviation in compressible regimes. *EPL (Europhysics Letters)*, 21(3):255, 1993.
133. B.T. Nadiga. An euler solver based on locally adaptive discrete velocities. *Journal of Statistical Physics*, 81(1):129–146, Oct 1995.
134. C. Sun. Lattice-boltzmann models for high speed flows. *Phys. Rev. E*, 58:7283–7287, Dec 1998.
135. T. Kataoka and M. Tsutahara. Lattice boltzmann model for the compressible navier-stokes equations with flexible specific-heat ratio. *Phys. Rev. E*, 69:035701, Mar 2004.
136. T. Kataoka and M. Tsutahara. Lattice boltzmann method for the compressible euler equations. *Phys. Rev. E*, 69:056702, May 2004.
137. Y. H. Qian, D. D'Humires, and P. Lallemand. Lattice bgk models for navier-stokes equation. *EPL*, 17(6):479, 1992.
138. R.R. Nourgaliev, T.N. Dinh, T.G. Theofanous, and D. Joseph. The lattice boltzmann equation method: theoretical interpretation, numerics and implications. *International Journal of Multiphase Flow*, 29(1):117 – 169, 2003.
139. Q. Li and A.J. Wagner. Symmetric free-energy-based multicomponent lattice boltzmann method. *Phys. Rev. E*, 76:036701, Sep 2007.
140. A.J.C. Ladd and R. Verberg. Lattice-boltzmann simulations of particle-fluid suspensions. *Journal of Statistical Physics*, 104(5):1191–1251, Sep 2001.
141. Z. Guo, C. Zheng, and B. Shi. Discrete lattice effects on the forcing term in the lattice boltzmann method. *Phys. Rev. E*, 65:046308, Apr 2002.
142. X. Shan and H. Chen. Simulation of nonideal gases and liquid-gas phase transitions by the lattice boltzmann equation. *Phys. Rev. E*, 49:2941–2948, Apr 1994.
143. J.M. Buick and C.A. Greated. Gravity in a lattice boltzmann model. *Phys. Rev. E*, 61:5307–5320, May 2000.
144. G. Gonnella, A. Lamura, A. Piscitelli, and A. Tiribocchi. Phase separation of binary fluids with dynamic temperature. *Phys. Rev. E*, 82:046302, Oct 2010.
145. A. Coclite, G. Gonnella, and A. Lamura. Pattern formation in liquid-vapor systems under periodic potential and shear. *Phys. Rev. E*, 89:063303, Jun 2014.
146. V. V. Sofonea, T. Biciusca, S. Busuioc, V.E. Ambrus, G. Gonnella, and A. Lamura. Corner-transport-upwind lattice boltzmann model for bubble cavitation. *Phys. Rev. E*, 97:023309, Feb 2018.
147. M.G. Ancona. Fully-lagrangian and lattice-boltzmann methods for solving systems of conservation equations. *Journal of Computational Physics*, 115(1):107 – 120, 1994.
148. E. Ilseven and M. Mendoza. Lattice boltzmann model for numerical relativity. *Phys. Rev. E*, 93:023303, Feb 2016.
149. Sauro Succi, Roberto Benzi, and Francisco Higuera. The lattice boltzmann equation: A new tool for computational fluid-dynamics. *Physica D: Nonlinear Phenomena*, 47(1):219 – 230, 1991.
150. O. Henrich, D. Marenduzzo, K. Stratford, and M.E. Cates. Domain growth in cholesteric blue phases: Hybrid lattice boltzmann simulations. *Computers and Mathematics with Applications*, 59(7):2360 – 2369, 2010. Mesoscopic Methods in Engineering and Science.
151. G. Negro, L.N. Carenza, P. Digregorio, G. Gonnella, and A. Lamura. Morphology and flow patterns in highly asymmetric active emulsions. *Physica A: Statistical Mechanics and its Applications*, 503:464 – 475, 2018.
152. Q. Zou and X. He. On pressure and velocity boundary conditions for the lattice boltzmann bgk model. *Physics of Fluids*, 9(6):1591–1598, 1997.
153. A. Lamura and G. Gonnella. Lattice boltzmann simulations of segregating binary fluid mixtures in shear flow. *Physica A: Statistical Mechanics and its Applications*, 294(3):295 – 312, 2001.
154. G. Kähler, F. Bonelli, G. Gonnella, and A. Lamura. Cavitation inception of a van der waals fluid at a sack-wall obstacle. *Physics of Fluids*, 27, 12 2015.
155. S. Sankararaman and S. Ramaswamy. Instabilities and waves in thin films of living fluids. *Phys. Rev. Lett.*, 102:118107, Mar 2009.
156. D. Marenduzzo, E. Orlandini, and J.M Yeomans. Hydrodynamics and rheology of active liquid crystals: A numerical investigation. *Phys. Rev. Lett.*, 98:118102, Mar 2007.
157. S. M. Fielding and P. D. Olmsted. Spatiotemporal oscillations and rheochaos in a simple model of shear banding. *Phys. Rev. Lett.*, 92:084502, Feb 2004.
158. D. Marenduzzo, E. Orlandini, M.E. Cates, and J.M. Yeomans. Lattice boltzmann simulations of spontaneous flow in active liquid crystals: The role of boundary conditions. *Journal of Non-Newtonian Fluid Mechanics*, 149(1):56 – 62, 2008. International Workshop on Mesoscale and Multiscale Description of Complex Fluids.

159. E. Orlandini, M. E. Cates, D. Marenduzzo, L. Tubiana, and J. M. Yeomans. Hydrodynamic of active liquid crystals: A hybrid lattice boltzmann approach. *Molecular Crystals and Liquid Crystals*, 494(1):293–308, 2008.
160. S. A. Edwards and J. M. Yeomans. Spontaneous flow states in active nematics: A unified picture. *EPL (Europhysics Letters)*, 85(1):18008, 2009.
161. L. Giomi, M.C. Marchetti, and T.B Liverpool. Complex spontaneous flows and concentration banding in active polar films. *Phys. Rev. Lett.*, 101:198101, Nov 2008.
162. Sumesh P. Thampi, Ramin Golestanian, and Julia M. Yeomans. Instabilities and topological defects in active nematics. *EPL (Europhysics Letters)*, 105(1):18001, 2014.
163. Sumesh P. Thampi, Ramin Golestanian, and Julia M. Yeomans. Vorticity, defects and correlations in active turbulence. *Philosophical Transactions of the Royal Society of London A: Mathematical, Physical and Engineering Sciences*, 372(2029), 2014.
164. J. Elgeti, M.E. Cates, and D. Marenduzzo. Defect hydrodynamics in 2d polar active fluids. *Soft Matter*, 7:3177–3185, 2011.
165. T. Lopez-Leon and Fernandez-Nieves. Drops and shells of liquid crystal. *A. Colloid Polym Sci*, 289:345, 2011.
166. J.F. Joanny and S. Ramaswamy. A drop of active matter. *J. Fluid Mech.*, 705:46, 2012.
167. PENGTAO YUE, JAMES J. FENG, CHUN LIU, and JIE SHEN. A diffuse-interface method for simulating two-phase flows of complex fluids. *Journal of Fluid Mechanics*, 515:293317, 2004.
168. G. De Magistris, A. Tiribocchi, C.A. Whitfield, R.J. Hawkins, M.E. Cates, and D. Marenduzzo. Spontaneous motility of passive emulsion droplets in polar active gels. *Soft Matter*, 10:7826–7837, 2014.
169. C.A. Whitfield and R.J. Hawkins. Instabilities, motion and deformation of active fluid droplets. *New Journal of Physics*, 18(12):123016, 2016.
170. Jérémie Gachelin, Gastón Miño, Hélène Berthet, Anke Lindner, Annie Rousselet, and Éric Clément. Non-newtonian viscosity of escherichia coli suspensions. *Phys. Rev. Lett.*, 110:268103, Jun 2013.
171. Héctor Matías López, Jérémie Gachelin, Carine Douarche, Harold Auradou, and Eric Clément. Turning bacteria suspensions into superfluids. *Phys. Rev. Lett.*, 115:028301, Jul 2015.
172. Salima Rafaï, Levan Jibuti, and Philippe Peyla. Effective viscosity of microswimmer suspensions. *Phys. Rev. Lett.*, 104:098102, Mar 2010.
173. Amarin G. McDonnell, Tilvawala C. Gopesh, Jennifer Lo, Moira O'Bryan, Leslie Y. Yeo, James R. Friend, and Ranganathan Prabhakar. Motility induced changes in viscosity of suspensions of swimming microbes in extensional flows. *Soft Matter*, 11:4658–4668, 2015.
174. Shuo Guo, Devranjan Samanta, Yi Peng, Xinliang Xu, and Xiang Cheng. Symmetric shear banding and swarming vortices in bacterial superfluids. *Proceedings of the National Academy of Sciences*, 2018.
175. Yashodhan Hatwalne, Sriram Ramaswamy, Madan Rao, and R. Aditi Simha. Rheology of active-particle suspensions. *Phys. Rev. Lett.*, 92:118101, Mar 2004.
176. T. B. Liverpool and M. C. Marchetti. Rheology of active filament solutions. *Phys. Rev. Lett.*, 97:268101, Dec 2006.
177. Luca Giomi, Tanniemola B. Liverpool, and M. Cristina Marchetti. Sheared active fluids: Thickening, thinning, and vanishing viscosity. *Phys. Rev. E*, 81:051908, May 2010.
178. M. E. Cates, S. M. Fielding, D. Marenduzzo, E. Orlandini, and J. M. Yeomans. Shearing active gels close to the isotropic-nematic transition. *Phys. Rev. Lett.*, 101:068102, Aug 2008.
179. J.O Kessler and M.F. Wojciechowski. *The collective behavior and dynamics of swimming bacteria*, chapter 15, page 417. New York: Oxford University Press, 1997.
180. N.H. Mendelson, A. Bourque, K. Wilkening, K.R. Anderson, and J.C. Watkins. Organized cell swimming motions in bacillus subtilis colonies: Patterns of short-lived whirls and jets. *J. Bacteriol.*, 181:600 – 609, 1999.
181. A. Sokolov, I.S. Aranson, J.O. Kessler, and R.E. Goldstein. Concentration dependence of the collective dynamics of swimming bacteria. *Phys. Rev. Lett.*, 98:158102, Apr 2007.
182. E. Lauga and R.E. Goldstein. Dance of the microswimmers. *Physics Today*, 65, 2012.
183. K. Drescher, R.E. Goldstein, N. Michel, M. Polin, and I. Tuval. Direct measurement of the flow field around swimming microorganisms. *Phys. Rev. Lett.*, 105:168101, Oct 2010.
184. C.W. Wolgemuth. Collective swimming and the dynamics of bacterial turbulence. *Biophys. J.*, 95(4):1564 – 1574, 2008.
185. J. Toner and Y. Tu. Flocks, herds, and schools: A quantitative theory of flocking. *Phys. Rev. E*, 58:4828–4858, Oct 1998.
186. G. Kokot, S. Das, R.G. Winkler, G. Gompper, I.S. Aranson, and A. Snezhko. Active turbulence in a gas of self-assembled spinners. *PNAS*, 114(49):12870–12875, 2017.
187. L. Giomi, L. Mahadevan, B. Chakraborty, and M.F. Hagan. Banding, excitability and chaos in active nematic suspensions. *Nonlinearity*, 25(8):2245, 2012.
188. L. Giomi. Geometry and topology of turbulence in active nematics. *Physical Review X*, 5, 7 2015.
189. L. Giomi, M.J. Bowick, P. Mishra, R. Sknepnek, and M.C. Marchetti. Defect dynamics in active nematics. *Philos. Trans. Royal Soc. A*, 372, 10 2014.
190. G. Boffetta R.E. and Ecke. Two-dimensional turbulence. *Annual Review of Fluid Mechanics*, 44(1):427–451, 2012.
191. V. Bratanov, F. Jenko, and E. Frey. New class of turbulence in active fluids. *Proc. Natl. Acad. Sci.*, 112(49):15048–15053, 2015.
192. Tyler N.; Thijssen Kristian; Yeomans Julia M. Doostmohammadi, Amin; Shendruk. Onset of meso-scale turbulence in active nematics. *Nature Communications*, 8, 5 2017.
193. Amin; Thijssen Kristian; Yeomans Julia M. Shendruk, Tyler N.; Doostmohammadi. Dancing disclinations in confined active nematics. *Soft Matter*, 2017.
194. Liang; Avila Kerstin; Jalikop Shreyas V.; Avila Marc; Hof Bjrn Lemoult, Grgoire; Shi. Directed percolation phase transition to sustained turbulence in couette flow. *Nature Physics*, 2 2016.
195. S. Ramachandran, P. B. Sunil Kumar, and I. Pagonabarraga. A lattice-boltzmann model for suspensions of self-propelling colloidal particles. *Eur. Phys. J. E*, 20:151–158, 2006.
196. A. J. C. Ladd. Numerical simulations of particulate suspensions via a discretized boltzmann equation. part 1. theoretical foundation. *Journ. Fluid. Mech.*, 271:285, 1994.

197. A. J. C. Ladd. Numerical simulations of particulate suspensions via a discretized boltzmann equation. part 2. numerical results. *Journ. Fluid. Mech.*, 271:311, 1994.
198. I. Llopis and I. Pagonabarraga. Dynamic regimes of hydrodynamically coupled self-propelling particles. *Europhys. Lett.*, 75:999, 2006.
199. F. Alarcón and I. Pagonabarraga. Spontaneous aggregation and global polar ordering in squirmer suspensions. *Journ. Mol. Liq.*, 185:56, 2013.
200. I. Llopis and I. Pagonabarraga. Hydrodynamic regimes of active rotators at fluid interfaces. *Eur. Phys. Journ. E*, 26:103, 2008.
201. H. Noji, R. Yasuda, M. Yoshida, and K. Jr. Kinosita. Direct observation of the rotation of f1-atpase. *Nature*, 386:299, 1997.
202. M. J. Lighthill. On the squirming motion of nearly spherical deformable bodies through liquids at very small reynolds numbers. *Communications on Pure and Applied Mathematics*, 46:109, 1952.
203. J. R. Blake. A spherical envelope approach to ciliary propulsion. *Journ. Fluid Mech.*, 46:199, 1971.
204. D. J. Earl, C. M. Pooley, J. F. Ryder, I. Bredberg, and J. M. Yeomans. Modeling microscopic swimmers at low reynolds number. *Journ. Chem. Phys.*, 126:064703, 2007.
205. A. Najafi and R. Golestanian. Simple swimmer at low reynolds number: Three linked spheres. *Phys. Rev. E*, 69:062901, 2004.
206. C. J. Smith and C. Denniston. Elastic response of a nematic liquid crystal to an immersed nanowire. *J. Appl. Phys.*, 101:014305, 2007.
207. J. de Graaf, H. Menke, A. J. T. M. Mathijssen, M. Fabritius, C. Holm, and T. N. Shendruk. Lattice-boltzmann hydrodynamics of anisotropic active matter. *J. Chem. Phys.*, 144:134106, 2016.
208. J. de Graaf, A. J. T. M. Mathijssen, M. Fabritius, H. Menke, C. Holm, and T. N. Shendruk. Understanding the onset of oscillatory swimming in microchannels. *Soft Matter*, 12:4704, 2016.
209. and B. Düenweg. Simulation of a single polymer chain in solution by combining lattice boltzmann and molecular dynamics. *Journ. Chem. Phys.*, 111:8225, 1999.
210. L. P. Fisher, T. Peter, C. Holm, and J. de Graaf. The raspberry model for hydrodynamic interactions revisited. i. periodic arrays of spheres and dumbbells. *J. Chem. Phys.*, 143:084107, 2015.
211. J. de Graaf, T. Peter, L. P. Fisher, and C. Holm. The raspberry model for hydrodynamic interactions revisited. ii. the effect of confinement. *J. Chem. Phys.*, 143:084108, 2015.
212. R. W. Nash, R Adhikari, and M. E. Cates. Singular forces and pointlike colloids in lattice boltzmann hydrodynamics. *Phys. Rev. E*, 77:026709, 2008.
213. J. P. Hernandez-Ortiz, C. G. Stolz, and M. D. Graham. Transport and collective dynamics in suspensions of confined swimming particles. *Phys. Rev. Lett*, 95:204501, 2005.
214. D. Saintillan and M. J. Shelley. Orientational order and instabilities in suspensions of self-locomoting rods. *Phys. Rev. Lett*, 99:058102, 2007.
215. J. de Graaf and J. Stenhammar. Lattice-boltzmann simulations of microswimmer-tracer interactions. *Phys. Rev. E*, 95:023302, 2017.
216. J. Stenhammar, C. Nardini, R. W. Nash, D. Marenduzzo, and A. Morozov. Role of correlations in the collective behavior of microswimmer suspensions. *Phys. Rev. Lett*, 119:028005, 2017.
217. G. W. Schmid-Schönbein, S. Usami, R. Skalak, and S. Chien. The interaction of leukocytes and erythrocytes in capillary and postcapillary vessels. *Microvasc. Res.*, 19:45, 1980.
218. S. Gekle. Strongly accelerated margination of active particles in blood flow. *Bioph. Journ.*, 110:514, 2016.
219. K. Vahidkhah, S. L. Diamond, and P. Bagchi. Platelet dynamics in three-dimensional simulation of whole blood. *Bioph. Journ.*, 104:2529, 2014.
220. K. VahidKhah and P. Bagchi. Microparticle shape effects on margination, near-wall dynamics and adhesion in a three-dimensional simulation of red blood cell suspension. *Soft Matter*, 11:2097, 2015.
221. N. Schopohl and T. J. Sluckin. Defect core structure in nematic liquid crystals. *Phys. Rev. Lett.*, 59:2582, 1987.
222. A.C. Callan-Jones, R.A. Pelcovits, V.A. Slavin, S. Zhang, D.H. Laidlaw, and G.B. Loriot. Simulation and visualization of topological defects in nematic liquid crystals. *Phys. Rev. E*, 74:061701, 12 2006.

A Biaxial nematics

In this Appendix we briefly discuss how to extend the uniaxial order parameter to biaxial nematics and how biaxiality provides information about the localization of topological defects in nematic liquid crystals.

A biaxial nematic is a nematic liquid crystal with three distinct optical axis and, unlike an uniaxial liquid crystal, it does not have any axis of complete rotational symmetry. Hence one can define three perpendicular axes $\mathbf{n}$, $\mathbf{m}$ and $\mathbf{l}$ (two are sufficient, as the third one would be perpendicular to the others), or director fields, for which there is a reflection symmetry. The order parameter in three dimensions is then

$$Q_{\alpha\beta} = S(n_\alpha n_\beta - \frac{1}{3}\delta_{\alpha\beta}) + \eta(m_\alpha m_\beta - \frac{1}{3}\delta_{\alpha\beta}), \qquad (110)$$

where S and η are called scalar order parameters. This representation of $\underline{\underline{\boldsymbol{Q}}}$ is a traceless symmetric second order rank tensor with five independent components. If the smaller of the two scalar order parameters is very small (like in many systems), one recovers the $\underline{\underline{\boldsymbol{Q}}}$ tensor in the uniaxial approximation.

For a biaxial nematic the three eigenvalues are in general different, and the diagonal representation of the $\underline{\underline{\boldsymbol{Q}}}$ tensor is

$$\boldsymbol{Q} = \mathrm{Diag}\left(\frac{2}{3}S\ ,\ -\frac{1}{3}S+\eta\ ,\ -\frac{1}{3}S-\eta\right) \qquad (111)$$

where $\eta \leqslant S$, with η gauging the degree of biaxiality.

The investigation of nematic defects in the context of a Landau-de Gennes theory has shown that their core presents a heavy degree of biaxiality [221]. By following the approach of Ref. [222], this can be measured by computing three scalars, $c_l = \tilde{\lambda}_1 - \tilde{\lambda}_2$, $c_p = 2(\tilde{\lambda}_2 - \tilde{\lambda}_3)$ and

$c_s = 3\tilde{\lambda}_3$, where $\tilde{\lambda}_1$, $\tilde{\lambda}_2$ and $\tilde{\lambda}_3$ (with $\tilde{\lambda}_1 \geq \tilde{\lambda}_2 \geq \tilde{\lambda}_3$) are three eigenvalues of the diagonalised matrix $D_{\alpha\beta} = Q_{\alpha\beta} + \delta_{\alpha\beta}/3$. These parameters fulfill the following properties: $0 \leq c_l, c_p, c_s \leq 1$ and $c_l + c_p + c_s = 1$. An ordered unixial nematic will give $c_l \simeq 1$, while the isotropic state, where both S and η are approximatively null, corresponds to $c_s \simeq 1$. Finally the biaxial case implies $c_p \simeq 1$.

B Recovering continuum equations for the algorithm described in Section 3.3.2

In this Appendix we show the calculations to recover the continuum equations obtained by means of the forcing method algorithm discussed in Section 3.3.2.

We start with a Chapman-Enskog expansion of the distribution functions and of the derivatives according to relations (34)-(36), and for the forcing term we assume that

$$\mathcal{F}_i = \epsilon \mathcal{F}_{i1}. \tag{112}$$

. By Taylor expanding the evolution equation (20), we get

$$\Delta t(\partial_t + \xi_{i\alpha}\partial_\alpha) f_i + \frac{\Delta t^2}{2}(\partial_t^2 + 2\xi_{i\alpha}\partial_\alpha\partial_t + \xi_{i\alpha}\xi_{i\beta}\partial_\alpha\partial_\beta) f_i = \Delta t \mathcal{F}_i - \frac{f_i - f_i^{eq}}{\tau}. \tag{113}$$

We now substitute Eq. (34)-(36) and (112) in Eq. (113) and, after grouping terms of the same order in ϵ, we get

$$f_i^{(0)} = f_i^{eq} + \mathcal{O}(\epsilon), \tag{114}$$

$$(\partial_{t_1} + \xi_{i\alpha}\partial_{\alpha_1}) f_i^{(0)} = -\frac{1}{\tau\Delta t} f_i^{(1)} + F_{i1} + \mathcal{O}(\epsilon), \tag{115}$$

$$\partial_{t_1} f_i^{(1)} + \xi_{i\alpha}\partial_{\alpha_1} f_i^{(1)} + \partial_{t_2} f_i^{(0)} + \frac{\Delta t}{2}\left(\partial_{t_1}^2 + 2\xi_{i\alpha}\partial_{\alpha_1}\partial_{t_1} + \xi_{i\alpha}\xi_{i\beta}\partial_{\alpha_1}\partial_{\beta_1}\right) f_i^{(0)} = -\frac{1}{\tau\Delta t} f_i^{(2)} + \mathcal{O}(\epsilon). \tag{116}$$

From these equations one gets the zeroth-order moments of the distrubution functions

$$\sum_i f_i^{(0)} = \sum_i f_i^{eq} = \rho \qquad \sum_i f_i^{(1)} = \sum_i f_i^{(2)} = 0, \tag{117}$$

the first-order ones

$$\sum_i f_i^{(0)} \xi_{i_\alpha} = \sum_i f_i^{eq} \xi_{i_\alpha} = \rho v_\alpha, \tag{118}$$

$$\sum_i f_i^{(1)} \xi_{i_\alpha} = -\frac{\Delta t}{2} F_{1\alpha}, \tag{119}$$

$$\sum_i f_i^{(2)} \xi_{i_\alpha} = 0. \tag{120}$$

and the zeroth, first and second moments of the forcing term

$$\sum_i \mathcal{F}_i = 0, \tag{121}$$

$$\sum_i \mathcal{F}_i \xi_{i\alpha} = \left(1 - \frac{\Delta t}{2\tau}\right) F_\alpha, \tag{122}$$

$$\sum_i \mathcal{F}_i \xi_{i\alpha}\xi_{i\beta} = \left(1 - \frac{\Delta t}{2\tau}\right)(v_\alpha F_\beta + v_\beta F_\alpha). \tag{123}$$

These relations can be explicitly calculated by using Eq. (75). Now combining the zeroth-order moment of Eq. (115) with Eqs. (117) and (121), one gets

$$\partial_{t_1}\rho + \partial_{\beta_1}(\rho v_\beta) = 0, \tag{124}$$

the continuity equation at first order in the Knudsen number. To recover it at second order we apply the differential operators ∂_{t_1} and $\xi_{i\alpha}\partial_{\alpha_1}$ to Eq. (115) and then, by perfoming the difference between the two resulting equations, one has

$$\partial_{t_1}^2 f_i^{(0)} = \xi_{i\alpha}\xi_{i\beta}\partial_{\alpha_1}\partial_{\beta_1} f_i^{eq} - \frac{1}{\tau\Delta t}(\partial_{t_1} - \xi_{i\gamma}\partial_{\gamma_1}) f_i^{(1)} + (\partial_{t_1} - \xi_{i\gamma}\partial_{\gamma_1})\mathcal{F}_{i1}. \tag{125}$$

Now we substitute the latter into Eq. (116) and, by using Eq. (115), we obtain

$$(\partial_{t_1} + \xi_{i\alpha}\partial_{\alpha_1}) f_i^{(1)} + \partial_{t_2} f_i^{(0)} - \frac{1}{2\tau}\left[\partial_{t_1} + \xi_{i\gamma}\partial_{\gamma_1}\right] f_i^{(1)} = -\frac{1}{\tau\Delta t} f_i^{(2)} - \frac{\Delta t}{2}(\partial_{t_1} + \xi_{i\gamma}\partial_{\gamma_1})\mathcal{F}_{i1}. \tag{126}$$

Finally summing this one over index i and by means of Eqs. (114)-(122), we get

$$\partial_{t_2}\rho = 0, \tag{127}$$

which represents the continuity equation at second order in the Knudsen number.

To reproduce the Navier-Stokes equation, we start by computing the first moment of Eq. (115) that, after using Eqs. (117)-(123), reads

$$\partial_{t_1}(\rho v_\alpha) + \partial_{\beta_1}\left(\frac{c^2}{3}\rho\delta_{\alpha\beta} + \rho v_\alpha v_\beta\right) = F_\alpha. \tag{128}$$

Following the same procedure for Eq. (126) we get

$$\partial_{t_2}(\rho v_\alpha) = \frac{c^2}{3}\Delta t\left(\tau - \frac{1}{2}\right)\partial_{\beta_1}\left[\rho(\partial_{\beta_1} v_\alpha + \partial_{\alpha_1} v_\beta)\right]. \tag{129}$$

Finally, summing these two equations, one can restore the Navier-Stokes equation

$$\partial_t(\rho v_\alpha) + \partial_\beta\left(\rho v_\alpha v_\beta\right) = \partial_\beta\sigma_{\alpha\beta} + \frac{c^2}{3}\Delta t\left(\tau - \frac{1}{2}\right)\partial_{\beta_1}\left[\rho(\partial_{\beta_1} v_\alpha + \partial_{\alpha_1} v_\beta)\right], \tag{130}$$

where we require that

$$F_\alpha = \partial_\beta \left[\sigma_{\alpha\beta} + \frac{c^2}{3} \rho \delta_{\alpha\beta} \right], \tag{131}$$

and the kinematic viscosity is

$$\nu = \frac{c^2}{3} \Delta t \left(\tau - \frac{1}{2} \right). \tag{132}$$